Gravitational Interactions and Resonances in Ring-Moon Systems

A Dissertation
Presented in Partial Fulfilment of the Requirements for the
Degree of Doctor of Philosophy
with a
Major in Physics
in the
College of Graduate Studies
University of Idaho
by
Joseph A. A'Hearn

Approved by
Major Professor: Matthew M. Hedman, Ph.D.
Committee Members: Jason W. Barnes, Ph.D.; Douglas P. Hamilton, Ph.D.;
Eric Mittelstadt, Ph.D.
Department Chair: John Hiller, Ph.D.

May 2022

Abstract

While resonances determine the large-scale dynamical structure of planetary systems, interactions among the small bodies in these resonances impact their orbital evolution. We use numerical simulations to study the orbital evolution of interacting small bodies orbiting within two different locations in Saturn's rings, and of interacting equal-mass co-orbitals. Modeling the clumps in Saturn's D68 ringlet as co-orbital point-masses reveals the fragility of low-mass co-orbital satellite systems. Simulations of multiple massive bodies in a common corotation resonance site, such as the ring arc of Saturn's moon Aegaeon, reveal the importance of interaction timescales for multi-body orbital dynamics. We also investigate the planetary normal mode spectra of Uranus and Neptune to predict where in their rings we might expect to see resonant phenomena.

Acknowledgements

I thank my advisor Matt Hedman first of all. He has consistently been available to talk and has given me the time I needed, both with his door open when things were more in-person and also by email and video chat. He leads by example, often arriving early to work on research, and has earned multiple awards for his scientific contributions. Yet he does not put unnecessary pressure on me. He even reminded me early on that I was not expected to work on weekends and that I should not work more than 8 hours in a day. I have described him to others as the ideal Ph.D. advisor, and I am grateful that I have had the opportunity to work for him.

Next I thank the other members of my committee: Jason Barnes, Doug Hamilton, and Eric Mittelstaedt. Jason has played a large role in all things related to Planetary Science at the University of Idaho, and has also been a great friend. He provided valuable academic feedback and career advice, let me drive his second Tesla, and switched off playing shortstop with me on our softball team. I met Doug when he came to Idaho for the total solar eclipse in 2017. Doug has helped my research with his insights and was a co-author on my second paper, even during a wild sabbatical year. Eric taught me Geodynamics in my first semester of graduate school and has always been approachable. He is excited to talk about research and has shared valuable career and parenting advice.

I thank my co-authors (besides Matt and Doug, whom I have already mentioned): Maryame El Moutamid, Mark Marley, Chris Mankovich, Marco Munoz-Gutiérrez, Paola Contreras, Silvia Giuliatti Winter, Gustavo Madeira, Hima Aramona. Maryame helped me in my first project when I was struggling to make my code work that was supposed to convert between state vectors and geometric orbital elements. She shared her `Fortran` code with me, with comments in French, but looking at it was enough to help me figure out what to do to make my code work. Chris Mankovich has been extremely helpful during my third project, guiding me in ring seismology and how to run `GYRE`. I have not interacted with Hima, but working under Chris during a summer, he produced three interior models of Uranus that were important in advancing my third project. I met Marco at the DPS meeting in Knoxville, and he followed up with an email that led to a collaboration on an additional project that is now published. Paola and Gustavo have shown quality work and dedication in this collaboration. Mark Marley and Silvia Giuliatti Winter have been the experienced researchers ensuring quality in projects led by us younger folks.

I thank my Planetary Science companions in the Physics Department, first of all those who blazed the trail before me: Johnathon Ahlers, Shannon MacKenzie, Rob Chancia, and Rajani Dhingra; and next, those who have been following it after me: Steven Kreyche, Himanshi Sharma, Doug Creel, William Miller, Bill Bridges, Michael Heslar, Daniel Coulter, AnnaSage Ross-Browning, Katie Denny, Elizabath Atang, Alex Etgen, and Victor Afigbo. Of these I especially thank Johnathon Ahlers and Rob Chancia for being there for me to turn to them with any questions relating to math, science, coding, scientific proposals, and career advice.

I thank my Physics Department cohort, particularly Jonathan Barnes, Marshall Boyland, and Dillon Morehouse, who all spent hours with me in EP 309 figuring out our Physics homework. I also thank those who followed in the year after me, especially Sanjoy Saha and Ross Miller.

I thank my academic friends from the Geology Department (besides Eric, whom I have already mentioned): faculty members Leslie Baker, Erika Rader, and Tim Bartholomaus, for their guidance during Planetary Science journal club as well as Geology Department courses that I took; and graduate students with whom I interacted in those courses and in journal club: Haley Thoreson, Margot Vore, Emily Forsberg, and Emma Swaninger.

I thank my friend Dylan Hull-Nye for helping me whenever I had statistics questions.

I thank people in the larger communities of Planetary Science and Dynamical Astronomy: Phil Nicholson, Matija Ćuk, David Atkinson, Ryan Park, Matt Tiscareno, Mark Showalter, Dick French, Mark Hofstadter, Rebecca Dawson, Jim Fuller, Jonathan Fortney, Krista Soderlund, Isamu Matsuyama, Ravit Helled, Nadine Nettelmann, Kat Volk, Marina Brozović, Leigh Fletcher, Billy Quarles, Dan Tamayo, Juliette Becker, David Hernandez, Smadar Naoz, Jack Lissauer, Ludwig Scheibe, Faith Vilas, and many others.

Dedication

I would like to dedicate this dissertation to those who have helped me personally. First of all I thank God, who created the universe in an overflowing of love, and has allowed it to evolve to where it is today. I thank my wife Lilia, who has been patient with me while I have pursued the light at the end of this tunnel, and my sons, Owen and Titus.

I thank my family of origin for all their support: my mom, up until she passed away due to cancer right at the end of my second year of graduate school, and my dad and brother, who have always been close to me.

I thank my in-laws especially for helping watch Owen. I thank my extended family and friends for moral support. Finally, I thank others who have inspired me, especially St. Thomas Aquinas and Galileo Galilei.

Table of Contents

List of Tables

List of Figures

Statement of Contribution

Chapters 2, 3, and 4 are multi-authored articles in which I was the first author. Section 5.2.2 consists of excerpts that I am the primary author of from a multi-authored article for the rest of which the contributions were primarily from the other co-authors. Those other parts of that paper are not included in this dissertation. I ran the `Mercury6` code for Chapters 2 and 3, and the `GYRE` code for Chapter 4. I performed the analysis of the simulation results using my own `Python` code. I produced all the figures that are included in this dissertation.

For Chapters 2, 3, and 4, the second author is Matt Hedman, who guided me during these projects, meeting with me at least once a week, and provided suggestions throughout the writing process.

For Chapter 2, the third author is Maryame El Moutamid, who discussed my project with me when she visited Idaho in 2016 and shared with me her `Mercury6` setup files and `Fortran` code (commented in French). The latter was especially useful to me as a reference as I was writing my own `Python` code to convert between state vectors and geometric orbital elements. She also provided suggestions for textual changes before I submitted the paper.

For Chapter 3, the third author is Doug Hamilton, who discussed co-orbital systems with me when he visited Idaho in 2017 for the total Solar eclipse. He continued to provide insights and feedback on my project, including suggestions for textual changes before submission.

For Chapter 4, the third, fourth, and fifth authors are Chris Mankovich, Hima Aramona, and Mark Marley. Mark Marley forwarded me interior models of Uranus and Neptune that were sent to him from Nadine Nettelmann and Ravit Helled. I wrote a code to convert these interior models into the `MESA` format to input them into `GYRE`. Of these models, the only one that successfully ran in `GYRE`, and thus appeared in the paper, was Scheibe et al. (2019)'s adiabatic Uranus model. Chris Mankovich produced interior models of Saturn, Uranus, and Neptune, and oversaw Hima Aramona, who produced the triplet of Uranus models, all of which I used as input, already in the `MESA` format, when I ran the stellar oscillation code `GYRE`. Chris guided me and answered questions relating to using `GYRE` and to planetary seismology in general. While I was the primary author of most of the text, three paragraphs in Section 4.4 concerning how the interior models were produced were written by Chris Mankovich. Chris and Mark provided suggestions for textual changes before submission. Mark also helped throughout the project with high-level suggestions.

The paper from which Section 5.2.2 is excerpted lists Marco Muñoz-Gutiérrez as the first author, A. Paula Granados Contreras as the second author, Gustavo Madeira as the third author, myself as the fourth author, and Silvia Giuliatti Winter as the fifth author. Marco is the one who set up the collaboration for the paper after a discussion I had with him at the 2018 DPS meeting in Knoxville. For the paper, Marco and Paula performed simulations in `Mercury6` concerning the search for a resonance for Pallene, and were the primary authors of the corresponding part of the paper. Gustavo and Silvia performed the simulations in `Mercury6` concerning the Pallene ring, and were the primary authors of the corresponding part of the paper. I did the calculations and composed the text relating to tidal evolution. Marco and Paula provided suggestions for textual changes to what I had composed. I only provide the excerpts of which I was the primary author.

Other parts of Chapter 5 include text that has been taken and adapted from reports or proposals I have written. Before I submitted these, individuals who provided suggestions for textual changes were Matt Hedman, Jason Barnes, Jonathan Fortney, Jim Fuller, Krista Soderlund, Isamu Matsuyama, and Ryan Park.

CHAPTER 1

Introduction

1.1 The outer Solar system

The outer Solar system is a sandbox for the exploration of gravitational interactions and resonances in ring-moon systems. In this Section, I comment briefly on many of the resonant phenomena in the outer Solar system. In Section 1.2, I review the basics of orbits. In Section 1.3, I discuss the fundamentals of orbital evolution and resonances. Feel free, if necessary, to read Sections 1.2 and 1.3 first and then return to this Section.

The three inner Galilean moons of Jupiter are in a three-body resonance such that Io orbits twice for every time Europa orbits, and Europa orbits twice for every time Ganymede orbits. This is called the Laplace resonance and can also be expressed in terms of mean longitudes λ of the moons:

$$\varphi = \lambda_I - 3\lambda_E + 2\lambda_G \simeq 180^\circ. \tag{1.1}$$

The resonant argument φ oscillates around 180° with an amplitde of 0.03° (Sinclair, 1975). This relation makes a conjunction among all three moons impossible. Instead, whenever one moon passes another, the third is at least 60° away from the conjunction of the other two moons (Murray and Dermott, 1999). This fact helps the system remain stable, preserving this resonance.

The Saturnian system, with its magnificent rings and significant number of mid-sized moons, has the largest number of known resonances out of any orbital system. Titan, Saturn's only large moon, and Hyperion are in a 4:3 resonance, Enceladus and Dione are in a 2:1 resonance, and Mimas and Tethys are in a 4:2 inclination resonance (Murray and Dermott, 1999). Mimas's 2:1 resonance produces a gap between Saturn's A and B rings, called the Cassini Division (Goldreich and Tremaine, 1978). The small moons Anthe, Methone, and Aegaeon are each confined along with an arc of ring material by corotation eccentricity resonances with Mimas (Spitale et al., 2006; Hedman et al., 2007b; Hedman et al., 2009b, 2010; Cooper et al., 2008). These, especially that of Aegaeon, are covered in more detail in Chapter 2. The small moons Pan, Pandora, Prometheus, and Janus are responsible for a number of resonant phenomena in the A ring. Janus and Epimetheus, of comparable masses, are in a sort of 1:1 resonance that I discuss further in Chapter 5, and their orbital swap every four years affects the outer edge of the A ring through a 7:6 Lindblad resonance (El Moutamid et al., 2016). Other moons in 1:1 resonances include the Trojan moons, which librate around a stable Lagrange point of another moon: Telesto and Calypso are Trojans of Tethys, while Helene and Polydeuces are Trojans of Dione. The C ring has several density waves and bending waves that have been tied to resonances with normal modes of the planet Saturn itself, which have given rise to the field of kronoseismology (Hedman and Nicholson, 2013; Hedman et al., 2014; French et al., 2016, 2019; Hedman et al., 2019; French et al., 2021; Hedman et al., 2022), confirming predictions made by Marley and Porco (1993).

Resonances influence several of the narrow Uranian rings. For example, the ϵ ring is shepherded by Cordelia and Ophelia: its inner edge coincides with the 24:25 outer eccentric resonance with Cordelia, while the outer edge coincides with the 14:13 inner eccentric resonance with Ophelia (Goldreich and Porco, 1987; French et al., 1991; French and Nicholson, 1995; Nicholson et al., 2018). The 6:5 resonance with Ophelia falls within the γ ring and affects its brightness (Showalter, 2011; Hedman and Chancia, 2021). Cressida affects the η ring's kinematics through a 3:2 inner Lindblad resonance (Chancia et al., 2017). The 23:22 resonance with Cordelia lies near the δ ring, but does not seem to strongly influence the ring (Hedman and Chancia, 2021). Similarly, the small moons Rosalind and Cordelia are close to a 5:3 resonance (Murray and Thompson, 1990). Although the innermost rings, from the 6 ring to the β ring, do not line up well with satellite resonances, a number of planetary normal mode resonances fall in this region. This topic is explored specifically in Chapter 4.

Neptune's ring arcs in the Adams ring, discovered through ground-based occultation events (Hubbard et al., 1985, 1986; Manfroid et al., 1986), and then imaged by Voyager (Smith et al., 1989), are confined longitudinally, likely by a resonance. Although several ideas have been proposed about the particular resonance of Neptune's ring arcs, consensus has not been reached. Initial studies suspected that a 42:43 resonance with Galatea confined the ring arcs (Goldreich et al., 1986; Porco, 1991; Namouni and Porco, 2002). Deviations from the exact rate of different types of a corotation resonance with Galatea, however, support other possible explanations (Renner et al., 2014). Confinement due to shepherding by undetected satellites that are co-orbital with the Adams ring arcs has been proposed (Lissauer, 1985; Salo and Hanninen, 1998; Renner et al., 2014), though more recent investigation claims to rule out that co-orbital satellites could be the source of the dust (Giuliatti Winter et al., 2020). Another recent idea is that the Adams ring arcs are in a three-body resonance with Galatea and Larissa (Showalter et al., 2017). Nevertheless, none of these theories explain how two of the ring arcs could have faded since 1989, while the other two have survived (de Pater et al., 2018; Souami et al., 2021). The contents of Chapter 2 are likely relevant to Neptune's ring arcs, though the exploration required to confirm this is mentioned in Chapter 5 as possible future work. The possible perturbation of the Adams ring by a Neptunian g-mode resonance is discussed in Chapter 4.

Rings have also been discovered around smaller bodies: the centaurs Chariklo (Braga-Ribas et al., 2014) and possibly Chiron (Ortiz et al., 2015) as well as the dwarf planet Haumea (Ortiz et al., 2017). These new ring systems have presented an opportunity for new developments in ring theory (Sicardy et al., 2019; Sicardy, 2020; Madeira et al., 2022). Sicardy et al. (2021) highlighted the importance of the 1:3 spin-orbit resonance for small bodies.

The main chapters (2, 3, and 4) of this dissertation are structured only by order of publication. They treat a variety of topics related to gravitational interactions and resonances in ring-moon systems. In Chapter 2, we investigate the dynamics of multiple masses in the same corotation resonance site, including important consequences from energy conservation. This has a specific application for the three ring arcs in the Saturnian system, especially that of Aegaeon. In Chapter 3, we look at co-orbital systems with a specific application to the clumps in Saturn's D68 ringlet. The chapter will show how fragile and perhaps transient the collection of D68 clumps may be. In Chapter 4, we examine the prospect of applying ring seismology to the ice giants Uranus and Neptune. Finally, in Chapter 5, I summarize the work presented in this thesis, explain its significance, and remark on preliminary and future projects related to this work.

The remaining sections of this introduction provide further theoretical background for the studies that follow.

1.2 Orbit fundamentals

Kepler's Third Law (1619) describes the relation between an orbiting object's orbital period T and its semi-major axis a in a two-body system:

$$a^3 = \frac{G\left(M+m\right)}{4\pi^2}T^2, \tag{1.2}$$

where G is the gravitational constant, M is the mass of the central body, and m is the mass of the orbiting body. By defining $\mu = G\left(M+m\right)$ and the mean motion $n = 2\pi/T$, we can write Kepler's Third Law as

$$\mu = n^2 a^3. \tag{1.3}$$

Kepler's Third Law, however it is written, is a good starting point for the scientific investigations of orbits. Although it remains unknown how Kepler arrived at his Third Law before Newton (Kozhamthadam, 1994), it can be derived directly from Newton's Second Law of Motion:

$$F = ma \tag{1.4}$$

and Newton's Universal Law of Gravitation (Newton, 1687):

$$F = G\frac{Mm}{r^2} \tag{1.5}$$

The gravitational field of a point-mass is described by

$$V\left(r\right) = \frac{GM}{r} \tag{1.6}$$

where V (sometimes written as U or φ) is the gravitational potential.

Kepler's First Law states that orbits are elliptical. The ellipticity of an orbit is measured by a quantity between 0 (a circle) and 1 (a parabola) called its eccentricity e. Orbits are not always in-line with the equatorial plane of the central body. The angle between the central body's equatorial plane and the orbital plane is called the inclination i. A few more angular quantities are needed for us to be able to specify an orbit's configuration and where the orbiting body is. For an inclined orbit, the location where the orbiting body goes from below the equatorial plane to above the equatorial plane is called the ascending node. The angle between a reference direction and the ascending node is called the longitude of ascending node Ω. For an orbit with no inclination, the longitude of the ascending node would be undefined, but in these cases, for computational purposes, it is normally set to zero. Because what we call the central body is not found at the ellipse's center but rather at one of its foci, there is a special place in the orbit called the pericenter, where the particle is closest to the central body. The orientation of the orbit with respect to some reference frame can be described with an angular quantity. For this angle, some use the argument of pericenter ω, which measures the angle from the ascending node to pericenter; while others use the longitude of pericenter ϖ, which is a dog-legged angle spanning from the reference direction to the ascending node, and then from the ascending node to pericenter. Thus we have $\varpi = \Omega + \omega$. I will use the longitude of pericenter ϖ in this dissertation. With the previous five orbital elements, the shape of the orbit is fully defined, but we still need to know where the orbiting body is in its orbit. A few slightly different parameters do this: the true anomaly f defined as the angle at the central body between pericenter and the orbiting body's location, the true longitude $\theta = f + \varpi$, mean anomaly $M = n\,(t - \tau)$, where the constant τ is the time of pericenter passage, and mean longitude $\lambda = M + \varpi$. I will use the mean longitude λ in this dissertation. For more details about orbital elements, see Chapter 2 of Murray and Dermott (1999).

1.3 Orbital evolution and resonances

Real-world systems, however, are not as simple as the theoretical two-body system. The introduction of a third mass into the system gives rise to the still not completely solved three-body problem. Chapter 3 of Murray and Dermott (1999) discusses the "restricted three-body problem", in which two of the bodies move in coplanar orbits about their common center of mass, and the third body's mass is small enough to be neglected. In such a system, there are five special locations, called Lagrange points, where the negligible mass could orbit the primary with the same period as the secondary. The first three Lagrange points are collinear with the other two bodies. L_1 is in between the two larger masses, while L_2 is exterior to the secondary. Both L_1 and L_2 share the same mean longitude λ as the secondary. L_3 is found on the other side of the orbit from the secondary (180° away). The fourth and fifth Lagrange points involve the Coriolis force and are stationed at points that form equilateral triangles with the primary and secondary: L_4 is 60° ahead of the secondary, while L_5 is 60° behind it. With respect to equilibrium, the first three Lagrange points are saddle points, i.e. stable for small oscillations in one direction, but not the other; while the fourth and fifth Lagrange points are stable for small oscillations in any direction. Oscillatory motion near one of these stable Lagrange points is referred to as "tadpole" motion. Another type of motion, referred to as "horseshoe" motion, describes particles that pass alternate between L_4 and L_5 via L_3. See Section 5.3 for further discussion of tadpole and horseshoe motion. As long as a particle is not found exactly at one of the Lagrange points, its orbit will evolve over time, and not always in closed loops.

Orbital evolution also occurs when the system contains additional masses. This happens especially when the periods or frequencies of the orbits of these masses are related through an integer multiple. This is called an orbital resonance. Many examples of orbital resonances were mentioned above in Section 1.1. Some orbital resonances foster stability under small oscillations, such as the 3:2 resonance between Neptune and Pluto, which guarantees that whenever Pluto crosses Neptune's orbit, Neptune is not nearby. Other orbital resonances drive instability, such as the Kirkwood Gaps, specific semi-major axes in the asteroid belt where fewer asteroids orbit due to perturbations from Jupiter.

Orbital evolution will also occur if the central body is oblate. The gravitational field influenced by oblateness of the central body becomes

$$V = -\frac{GM_1}{r}\left[1 - \sum_{i=1}^{\infty} J_{2i}\left(\frac{R}{r}\right)^{2i} P_{2i}\left(\sin\alpha\right)\right], \tag{1.7}$$

where J_{2i} are even gravitational harmonics, $P_{2i}(\sin\alpha)$ are Legendre polynomials of degree i in $\sin\alpha$, α is the latitude of the particle. As a consequence of the J_{2i} terms in this equation, the mean motion n is no longer the only frequency that governs the motion; in addition, a radial frequency κ and a vertical frequency ν become relevant. These quantities, according to first-order theory in e and i, are given by partial first- and second-derivatives of the gravitational potential (Murray and Dermott, 1999):

$$n^2 = \frac{1}{a}\left(\frac{\partial V}{\partial r}\right)_0 \tag{1.8}$$

$$\kappa^2 = \frac{3}{a}\left(\frac{\partial V}{\partial r}\right)_0 + \left(\frac{\partial^2 V}{\partial r^2}\right)_0 \tag{1.9}$$

$$\nu^2 = \frac{1}{a}\left(\frac{\partial V}{\partial r}\right)_0 + \frac{1}{a^2}\left(\frac{\partial^2 V}{\partial \alpha^2}\right)_0 . \tag{1.10}$$

This distinction results in precession of the pericenter and of the ascending node according to the following relations (Murray and Dermott, 1999):

$$\frac{d\varpi}{dt} = n - \kappa \tag{1.11}$$

$$\frac{d\Omega}{dt} = n - \nu \tag{1.12}$$

Orbital evolution as an effect of oblateness is relevant in all the chapters throughout this dissertation, but especially in Chapter 2.

A resonance can also occur between an orbiting body and the rotating central body. Resonances of this type that we will discuss at length in Chapter 4 are with planetary normal modes, internal oscillations of the planet itself. Following Marley and Porco (1993), we can write the total gravitational potential as a sum of an unperturbed component and a perturbed component:

$$V = V_0 + V'(t), \tag{1.13}$$

where the unperturbed component is

$$\begin{aligned} V_0 = & \frac{GM}{r} \left[1 - \sum_{\ell=1}^{\infty} \left(\frac{R}{r} \right)^{\ell} J_{\ell} P_{\ell} (\cos\theta) \right. \\ & + \sum_{\ell=1}^{\infty} \sum_{m=1}^{\infty} \left(\frac{R}{r} \right)^{\ell} P_{\ell}^{m} (\cos\theta) \\ & \left. \times \left(C_{\ell m} \cos m\phi + S_{\ell m} \sin m\phi \right) \right] \end{aligned} \tag{1.14}$$

and the perturbed component is

$$\begin{aligned} V' = & \frac{GM}{r} \sum_{n=0}^{\infty} \left[- \sum_{\ell=2}^{\infty} \left(\frac{R}{r} \right)^{\ell} J'_{\ell} P_{\ell} (\cos\theta) \right. \\ & + \sum_{\ell=2}^{\infty} \sum_{m=-\ell}^{\ell} \left(\frac{R}{r} \right)^{\ell} P_{\ell}^{m} (\cos\theta) \\ & \left. \times \left(C'_{\ell m} \cos m\phi + S'_{\ell m} \sin m\phi \right) \right]. \end{aligned} \tag{1.15}$$

The harmonics are normalized to the equatorial radius R. The non-axisymmetric terms $C_{\ell m}$ and $S_{\ell m}$ are zero for a fluid planet in hydrostatic equilibrium. The perturbed gravitational harmonics, taking the integrals over the density perturbation, can then be reduced to

$$MR^{\ell} J'_{\ell n} = - \left(\frac{4\pi}{2\ell + 1} \right)^{1/2} e^{i\sigma_{\ell 0 n} t} \int_0^R \rho'_{\ell n} (r) \, r^{\ell+2} dr \tag{1.16}$$

for $m = 0$, and

$$\begin{aligned} MR^{\ell} C'_{\ell m n} = & (-1)^{\frac{m+|m|}{2}} \left[\frac{2\ell + 1}{4\pi} \left(\frac{(\ell - |m|)!}{(\ell + |m|)!} \right) \right]^{1/2} \\ & \times e^{i\sigma_{\ell m n} t} \int_0^R \rho'_{\ell m n} (r) \, r^{\ell+2} dr \end{aligned} \tag{1.17}$$

for $m \neq 0$. Evaluation of these quantities can reveal the depths in the planet that give rise to specific planetary normal modes, as is illustrated in Chapter 4.

CHAPTER 2

Dynamics of multiple bodies in a corotation resonance: Conserved quantities and relevance to ring arcs

Joseph A. A'Hearn, Matthew M. Hedman, Maryame El Moutamid, "Dynamics of multiple bodies in a corotation resonance: Conserved quantities and relevance to ring arcs", *The Astrophysical Journal* 882, 66, 2019

In this work I began my investigation of ring arcs and resonances. The project reported here started as an exploration of what we called "the Aegaeon Four-Body Problem," and was one of several research avenues within the funding scope of the Cassini Data Analysis and Participating Scientist Program grant to study the structure, composition, and history of Saturn's faint rings. Because I had previous experience from my final undergrad semester with running `Mercury6` *code to investigate orbital evolution, this was an appealing project to take on. The problem with Aegaeon was that, compared to Anthe and Methone, which are the other moons in rings arcs confined by corotation eccentricity resonances with Mimas, Aegaeon is both less dominant in its ring arc in terms of mass and also much closer to the center of the corotation site. Our intuition told us that these two scientific facts must be connected in some non-trivial way, which I set out to explore. It turned out that our intuition was incorrect. What I discovered about how energy is conserved in corotation resonances makes it even more difficult to explain those two simultaneous facts about Aegaeon.*

2.1 Abstract

The interactions among objects in a mean motion resonance are important for the orbital evolution of satellites and rings, especially Saturn's ring arcs and associated moons. In this work, we examine interactions among massive bodies in the same corotation eccentricity resonance site that affect the orbital evolution of those bodies using numerical simulations. During these simulations, the bodies exchange angular momentum and energy during close

encounters, altering their orbits. This energy exchange, however, does not mean that one body necessarily moves closer to exact corotation when the other moves away from it. Indeed, if one object moves towards one of these sites, the other object is equally likely to move towards or away from it. This happens because the timescale of these close encounters is short compared to the synodic period between these particles and the secondary mass (i.e., the timescale where corotation sites can be treated as potential maxima). Because the timescale of a gravitational encounter is comparable to the timescale of a collision, we could expect energy to be exchanged in a similar way for collisional interactions. In that case, these findings could be relevant for denser systems like the arcs in Neptune's Adams ring and how they can be maintained in the face of frequent inelastic collisions.

2.2 Introduction

In our solar system, both Saturn and Neptune have ring arcs. Saturn's ring arcs are confined longitudinally due to corotation eccentricity resonances with Saturn's moon Mimas: Aegaeon and its ring arc are in a 7:6 corotation resonance with Mimas (Hedman et al., 2007c; Hedman et al., 2010) (see Figure 2.1), Anthe and its ring arc are in a 10:11 corotation resonance with Mimas (Cooper et al., 2008; Hedman et al., 2009b), while Methone and its ring arc are in a 14:15 corotation resonance with Mimas (Spitale et al., 2006; Hedman et al., 2009b). Neptune's ring arcs are also confined longitudinally (Smith et al., 1989) and move at rates close to a 42:43 corotation resonance with Galatea, which may be the explanation for their confinement (Goldreich et al., 1986; Porco, 1991; Namouni and Porco, 2002). Deviations from this exact rate, however, could support other explanations, like the presence of undetected co-orbital satellites (Salo and Hanninen, 1998; Renner et al., 2014) or a three-body resonance with Galatea and Larissa (Showalter et al., 2017).

The interactions among objects in a mean motion resonance are important for the orbital evolution of satellites and rings. For example, multiple authors have looked at the importance of the nearby Lindblad resonance in maintaining energy among ring arc particles, since we would otherwise expect energy to dissipate due to collisions (Goldreich et al., 1986; Porco, 1991; Namouni and Porco, 2002). Thus far, however, there have not been

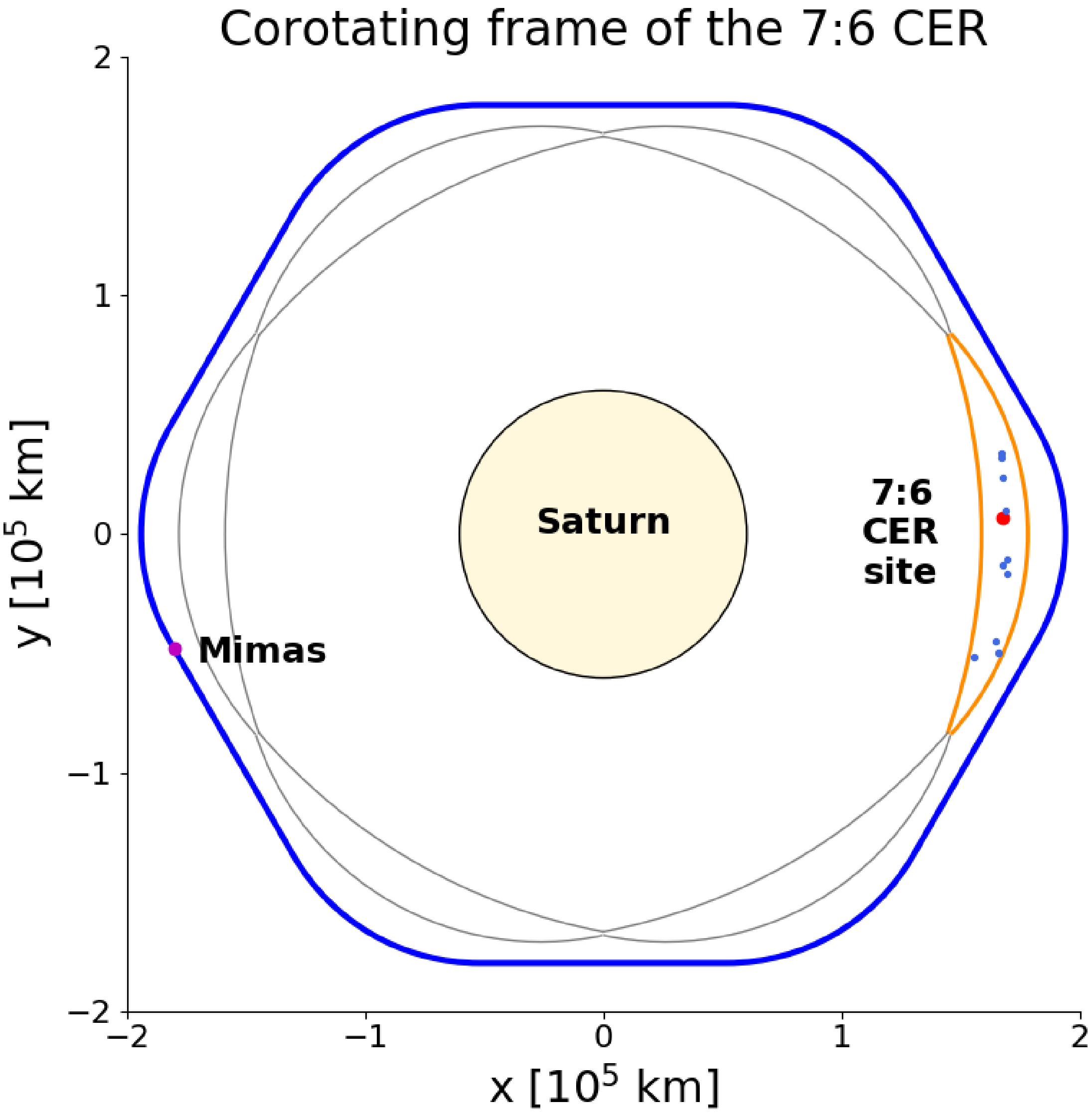

Figure 2.1: The geometry of a corotation eccentricity resonance. In the corotating frame of each of six fixed points of the 7:6 corotation eccentricity resonance with Mimas, Mimas traces out a rounded hexagonal shape (blue). This creates six corotation sites where material can become trapped (within the gray boundaries). Aegaeon's ring arc consists of trapped material in just one of the six corotation sites (within the orange boundary). For illustration purposes, we have exaggerated the eccentricity of Mimas by about a factor of 2 and we have stretched the radial boundaries of the corotation sites as well as the distances the ring arc particles appear from the semi-major axis of the fixed point (using a nonlinear function). The real width and length of the corotation sites are defined in Equations 2.7 and 2.8. The positions of Mimas (magenta) and the ring arc bodies (royal blue for the equal-mass bodies and red for the larger-mass body) depicted here are from their initial positions in one of our simulations (see Section 2.4). The phase space plots in other figures are parametric projections of the single corotation site with the ring arc bodies.

detailed investigations of interactions of multiple bodies within a corotation resonance. Recent work has focused instead on the motions of individual objects in these resonances. For example, El Moutamid et al. (2014) developed the CoraLin model providing a description of a time-averaged Hamiltonian of the three-body system and showed that intermediate distances between the corotation and Lindblad resonances yield a region of chaotic motion. El Moutamid et al. (2017) then studied the capture of massless particles into corotation eccentricity resonances. Muñoz-Gutiérrez and Giuliatti Winter (2017) performed a study on the long-term evolution (10^5 years) of Saturn's moons Aegaeon, Methone, Anthe, and Pallene. Sun et al. (2017) looked at the dynamics of small particles in corotation resonances with Anthe and Methone. Madeira et al. (2018) examined the influence of Aegaeon on μm-sized dust particles, acknowledging that larger particles (cm- to m-sized) could also be present. Although these last studies have discussed satellite perturbations on dust, no study has explored mutual interactions between ring arc bodies. In this work, we consider how interactions among massive bodies in the same corotation eccentricity resonance site affect their orbital evolution on short timescales. We find that the time-averaged Hamiltonian that is so useful for describing three-body motion is no longer appropriate for mutual encounters, which has implications for the stability of arcs where such interactions are common.

In Section 2.3, we cover the background of the three-body problem where the third body is in a corotation eccentricity resonance with the secondary body. In Section 2.4, we describe how we use numerical simulations to investigate the interactions between two or more massive bodies trapped in the same corotation resonance. In Section 2.5, we consider what happens when two or more massive bodies share the same corotation resonance site. In Section 2.6, we describe the results of these simulations, which demonstrate that the time-averaged energy defining the corotation resonance is not conserved.

2.3 Background

In this section, we review mean motion resonances around an oblate primary, body 1, and then discuss the dynamics of the three-body problem where the secondary, body 2, holds a third body, body 3, in a corotation eccentricity resonance. We assume a hierarchical system in which $M_1 \gg M_2 \gg M_3$.

Mean motion resonances occur when the orbital motions of two objects in orbit around a primary body are commensurate with each other. For objects in orbit around giant planets, however, the planet's oblateness splits each resonance into multiple sub-resonances of different types. For a test particle orbiting around an oblate central mass, the gravitational potential is

$$V = -\frac{GM_1}{r}\left[1 - \sum_{i=1}^{\infty} J_{2i}\left(\frac{R}{r}\right)^{2i} P_{2i}\left(\sin\alpha\right)\right] \tag{2.1}$$

where G is the gravitational constant, M_1 is the mass of the primary body, r is the distance between the test particle and the center of M_1, the J_{2i} terms are zonal gravity harmonic coefficients, and the P_{2i} terms are Legendre polynomials in $\sin\alpha$, where the angle α is measured from the equatorial plane of the primary body. These terms in the potential alter the expressions for the particle's mean motion n and radial epicyclic frequency κ (Murray and Dermott, 1999; Renner and Sicardy, 2006):

$$n^2 \simeq \frac{GM}{a^3}\left[1 + \frac{3}{2}J_2\left(\frac{R}{a}\right)^2 - \frac{15}{8}J_4\left(\frac{R}{a}\right)^4 + \frac{35}{16}J_6\left(\frac{R}{a}\right)^6\right] \tag{2.2}$$

$$\kappa^2 \simeq \frac{GM}{a^3}\left[1 - \frac{3}{2}J_2\left(\frac{R}{a}\right)^2 + \frac{45}{8}J_4\left(\frac{R}{a}\right)^4 - \frac{175}{16}J_6\left(\frac{R}{a}\right)^6\right] \tag{2.3}$$

where a is the semi-major axis of the test particle. These extra terms in n and κ cause the locations of resonances with a secondary mass to split. Specifically, for any integer j, a Lindblad eccentricity resonance occurs where

$$jn_{\mathrm{LER}} = \left(j+1\right)n_2 - \dot{\varpi}_{\mathrm{LER}} \tag{2.4}$$

while the corresponding corotation eccentricity resonance occurs where

$$jn_{\mathrm{CER}} = \left(j+1\right)n_2 - \dot{\varpi}_2 \tag{2.5}$$

since the pericenter precession rate is given by

$$\dot{\varpi} = n - \kappa \tag{2.6}$$

Corotation eccentricity resonances exist when the perturbing body has non-zero eccentricity. The eccentricity of Mimas, $e = 0.0196$ (Jacobson, 2010), for example, is enough to provide large corotation sites for Aegaeon, Anthe, and Methone. The main effect of the corotation resonance is to drive oscillations in the perturbed body's semi-major axis and mean longitude around a series of points where Equation 2.5 is exactly satisfied. These points correspond to j equally-spaced corotating longitudes λ_{CER} at the same semi-major axis a_{CER}.

It is useful to depict this motion as well as a body's location with a phase space of corotating longitude vs. semi-major axis, as shown in Figure 2.2. In this phase space, bodies in the corotation resonance follow quasi-elliptical trajectories. The center of the "ellipse" is the phase space location of exact corotation resonance. This is a local potential maximum in a field that is time-averaged over the synodic period between the secondary and tertiary bodies (Goldreich et al., 1986; Sicardy, 1991; Porco et al., 1995; Namouni and Porco, 2002).

The width of a corotation eccentricity resonance (horizontal distance in Figure 2.2), for sufficiently large j, can be approximated as (El Moutamid et al., 2014)

$$W_{\mathrm{CER}} \simeq 4.136\sqrt{|j| e_2 \frac{M_2}{M_1} \frac{a_{\mathrm{CER}}^3}{a_2}} \tag{2.7}$$

where a_{CER} is the semi-major axis of the corotation eccentricity resonance, a_2 is the semi-major axis of the secondary body, e_2 is the eccentricity of the secondary, M_2 is the mass of the secondary, M_1 is the mass of the primary (central) body, and the coefficient 4.136 has absorbed constants as well as combinations of Laplace coefficients (Brouwer and Clemence, 1961).

The length of the corotation eccentricity resonance (vertical distance in Figure 2.2), measured in degrees, is simply

$$L_{\mathrm{CER}} = \frac{360^\circ}{|j|} \tag{2.8}$$

for an inner resonance (replace $|j|$ with $|j+1|$ for an outer resonance). From the width and length, the resulting boundary of the corotation resonance can then be approximated as an ellipse. We can calculate a normalized distance s from exact resonance in phase space to

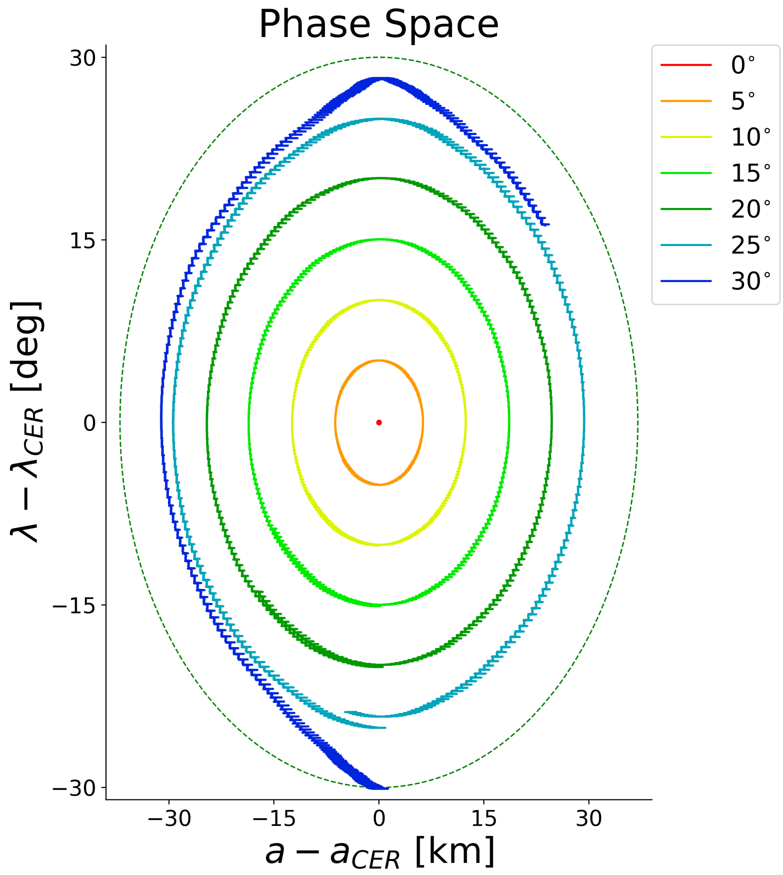

Figure 2.2: A body in a corotation resonance traces out a quasi-elliptical path in phase space, moving in the clockwise direction. The paths traced out in phase space seen here are from separate 4-year simulations in which the third body is initially placed 0, 5, 10, 15, 20, 25, and then 30 degrees of mean longitude behind the exact corotating longitude, and at $a_{\mathrm{CER}} = 167506.5$ km. The dashed ellipse marks an approximate boundary for the corotation resonance, though it can be seen that near the fringe of the resonance site bodies trace out paths that resemble an American football rather than an ellipse. The curves do not quite close on themselves at large distances from the resonance center due to additional perturbations from the Lindblad resonance, which is located at about +19 km.

help our analysis.

$$s^2 = \left(\frac{a - a_{\text{CER}}}{0.62 W_{\text{CER}}} \right)^2 + \left(\frac{\lambda - \lambda_{\text{CER}}}{0.5 L_{\text{CER}}} \right)^2 \tag{2.9}$$

where $s < 1$ for bodies in the corotation resonance and $s > 1$ for bodies outside the corotation resonance. The coefficients in the denominators apply to the 7:6 corotation resonance and are empirically determined such that the phase space distance s remains relatively constant over the course of librations in the corotation resonance.

Table 2.1: Parameters of Saturn used for numerical simulations, from Jacobson et al. (2006)

Parameter	Value
$\mathrm{R}_{♄}$	60268 km
$\mathrm{GM}_{♄}$	37931207.7 $\mathrm{km}^3\mathrm{s}^{-2}$
J_2	1.629071×10^{-2}
J_4	-9.3583×10^{-4}
J_6	8.614×10^{-5}

Table 2.2: Parameters of Mimas used for numerical simulations, corresponding to its position at UTC 2010-100T00:00:00

Parameter	Value
M	$6.597\times10^{-8}\mathrm{M}_{♄}$
x	$8.81807403961\times10^{-4}$ AU
y	$8.80075627975\times10^{-4}$ AU
z	$1.2509303717\times10^{-5}$ AU
$\dot{x}$	$-5.70335493828\times10^{-3}$ AU/day
$\dot{y}$	$5.93108634437\times10^{-3}$ AU/day
$\dot{z}$	$2.10785127451\times10^{-4}$ AU/day

2.4 Methods

To examine the dynamics of multiple bodies in a corotation eccentricity resonance, we numerically simulated the motion of objects with orbits similar to Aegaeon, which orbits Saturn within the 7:6 CER created by Mimas. For orbital simulations, we used Mercury6 code (Chambers, 1999). Our orbital simulations considered Saturn as the central mass and included terms up to J_6 in its gravitational field. The constants used for these simulations were taken from Jacobson et al. (2006) and are found in Table 5.3. Mimas was included in all simulations, with its initial state vectors from an arbitrary date (UTC 2010-100T00:00:00) according to the SPICE kernel sat393.bsp (Acton 1996, Table 5.4).

For each simulation, we modified the initial state vectors of masses we placed in the same 7:6 corotation resonance site with Mimas to set up a system similar to Aegaeon's ring arc. We used time-steps of 0.01 days in order to observe carefully what happens during a close encounter. After an initial test with the Bulirsch-Stoer integrator, we chose the hybrid symplectic/Bulirsch-Stoer integrator with the changeover at 3 Hill radii. Since a libration in the phase space of the 7:6 corotation resonance with Mimas takes about four years (Hedman et al., 2010; Muñoz-Gutiérrez and Giuliatti Winter, 2017), and a close encounter between any two bodies generally occurs twice each libration, ten-year simulations were sufficient to observe an average of 15 close encounters per body per simulation.

Aegaeon's ellipsoidal axes and inferred mean density (Thomas et al., 2013) give a mass estimate of 1.0×10^{11} kg, but encounters with such small masses produce very small changes in the phase space distance s. Hence, in order to better document the changes in the particles' orbits during a close encounter, we consider much larger mass objects: 10 objects with masses of 2×10^{13} kg and (optionally) one object with a mass of 6×10^{14} kg. This preserves the estimated mass ratio of 0.3 of the total mass of all the other bodies in Aegaeon's ring arc to the mass of Aegaeon (Hedman et al., 2010). We verified that increasing the masses changes the results only quantitatively, not qualitatively, by experimenting with smaller masses over larger timescales and by observing that changes in semi-major axis in asymmetric mass interactions scale linearly with mass.

The initial positions of all bodies were distributed randomly in $(e\cos\varpi, e\sin\varpi)$ space with $0.00001 < e < 0.0008$ and $(I\cos\Omega, I\sin\Omega)$ space with $0.00001^\circ < I < 0.0917^\circ$. For every simulation with the more massive body, an additional simulation without the more massive body was performed, but with the same initial positions and velocities given to the other bodies.

After running each orbital simulation, we converted the state vectors at each time-step to geometric orbital elements using the equations and iterative method found in Renner and Sicardy (2006). Using the geometric elements is important when considering orbits around an oblate planet like Saturn because they do not exhibit the artificial orbit-period variations seen in osculating elements.

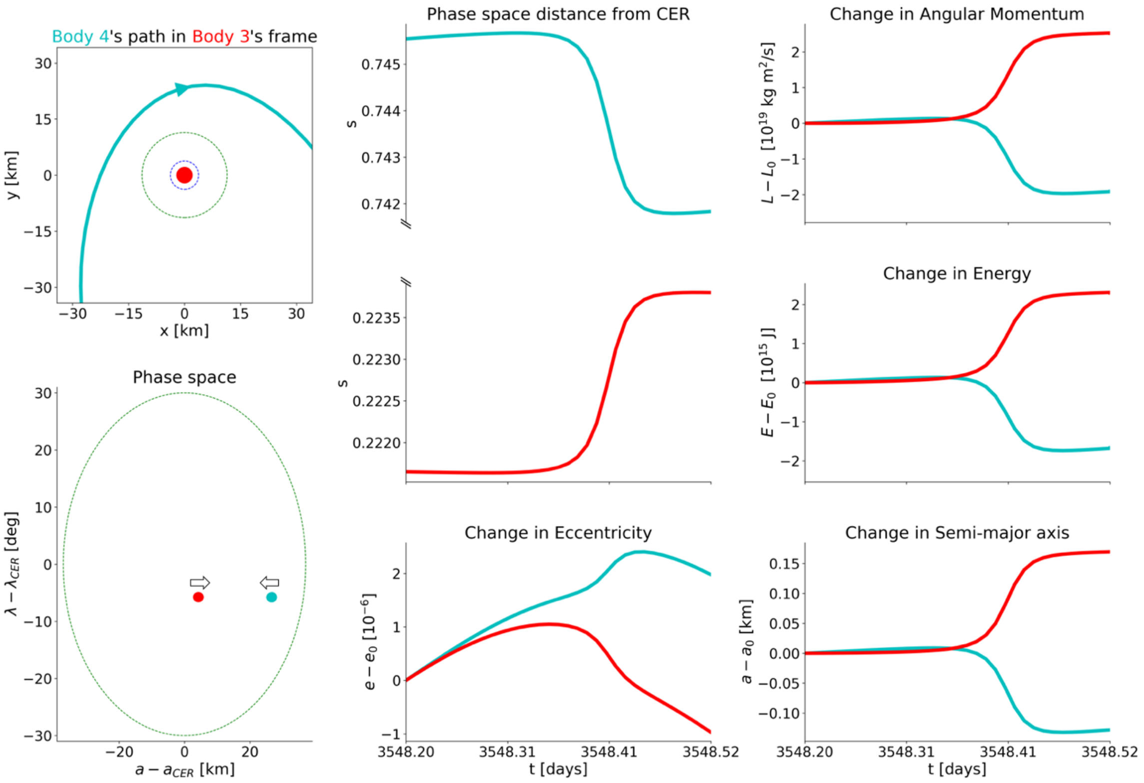

Figure 2.3: A sample close encounter of equal-mass bodies. The result of this close encounter is that one body (cyan) moves closer to exact corotation while the other (red) moves away from exact corotation. The mass of each body in this close encounter is 2×10^{13} kg. The eccentricity at the start of the close encounter, e_0, was 8.078×10^{-4} for body 3 and 6.779×10^{-4} for body 4. The angular momentum at the start of the close encounter, L_0, was 5.0217×10^{25} kg m^2/s for body 3 and 5.0221×10^{25} kg m^2/s for body 4. The total energy at the start of the close encounter, E_0, was -2.2495×10^{21} J for body 3 and -2.2492×10^{21} J for body 4. The semi-major axis at the start of the close encounter, a_0, was 167511 km for body 3 and 167534 km for body 4.

2.5 Results

If we add another body of comparable mass (i.e., $M_3 \simeq M_4$) to the same corotation site, the bodies in the corotation site, which we call body 3 and body 4, can have close encounters with each other. Although they will have slightly different semi-major axes, the forcing due to the nearby Lindblad resonance provides enough eccentricity for the bodies to have a close encounter when they share the same mean longitude, which generally happens twice per libration period. We describe how we quantify these interactions in Section 2.5.1, and summarize the distribution of outcomes in Section 2.5.2.

2.5.1 Quantifying close encounters

We define a close encounter as any time one body is less than 6 Hill radii from another. For each close encounter, we generate a series of plots documenting change in the orbital properties of the two bodies (see Figure 2.3). These plots show the path of one body in the fixed frame of the other, the bodies' trajectories in phase space during the interaction, their phase space distance from exact corotation defined in Equation 2.9, and their changes in semi-major axis, eccentricity, angular momentum, and energy over the course of the interaction.

The top left panel of these plots shows the encounter in the frame where body 3 is fixed, with up being the direction of orbital motion. The dotted blue circle around the red body marks its Hill radius. The dotted green circle around the red body marks 3 Hill radii, which is the boundary inside of which the integrator uses the Bulirsch-Stoer algorithm. The cyan path shows the motion traced out by body 4, with an arrow indicating the direction of motion.

The next plot down shows the paths in phase space of body 3 (red) and body 4 (cyan) during the close encounter. Again, the bodies can interact even though they are at different semi-major axes because of their orbital eccentricities. In most cases, the change in semi-major axis during a close encounter is small compared to the oscillations of semi-major axis over the course of a libration period.

The first two plots of the second column show the evolution over time of the phase space

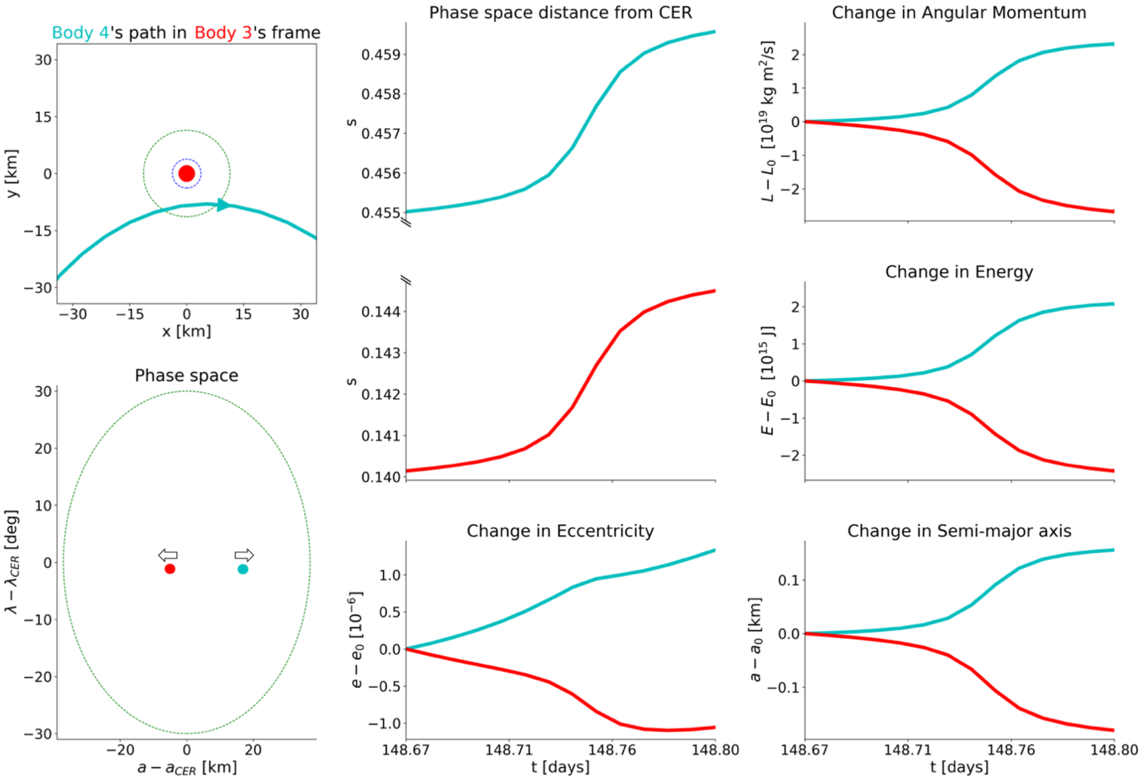

Figure 2.4: Close encounter of symmetric masses in which both bodies move away from exact corotation. The mass of each body in this close encounter is 2×10^{13} kg. The eccentricity at the start of the close encounter, e_0, was 2.418×10^{-4} for body 3 and 6.32×10^{-4} for body 4. The angular momentum at the start of the close encounter, L_0, was 5.0216×10^{25} kg m^2/s for body 3 and 5.0219×10^{25} kg m^2/s for body 4. The total energy at the start of the close encounter, E_0, was -2.2496×10^{21} J for body 3 and -2.2493×10^{21} J for body 4. The semi-major axis at the start of the close encounter, a_0, was 167502 km for body 3 and 167523 km for body 4.

distance from exact corotation. The top one (cyan) is for body 4; the bottom one (red) is for body 3. For the interaction shown in Figure 2.3, body 3 (red) moves away from exact resonance while body 4 (cyan) moves towards exact resonance.

The bottom plot in the second column shows the change over time in eccentricity. The plots in the third column show the change over time in angular momentum, energy, and semi-major axis. An equation for angular momentum in the context of the two-body problem (cf. Equation 2.26 in Murray and Dermott 1999)

$$L = m\sqrt{GMa(1-e^2)} \tag{2.10}$$

shows that angular momentum is proportional to the square root of the semi-major axis. This relation is reflected in the plots shown. When we compute angular momentum, however, we use a more fundamental equation (cf. Equations 2.128-129 in Murray and Dermott 1999):

$$L = m|\vec{r} \times \vec{v}| \tag{2.11}$$

Total energy is conserved during these close encounters as long as it is computed in the fundamental way:

$$E = \sum_{i}^{N} \left(V_{1,i} + \frac{1}{2} m_i v_i^2 \right) - \sum_{i \neq j}^{N} \frac{G m_i m_j}{r_{ij}} \tag{2.12}$$

where $V_{1,i}$ is the potential energy due to the oblate central body as computed in Equation 2.1. Note in Figure 2.3 the changes in L and E have opposite signs for bodies 3 and 4, consistent with the two objects exchanging energy and angular momentum.

2.5.2 Probability of different outcomes

Given the standard three-body picture of the co-rotation resonance, where the sites of exact corotation are treated as (time-averaged) potential maxima, one might expect that conservation of energy would require that if the phase space distance s of one body decreases, that of the other body must increase. In fact, however, we find encounters are equally likely to cause objects to both move in the same direction relative to the resonance center. From our simulations, about 5000 close encounters have been analyzed. In 49% of cases, one body

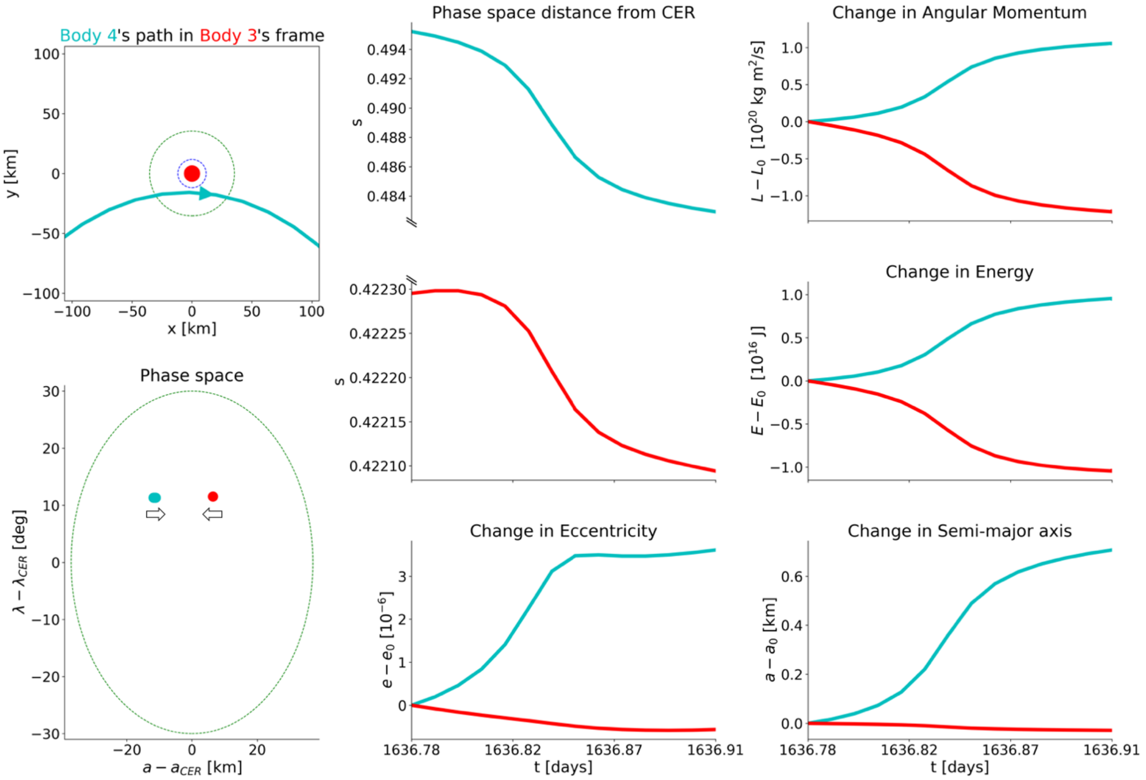

Figure 2.5: Close encounter of asymmetric masses in which both bodies move towards exact corotation. The mass of body 3 (red) is 6×10^{14} kg and the mass of body 4 (cyan) is 2×10^{13} kg. The eccentricity at the start of the close encounter, e_0, was 1.1134×10^{-3} for body 3 and 1.6571×10^{-3} for body 4. The angular momentum at the start of the close encounter, L_0, was 1.5065×10^{27} kg m^2/s for body 3 and 5.0215×10^{25} kg m^2/s for body 4. The total energy at the start of the close encounter, E_0, was -6.7484×10^{22} J for body 3 and -2.2497×10^{21} J for body 4. The semi-major axis at the start of the close encounter, a_0, was 167513 km for body 3 and 167495 km for body 4.

moves closer to exact resonance while the other moves away, like the interaction depicted in Figure 2.3. In 26% of cases, both bodies move away from exact resonance. In 25% of cases, both bodies move towards exact resonance. (With 5000 events the statistical uncertainties in these fractions are all 2%.) Examples of these encounters are shown in Figures 2.4 and 2.5. These encounters explicitly conserve energy and angular momentum, so these unexpected results are not due to an error in the code. The conservation of energy and angular momentum holds even in cases where the bodies have unequal masses, such as the encounter shown in Figure 2.5.

We investigated whether any regions of phase space favored certain outcomes. No obvious dependence on any specific part of phase space for a certain type of encounter outcome to occur can be seen in Figure 2.6. This randomness in outcomes suggests that the long-term evolution of bodies in a corotation eccentricity resonance does not differ qualitatively from the evolution observed in these ten-year simulations.

2.6 Discussion

The above simulations clearly show that close encounters between bodies within a corotation resonance do not conserve the phase space distance s. To understand why this is the case, we first examine the individual encounters shown in Figures 2.3-2.5, and show that the changes in semi-major axis are consistent with the encounter geometries. We then argue that the classical understanding of energy surfaces in corotation resonances is not applicable here because the encounters occur on very short timescales. Finally, we highlight some potential implications of these findings for the stability of ring arcs.

In the close encounter shown in Figure 2.3, body 4 (cyan) passes by ahead of body 3 (red) in their direction of orbital motion (up). Because of this, angular momentum and energy are transferred from body 4 to body 3. This determines which direction the bodies move in phase space. Since at the beginning of the interaction body 3 has a semi-major axis greater than the semi-major axis of exact corotation, and then gains angular momentum and energy, its semi-major axis increases, and it thus moves away from exact corotation. Body 4 also begins the interaction with a semi-major axis greater than the semi-major axis of exact corotation, but because it loses angular momentum and energy, its semi-major axis decreases, so it moves towards exact corotation.

In the close encounters shown in Figure 2.4 and in Figure 2.5, body 4 (cyan) passes by behind body 3 (red), so angular momentum and energy are transferred from body 3 to body 4. In Figure 2.4, body 3 begins the interaction with a semi-major axis less than the semi-major axis of exact corotation, whereas body 4 begins with a semi-major axis greater than that of exact corotation. Since body 3 is losing angular momentum and energy, its semi-major axis decreases, and it moves away from exact corotation. Since body 4 is gaining angular momentum and energy, its semi-major axis increases, so it also moves away from exact corotation.

In Figure 2.5, body 3 begins the interaction with a semi-major axis greater than the semi-major axis of exact corotation, whereas body 4 begins with a semi-major axis less than that of exact corotation. Since body 3 is losing angular momentum and energy, its semi-major axis decreases, and it moves towards exact corotation. Since body 4 is gaining angular momentum and energy, its semi-major axis increases, so it also moves towards exact corotation.

As we can see in these examples, then, it is the combination of the epicyclic phase of the encounters and their locations in phase space that determines which direction the bodies move relative to exact corotation.

In all of these encounters, we can see that energy is transferred from one body to the other, but total energy is conserved. Thus we can see that there is a difference between this energy and the energy maxima usually defined for corotation resonances (Goldreich et al., 1986; Sicardy, 1991; Porco et al., 1995; Namouni and Porco, 2002). This is because the classical picture of corotation resonances involves averaging over many terms in the potential, while these encounters occur over a short timescale where those terms in the potential cannot be ignored. This means that close encounters between bodies within a corotation resonance will disperse particles in phase space in a manner that is largely independent of the corotation sites.

This basic finding has important implications for the stability of ring arcs, particularly dense arcs like those found in Neptune's rings, where inter-particle collisions should be common, and inelastic interactions such as accretion can occur. On the one hand, such interactions could be more apt to disperse material out of the stable corotation sites. On the other hand, dissipative collisions might not necessarily require material to move away from the exact corotation sites. Detailed numerical simulations of collisional ring arcs will likely be needed to properly investigate these issues.

2.7 Acknowledgements

We are grateful to many individuals for useful discussions, especially R. Chancia, J. Ahlers, and D. Hull-Nye. We thank NASA for the support through the Cassini Data Analysis and Participating Scientist Program grant NNX15AQ67G. We also thank an anonymous reviewer for helpful comments.

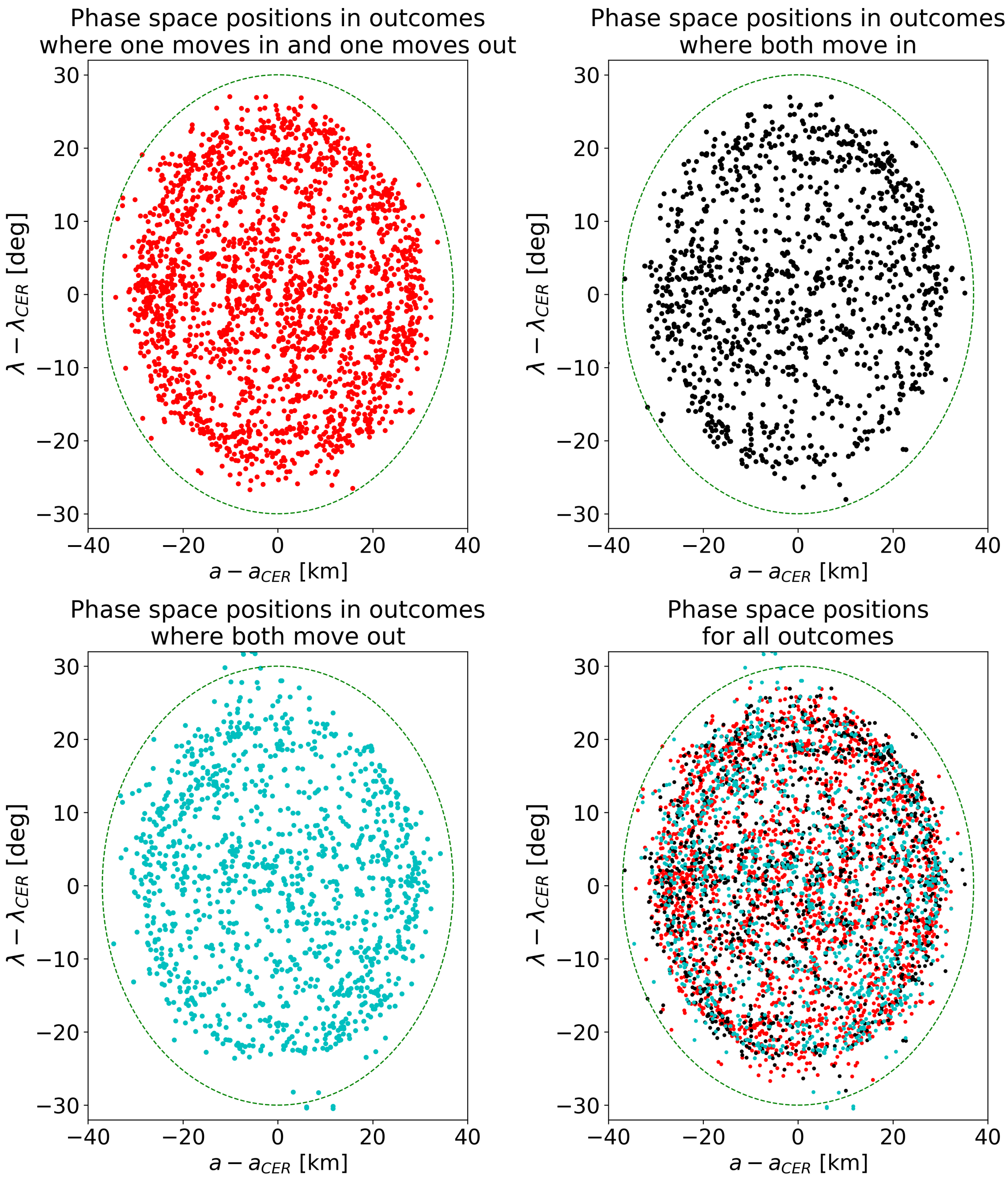

Figure 2.6: Positions in phase space of each body at the beginning of an encounter, organized by the outcome of the encounter. The uniformity in these distributions is evidence that there is no strong trend for a certain outcome based on where the body is in phase space. The randomness in outcomes throughout phase space suggests that the long-term evolution of ring arc particles does not differ qualitatively from the evolution observed in these ten-year simulations.

CHAPTER 3

Modeling Saturn's D68 clumps as a co-orbital satellite system

Joseph A. A'Hearn, Matthew M. Hedman, Douglas P. Hamilton, "Modeling Saturn's D68 clumps as a co-orbital satellite system", *The Planetary Science Journal*, 2, 74, 2021

This project was born during discussions with Matt Hedman about his paper Hedman et al. (2019). I suspected that Salo and Yoder (1988)'s work on co-orbital satellite systems could be applied to help us understand the clumps in Saturn's D68 ringlet. It fell under the Cassini Data Analysis and Participating Scientist Program grant to study the structure, composition, and history of Saturn's faint rings. In practice, this project turned out to be an application of Renner and Sicardy (2004) to a model that approximated the D68 clumps as point-masses. It revealed the fragility of the D68 system beyond our expectations.

3.1 Abstract

The D68 ringlet is the innermost feature in Saturn's rings. Four clumps that appeared in D68 around 2014 remained evenly spaced about 30° apart and moved very slowly relative to each other from 2014 up until the last measurements were taken in 2017. D68's narrowness and the distribution of clumps could either indicate that we have a collection of source bodies in a co-orbital configuration or imply that an outside force confines the observed dust and any source bodies. In this paper we explore the possibility that these four clumps arose from four source bodies in a co-orbital configuration. We find that there are no solutions with four masses that produce the observed spacings. We therefore consider whether an unseen fifth co-orbital object could account for the discrepancies in the angular separations and approach a stable stationary configuration. We find a range of solutions for five co-orbital objects where their mass ratios depend on the assumed location of the fifth mass. Numerical simulations of five co-orbitals are highly sensitive to initial conditions, especially for the range of masses we would expect the D68 clumps to have. The fragility of our

D68 co-orbital system model implies that there is probably some outside force confining the material in this ringlet.

3.2 Introduction: Four long-lived bright clumps in the D ring

A narrow ringlet referred to as D68 lies near the inner edge of Saturn's D ring, about 67,630 km from Saturn's center. From its discovery in Voyager images (Showalter, 1996) through much of the Cassini mission, investigation of D68 focused on its radial profile and phase angle properties (Hedman et al., 2007a). Later studies brought attention to its longitudinal brightness variations (Hedman et al., 2014). In 2014-15, four bright clumps formed and remained relatively evenly spaced with small longitudinal variations about mean separations of 26°, 32°, and 29° (Hedman et al., 2019). Hedman et al. (2019) investigated these clumps in depth and designated them T (trailing), M (middle), L (leading), and LL (leading leading). The most likely explanation for the sudden increase in brightness in the four clump regions of the ringlet is that fine material was released by collisions into or among larger objects located near or within D68. These hypothetical larger objects are called source bodies, whose minimum sizes can be constrained by estimating the amount of material associated with each clump from phase-corrected normal equivalent area values, and whose maximum sizes can be constrained by the fact that they have not been observed directly. The range of masses that would correspond to these size constraints is $10^5 - 10^{10}$ kg. The narrowness of the D68 ringlet and the distribution of clumps could either indicate that there is a collection of source bodies in a co-orbital configuration or imply that there is some outside force confining this material. In this paper we test the first idea by modeling the D68 clumps as a co-orbital satellite system.

The study of the dynamics of co-orbital systems is motivated by the many cases of co-orbital systems we find in our solar system. We are especially interested here in systems in which the co-orbitals have comparable masses. The best known of such systems are the horseshoe orbits of Janus and Epimetheus (Dermott and Murray, 1981b). Co-orbital asteroids have been suggested as the source of Venus's zodiacal dust ring (Pokorný and Kuchner, 2019). Finally, the ring arcs in the Neptunian system have been proposed to be confined by either a corotation resonance with a moon on a separate orbit (Goldreich et al., 1986; Porco, 1991; Salo and Hanninen, 1998; Namouni and Porco, 2002) or a co-orbital resonance with an undetected moon or even multiple moons sharing the same orbit (Lissauer, 1985; Sicardy and Lissauer, 1992; Renner et al., 2014).

In Section 3.3, we analyze potential stable configurations. In Section 3.4, we describe how we use numerical simulations to investigate these scenarios. In Section 3.5, we discuss some remarks for co-orbital systems as well as the possibilities for D68.

3.3 Analysis of potential stable configurations

Here we first review the theory of stable co-orbital objects, and we then apply the theory to the D68 clumps.

3.3.1 Theory

Salo and Yoder (1988) originally examined stationary configurations of equal-mass co-orbital satellites for small N ($N \leq 9$) using a simple first-order theory, neglecting terms of the order $(m/M)^{3/2}$, where m and M are the masses of the satellite and the primary. A numerical search revealed three distinct types of stationary solutions, of which we are here concerned with only one, which Salo and Yoder (1988) label Type Ia: an equilibrium where all the N satellites are most concentrated on the same side of the common orbit. The case where $N = 2$ is the well known Trojan configuration, with an angular separation of 60°. Type Ia configurations are stable for $2 \leq N \leq 8$ but are not found for $N \geq 9$ (Salo and Yoder, 1988). This study, motivated by the D68 clumps, focuses on configurations with $N = 4$ and $N = 5$. Renner and Sicardy (2004) generalized the work of Salo and Yoder (1988) for similar but not necessarily equal masses, which is what we expect for the D68 clumps.

When we define ϕ_i as the longitude of satellite i and $\xi_i = \Delta r_i / r_0$ as its relative radial excursion with respect to its average radius r_0, the relevant equations of motion become (Renner and Sicardy, 2004)

$$\dot{\phi}_i = -\frac{3}{2}\xi_i \tag{3.1}$$

and

$$\dot{\xi}_i = -2 \sum_{j \neq i} m_j f' \left(\phi_i - \phi_j \right) \tag{3.2}$$

where m_j is the mass of satellite j and

$$f \left(\phi \right) = \cos \phi - \frac{1}{2 |\sin \frac{\phi}{2}|}. \tag{3.3}$$

The derivative of $f \left(\phi \right)$ is

$$f' \left(\phi \right) = \sin \phi \left[-1 + \frac{1}{8 |\sin \frac{\phi}{2}|^3} \right]. \tag{3.4}$$

For a co-orbital stationary configuration (Renner and Sicardy, 2004),

$$\xi = 0 \tag{3.5}$$

and

$$\sum_{j \neq i} m_j f' \left(\phi_i - \phi_j \right) = 0. \tag{3.6}$$

Equation 3.6 can be written in matrix form:

$$\begin{pmatrix} 0 & f'_{12} & \cdots & \cdots & f'_{1N} \\ -f'_{12} & 0 & f'_{23} & \cdots & f'_{2N} \\ \vdots & & 0 & & \\ \vdots & & & \ddots & \\ -f'_{1N} & & & & 0 \end{pmatrix} \begin{pmatrix} m_1 \\ m_2 \\ \vdots \\ \vdots \\ m_N \end{pmatrix} = 0_{\mathrm{I\!R}^{\mathrm{N}}} \tag{3.7}$$

Because the $N \times N$ matrix is antisymmetric and depends only on the longitudinal separations ϕ_i between the bodies, for $N \geq 3$ one can always find a set of relative masses that satisfies these equations for any given set of angular separations. This solution, however, might not be physical because one or more of the masses could be negative or zero.

3.3.2 Results

We first considered the observed configuration with four masses separated by angles of 29°, 32°, and 26° because these are the observed separations (Hedman et al., 2019). These separations are closer than the expected separations for an equal-mass situation: 41.498°, 37.356°, and 41.498° (Salo and Yoder, 1988). We therefore solved the above equations for arbitrary masses, using Gaussian elimination, which involved re-ordering the rows, and found that the solution contains a mass ϵ that is calculated as either zero or a small negative number on the order of $10^{-16} - 10^{-19}$, depending on the order in which the rows are solved (most likely a numerical issue involving the limit of double precision numbers):

$$\begin{pmatrix} m_1 \\ m_2 \\ m_3 \\ m_4 \end{pmatrix} = \begin{pmatrix} m_T \\ m_M \\ m_L \\ m_{LL} \end{pmatrix} = \begin{pmatrix} \epsilon \\ 0.55825 \\ 0.00635 \\ 0.4354 \end{pmatrix} \tag{3.8}$$

when we normalize the relative masses such that their sum is 1. Thus, there does not exist a physical solution for the stationary configuration with four objects that would produce four comparably bright clumps.

There are two possible ways that the clumps could still reflect a collection of co-orbital source bodies: the four source bodies could have been librating around the equilibrium location or there could be another massive body in the system that did not produce a visible clump. It is certainly possible for there to be only four non-stationary clumps and for this to be a transient phenomenon. In fact, Hedman et al. (2019) identified slow changes in the clumps' azimuthal separations over time that could be evidence for libration. It is unlikely, however, for the clumps to be on the edge of a libration cycle, due to how azimuthally compact the whole configuration is. The most compact state of a configuration of three is in the symmetric mode when the outer bodies are at their closest approach to the middle body. A similar symmetric mode in a system of four bodies would require the outer two bodies to converge at a faster rate than the middle two bodies. The observed drift rates, however, show the opposite trend, with the middle two clumps drifting at a faster rate than the outer clumps (Hedman et al., 2019).

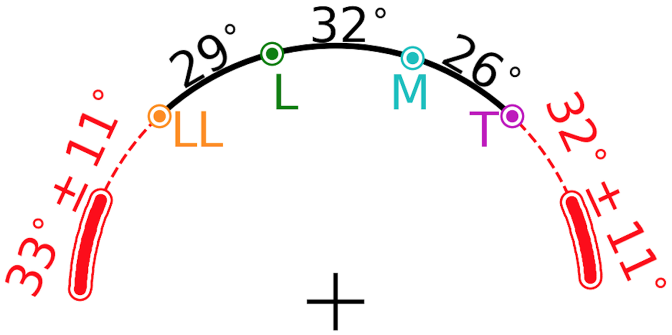

Figure 3.1: The configuration of the four D68 clumps along with the two regions where a fifth object could be. One region is leading, the other is trailing. The direction of orbital motion is counterclockwise.

If, however, the dust around four source bodies was stirred up by an object that passed nearby, it is certainly possible this object could have missed other source bodies in the D68 ringlet. We therefore consider whether there could be an unseen fifth object, whose mass could account for the angular separations we observe between the four known clumps. We explore the approximately 270-degree span of longitudes ahead of Clump LL and behind Clump T. Using the same equations of motion (Renner and Sicardy, 2004), we find physically realistic solutions in two regions, one centered 33° ahead of Clump LL and one centered 32° behind Clump T. These regions each span about 22° in longitude and are mapped out in Figure 3.1. The relative masses of the clumps that correspond to these solutions are plotted in Figure 3.2. The horizontal axis shows the longitude of Object 5 in the same longitude reference system used by Hedman et al. (2019). The left-hand side of the split horizontal axis corresponds to a configuration in which Object 5 is trailing the other D68 clumps; the right-hand side corresponds to a configuration in which Object 5 is leading the other D68 clumps. In more compact configurations (when Object 5 is near longitudes -80 and 55), the middle and outer masses are greater than the second and fourth masses. In less compact configurations (when Object 5 is near longitudes -95 and 75), Object 5's mass would be more than double that of any other mass, and the clump farthest away from Object 5 becomes the least massive while the other three would require comparable masses.

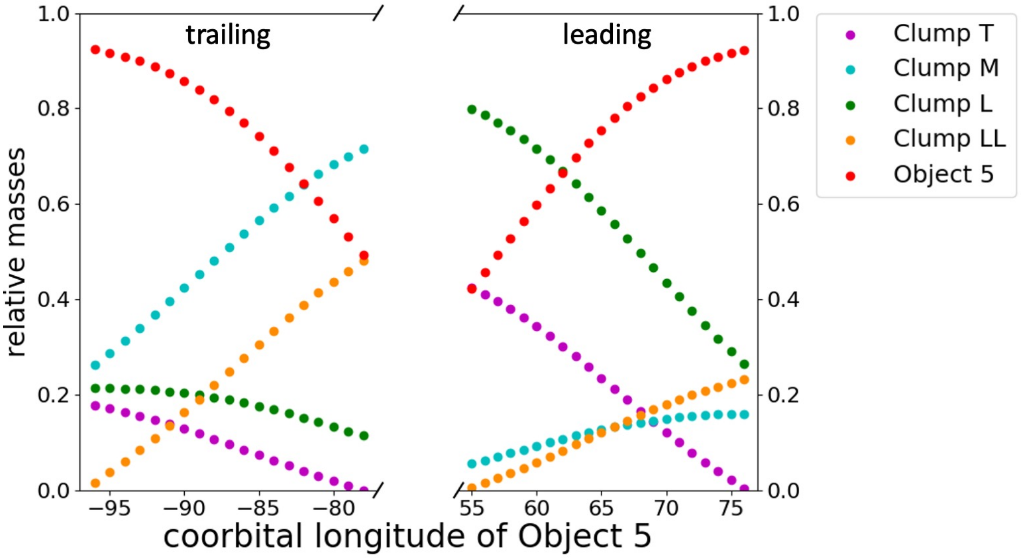

Figure 3.2: This plot shows the relative masses of the five co-orbitals for each possible configuration. Compact configurations are characterized by the more massive bodies in positions 1, 3, and 5. Extended configurations, by contrast, have the most massive object on one end, with the other masses tending to decrease with increasing distance.

3.4 Numerical investigations of the configurations' stability

To further examine the dynamics of a co-orbital system at the semi-major axis of the D68 ringlet and to investigate stability limits, we numerically simulated the motion of point masses at the longitudes of the clump peaks, adding in a fifth point mass at one of the locations permitted by the methods found in Renner and Sicardy (2004). For orbital simulations, we used the hybrid symplectic/Bulirsch-Stoer algorithm in the Mercury6 package (Chambers, 1999). Our orbital simulations considered Saturn as the central mass and included terms up to J_6 in its gravitational field. The constants used for these simulations were taken from Jacobson et al. (2006) and Archinal et al. (2018), converted to the units used in Mercury6, and are found in Table 5.3. We used a time step of 0.02 days, which for D68 corresponds to about one tenth of an orbit.

For the sake of simplicity, we focused on one specific stable solution with the corresponding angular separation of Object 5 in order to do numerical simulations, though other configurations were also investigated, both on the leading and trailing sides, to ensure that our conclusions are general. We focus on a configuration with Object 5 ahead of Clump LL

Table 3.1: Parameters of Saturn used for numerical simulations, from Archinal et al. (2018) and Jacobson et al. (2006)

Parameter	Value
$R_{♄}$	60,268 km
$GM_{♄}$	37931207.7 $km^3\ s^{-2}$
J_2	1.629071×10^{-2}
J_4	-9.3583×10^{-4}
J_6	8.614×10^{-5}

by 33°, as specified in Table 5.4.

Table 3.2: Initial parameters of co-orbitals used for numerical simulations

a	67,627 km	
Body	Mean longitude	Relative mass
T	122°	0.129
M	148°	0.069
L	180°	0.322
LL	209°	0.066
5	242°	0.414

Note: Relative mass is normalized such that the sum of all five masses equals 1.

We explored perturbations to this configuration in semi-major axis and longitude, modifying the initial semi-major axis or longitude for some of the bodies. We also varied their absolute mass, while keeping their relative masses constant, as calculated above (Renner and Sicardy, 2004). Although the highest mass range we expect for the clump source bodies is $10^9 - 10^{10}$ kg because they have not been observed directly (Hedman et al., 2019), we also consider much more massive configurations because these evolve more quickly and in this way clarify how these systems respond to perturbations. Thus we consider three different situations: one with extreme masses of $10^{20} - 10^{21}$ kg (i.e., similar to Enceladus, Tethys, and Dione), one with with masses of $10^{13} - 10^{14}$ kg (i.e., similar to Polydeuces, Pallene, and Daphnis), and one with masses of $10^8 - 10^9$ kg, close to that expected for the D68 source bodies.

In each simulation, we plot the longitudinal evolution of the bodies with respect to a reference longitude, which is calculated for each timestep as

$$\lambda_0 = \arctan \frac{\sum_i^N \sin \lambda_i}{\sum_i^N \cos \lambda_i} \tag{3.9}$$

where λ_i is the mean longitude of body i. This equation works well when the longitudinal oscillations are small. This type of plot gives a quick sense of stability and of orbital evolution.

We verify that the stationary points found using the method of Renner and Sicardy (2004) are indeed stable by placing objects there and finding they do not evolve in 1000-year simulations with high masses ($10^{20} - 10^{21}$ kg; see Figure 3.3). Here we do not explore perturbations in initial longitude or semi-major axis for the high-mass case because the larger masses complicate scalings to the real system.

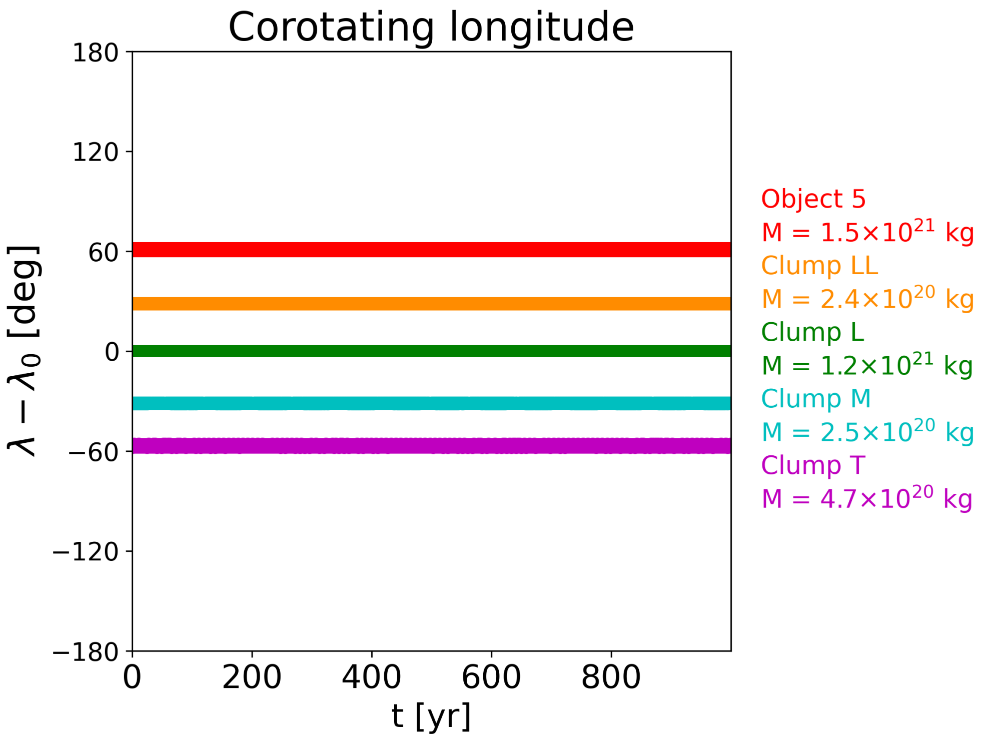

Figure 3.3: With extremely high masses and no perturbations (initial angular separations of 33°, 29°, 32°, and 26°), the system is stable, consistent with the analytic theory.

We consider two types of perturbation, longitudinal and radial, in the medium-mass case, $10^{13} - 10^{14}$ kg. The objects are massive enough that it is easier to demonstrate both stable libration and more chaotic mutual encounters. First, we consider a longitudinal shift in which the system begins in a more compact configuration, and we find that the masses oscillate stably around the solution (see Figure 3.4).

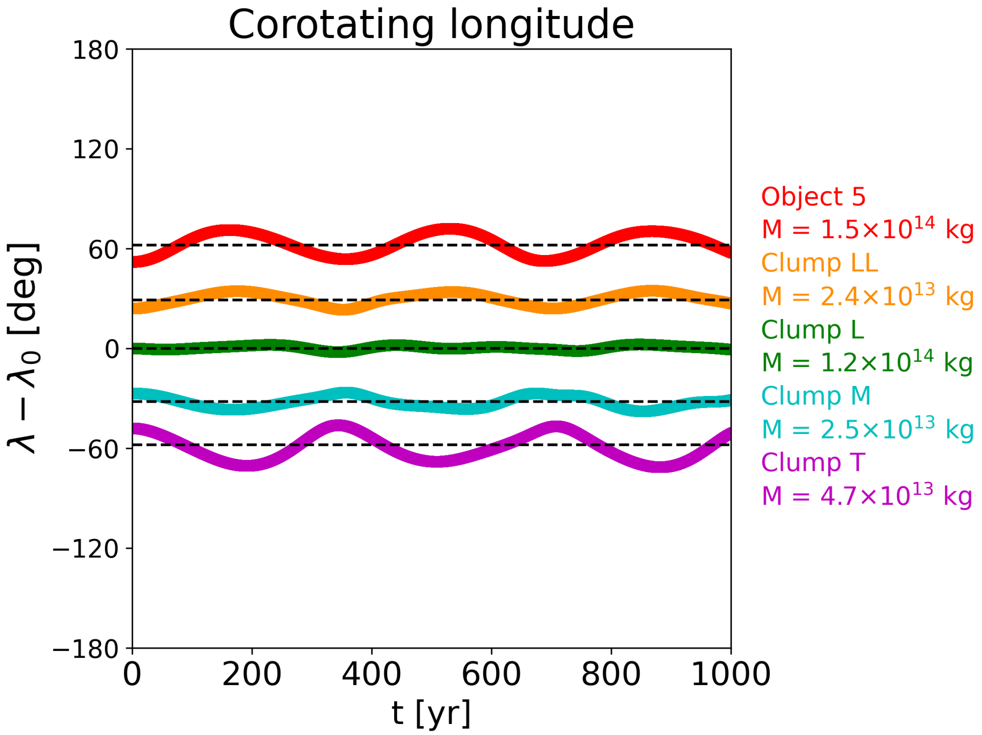

Figure 3.4: Including an initial perturbation to longitudes to start the system in a more compact configuration (with initial angular separations of 28°, 24°, 27°, and 21°), the bodies oscillate around the stable solution, which is indicated by the dashed lines.

Second, we consider radial perturbations in which we modify the initial semi-major axis. We define a critical semi-major axis separation Δa_{crit} which separates small oscillatory motion like that shown in Figure 3.5 from the sort of motion shown in Figure 3.6. We explored through simulations the allowable perturbations to semi-major axis using the mode in which Clump LL is given a positive Δa and Clump M is given a negative Δa, just as in Figure 3.5. We found that, for these relative masses in this specific perturbation mode, the critical semi-major axis separation's relation to absolute mass is best represented as

$$\frac{\Delta a_{\mathrm{crit}}}{a} \simeq 1.06 \left(\frac{m_{\mathrm{clumps}}}{M_{\mathrm{planet}}} \right)^{0.49} \tag{3.10}$$

For the medium-mass case, $\Delta a_{\mathrm{crit}} = 75.8$ m, which occurs in between the cases shown in Figures 3.5 and 3.6, namely, 50 m and 200 m. Perturbations of $\Delta a = 50$ m are small enough that when two of the bodies approach each other, they exchange energy and angular momentum in such a way as to begin receding from each other, similar to the periodic orbital swap of Janus and Epimetheus. Perturbations of $\Delta a = 200$ m are too much for a stable configuration, which results in bodies looping around to approach the other side of the co-orbital system and eventual spreading into multiple orbits via gravitational interactions with the other bodies.

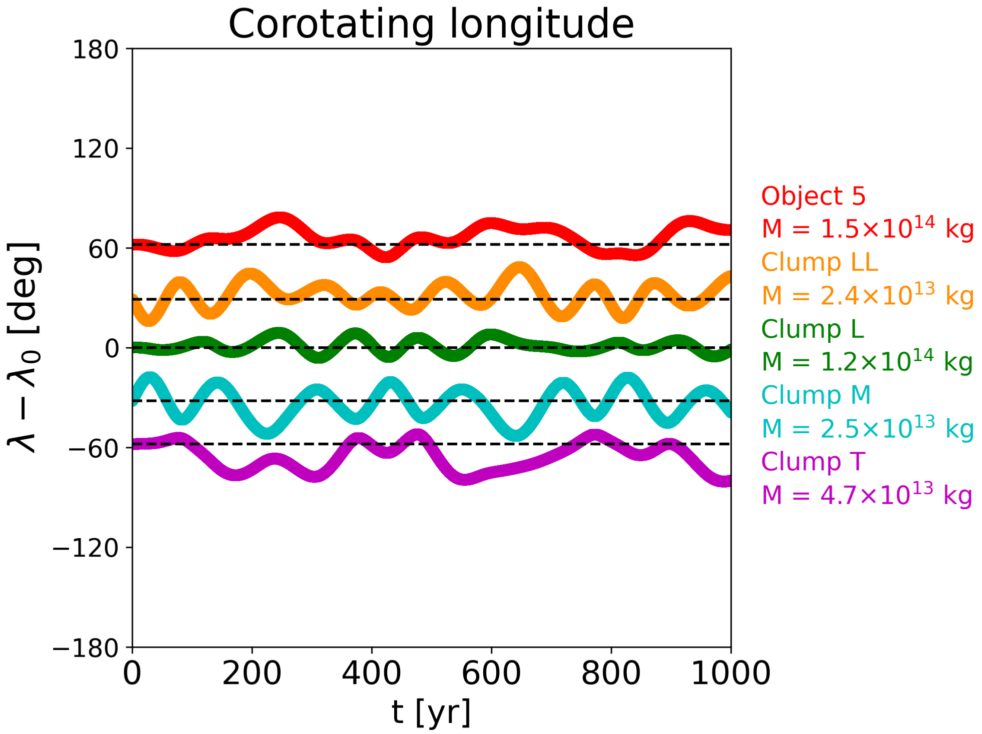

Figure 3.5: With sufficiently small initial perturbations to semi-major axes (50 m for Daphnis-scale co-orbitals), the bodies oscillate around a stable solution, which is indicated by the dashed lines.

To apply our numerical simulations to the D68 clumps, however, we must also consider the dynamics in a low-mass case, $10^8 - 10^9$ kg. For the low-mass case, $\Delta a_{\rm crit} = 27$ cm, which is confirmed by Figure 3.7. With only 1-m perturbations (a 2-m separation in semi-major axis), the point masses drift by each other, with the three closest approaches between the centers of any two bodies as 266 m, 365 m, and 400 m.[1] With a density of 0.5 g/cm^3, spher-

---

[1] We re-examined with a time step of 2×10^{-4} days any approach of two bodies within 1 km from each other, which corresponds to about 15 Hill radii for the largest mass.

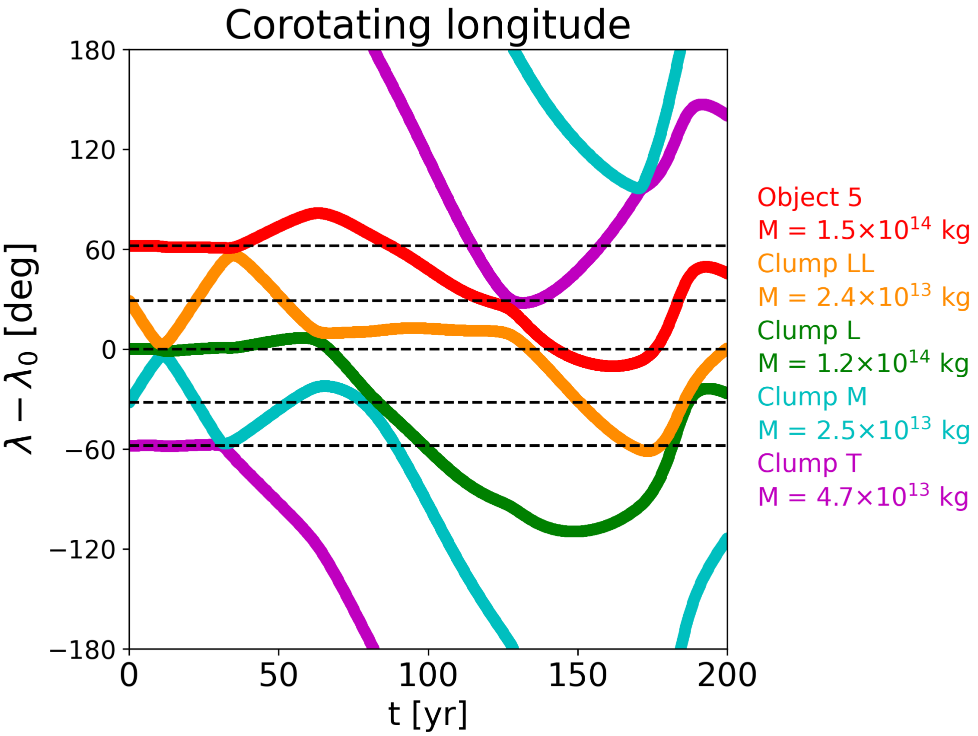

Figure 3.6: With large enough initial perturbations to semi-major axes (200 m for Daphnis-scale co-orbitals), the system becomes unstable when some of the bodies encounter each other.

ical bodies of these masses would have radii ranging from 49 to 89 m. Thus, although these closest approaches would not be collisions, they would still be close enough gravitational encounters to provide significant perturbations, in a range of 4 to 6 Hill radii for the largest mass. We consider such a system to be fragile.

3.5 Discussion and implications

To emphasize how fragile the system is, we can estimate the impulse required to perturb a moonlet's semi-major axis by 1 m, similar to what has been done in Hedman and Bridges (2020). For nearly circular orbits, the standard orbital perturbation equations can describe the rate of change of semi-major axis over time as (Burns, 1976; Hedman, 2018)

$$\frac{\delta a}{\delta t} = 2na\frac{F_p}{F_G} \tag{3.11}$$

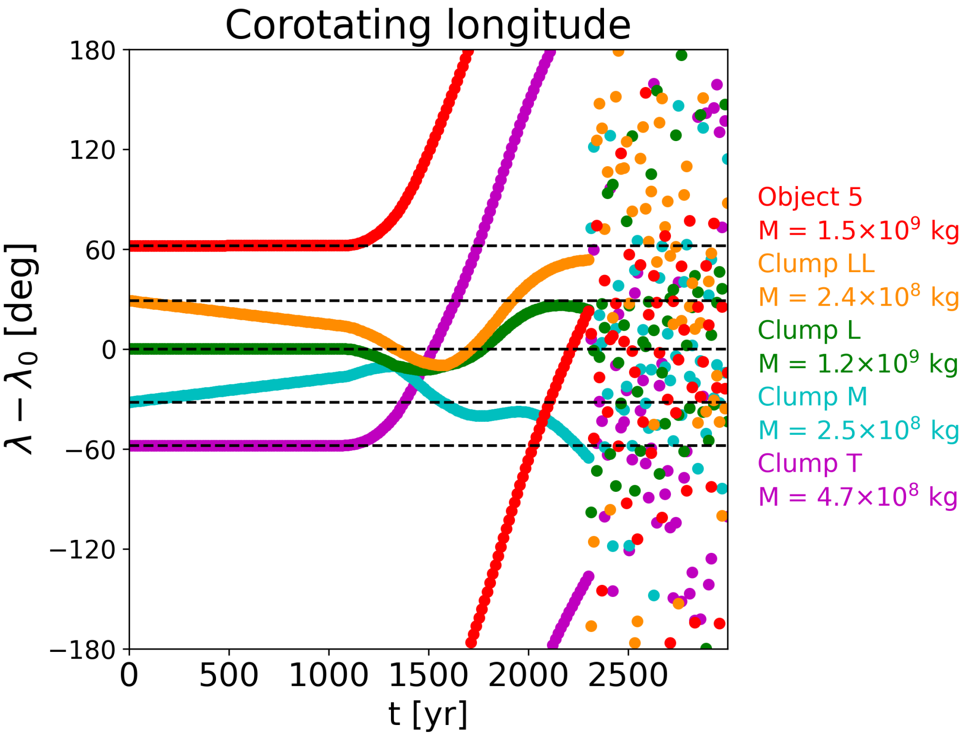

Figure 3.7: With realistic masses, even semi-major axis perturbations of one meter result in system instability. Although low-mass co-orbital systems are fragile, stability could be achieved with the help of an external force.

where the mean motion $n = \sqrt{GM/a^3} \simeq 1751.7°/\text{day}$, F_p is the azimuthal component of the perturbing force, $F_G = GMm/a^2 = n^2am$ is the gravitational force on the moonlet from the planet's center, M is the planet's mass, and m is the moonlet's mass. The moonlet will thus undergo a semi-major axis change δa upon receiving an azimuthal impulse

$$F_p\delta t = \frac{F_G}{2na}\delta a = \frac{1}{2}nm\delta a. \tag{3.12}$$

With the range of masses we use for our low-mass case, the impulse required to perturb a moonlet's semi-major axis by 1 m ranges from 4.2×10^4 kg m/s to 2.7×10^5 kg m/s. For any collision between a moonlet and interplanetary debris, the impact speed would be comparable to the D68 orbit speed $v = na \simeq 24$ km/s. Dividing the range of impulses by this orbit speed, we get a range of masses roughly from 2 kg to 10 kg for the interplanetary impactor. Assuming a density of 0.5 g/cm^3, the piece of interplanetary debris would need to be 0.1 m to 0.2 m in radius. The estimated cumulative influx rate Φ for debris of this size is around $10^{-17}/\mathrm{m}^2/\mathrm{s}$ (Tiscareno et al., 2013). Thus the rough timescale $t \simeq 1/\Phi A$ on which we can expect such a collision, using the cross-sectional area A for moonlets with radii of 49 m to 89 m, corresponds to a range from 130,000 years to 420,000 years, but this is the impact timescale for just one of the objects. Because an impact into any of the objects can break the system, we can adjust the system timescale to about 40,000 years by adding their cross-sectional areas together. We therefore cannot expect a co-orbital configuration at D68 to last longer than a few tens of thousands of years. For this reason we call the system fragile and find it unlikely that a co-orbital system could explain the orbital evolution of the clumps or the ringlet.

Consequently, we look for other resonances that could drive the orbital evolution of the clumps or the ringlet. It is unlikely that a corotation resonance with any satellite is responsible for the clumping of material into ring arcs. A 30° separation between clumps would be the result of a 12-fold pattern at the D68 semi-major axis. A 12-fold pattern could be caused by a 13:12 corotation resonance with an external perturber or an 11:12 corotation resonance with an internal perturber. A 13:12 corotation resonance with an external perturber would require a perturber at a semi-major axis of 71,300 km, which is not as far out as D72, the structure closest to D68. An 11:12 corotation resonance with an internal perturber would require a perturber at a semi-major axis of 63,800 km, which is a few thousand km away from Saturn's equatorial radius (60,268 km). There is no evidence for any moons or ringlets in these regions. Moreover, no results came from a numerical search for corotation resonances up to fourth-order between D68 and Janus, Mimas, Enceladus, Tethys, Dione, Rhea, or Titan.

It is possible that a resonance of some sort with Saturn itself could be responsible for the D68 clumping. The outer Lindblad resonance of Saturn's $\ell = 5$, $m = 3$ oscillation mode is located in the D68 region, reported first at 67,625 km ± 550 km (Marley and Porco, 1993) and more recently at roughly 67,550 km (Marley, 2014). Although Lindblad resonances do not confine material, each such resonance can be associated with a corotation resonance, which can confine material. To locate these corotation resonances, we computed the radii at which the mean motion (using the second-order equation from Renner and

Table 3.3: Predicted corotation resonance locations, the r_{M14} column corresponding to our predictions based on the pattern periods reported in Marley (2014), the r_{M19} column corresponding to our predictions based on the pattern speeds reported in Mankovich et al. (2019)

ℓ	m	r_{M14} (km)	r_{M19} (km)
8	6	67,852	67,663
3	3	67,732	67,932
2	2	66,132	67,235

Sicardy 2006) matches the pattern speeds associated with the modes reported in Marley (2014) and Mankovich et al. (2019). The modes that produce corotation resonances near D68 are listed in Table 3.3. Because the pattern speed is dependent on Saturn's structure, any of these modes could possibly be responsible for providing a corotation resonance to confine D68 material. Mode splitting or mixing could also be involved (Fuller, 2014), allowing the locations of these resonances to fall at slightly different radii than what we can compute. For a corotation resonance of one of these modes to explain the D68 clumping, it would require a planet-based angle that moves at a speed comparable to D68's mean motion. Although the set of angular separations among the clumps favors a 12-fold pattern, it is also possible for them to be confined to within the libration longitude of one or a few stable points of a lower m mode, and then be spaced out within that external potential. Perhaps there is a set of co-orbital moonlets that are trapped together and librating within a larger potential, similar to Renner et al. (2014)'s model of the Neptune ring arcs. Radial oscillations of ± 10 km have been observed for the D68 ringlet with an estimated period of 14-15 years (Hedman et al., 2014), though the clumps are drifting more slowly than the rest of the ringlet (Hedman et al., 2019). These radial oscillations could be evidence for that libration.

In conclusion, we have tested and ruled out long-term stable co-orbital configurations as an explanation for the spacing of the D68 clumps. We therefore predict that either the clumping is a transient phenomenon, or that an external mechanism is trapping the clumps in this region.

3.6 Acknowledgements

We are grateful to many individuals for useful discussions, especially P. Ricker for guiding J. A'Hearn's initial studies on co-orbitals; B. Sicardy, M. El Moutamid, and M. Ćuk for insightful questions and clarifications at the 2019 DDA meeting; H. Salo for helpful correspondence, and two anonymous reviewers for their helpful comments that have improved this paper. We also thank NASA for the support through the Cassini Data Analysis and Participating Scientist Program grant NNX15AQ67G.

CHAPTER 4

Ring Seismology of the ice giants Uranus and Neptune

Joseph A. A'Hearn, Matthew M. Hedman, Christopher R. Mankovich, Hima Aramona, Mark S. Marley, "Ring Seismology of the Ice Giants Uranus and Neptune", submitted to *The Planetary Science Journal* on March 7, 2022, reviewer reports returned on April 12, 2022, in revision

This project had been discussed for years by Matthew Hedman and Mark Marley. As I was wrapping up other projects, it was decided that I could take the lead on this one. This project was supported by two separate Solar System Workings grants, initially one on Uranian ring dynamics and constraints on Uranus's internal structure from occultation data, and later by one on seismological studies of the ice giants, which this project more directly addresses. For this project I needed to learn how to run the stellar oscillation code `GYRE`*, and Chris Mankovich had recently used it for Saturn, so he became a guide for me through much of this project. Chris produced the shallow Uranus model and the Neptune model, as well as a Saturn model that I used early on for testing. Hima worked under Chris during the summer of 2021 and produced thin, medium, and thick Uranus models. When I picked up the pace on this project in order to submit it for publication before requesting to proceed with my dissertation, my co-authors were able to support me and make many suggestions that improved the text of this paper.*

4.1 Abstract

We assess the prospect of using ring seismology to probe the interiors of the ice giants Uranus and Neptune. We do this by calculating normal mode spectra for different interior models of Uranus and Neptune using the stellar oscillation code `GYRE`. These spectra provide predictions of where in these planets' ring systems the effects of interior oscillations might be detected. We find that f-mode resonances with azimuthal order $m = 2$ or $7 \leq m \leq 19$

fall among the inner rings (6, 5, 4, α, and β) of Uranus, while f-mode resonances with $2 \leq m \leq 12$ fall in the tenuous ζ ring region. In addition, f-mode resonances with $m = 2$ or $6 \leq m \leq 13$ may give azimuthal structure to Neptune's tenuous Galle ring. We also find that g-mode resonances may fall in the middle to outer rings of these planets. Although an orbiter is most likely required to confirm the association between any waves in the rings and planetary normal modes, the diversity of normal mode spectra implies that identification of just one or two modes in the rings of Uranus or Neptune would eliminate a variety of interior models, and thus aid in the interpretation of Voyager observations and future spacecraft measurements.

4.2 Introduction

Three decades after the Voyager flybys of Uranus and Neptune, our knowledge of their internal structure and composition is still quite limited (Helled and Fortney, 2020). The ice giants Uranus and Neptune represent a distinct class of planets with radii between those of terrestrial worlds like Earth and Venus and gas giants like Jupiter and Saturn. The recent discovery that Neptune-mass exoplanets are common (Suzuki et al., 2016) motivates the exploration of the ice giants in our own solar system.

The deep interiors of the ice giants Uranus and Neptune are of special interest because their internal structure and composition are distinct from the gas giants Jupiter and Saturn. Their measured densities suggest that Uranus and Neptune have substantial amounts of carbon, nitrogen, oxygen, sulfur, and silicon, which form compounds like water, ammonia, methane, and silicate minerals (Podolak et al., 2019). At the high pressures and temperatures of planetary interiors, these "rocks" and "ices" display interesting properties. Water, for example, can enter a superionic state where the oxygen atoms become a lattice and the hydrogen nuclei are free to move, which may play a role in explaining the non-axisymmetric non-dipolar magnetic fields of Uranus and Neptune (Cavazzoni et al., 1999; Wilson et al., 2013). Although numerical calculations and laboratory experiments are providing better constraints on these exotic phases of these materials (Knudson et al., 2012; Bethkenhagen et al., 2017; Millot et al., 2018, 2019; French and Nettelmann, 2019), there remain many uncertainties regarding important parameters such as the mixing properties of the various compounds. In addition, both the overall breakdown and spatial distributions of hydrogen, helium, water, ammonia, methane, and silicates within the planets are poorly constrained.

While the interiors of Uranus and Neptune remain largely hidden, their ring systems are available for easier observation. Recent analyses of Saturn's rings have demonstrated that certain ring features are likely generated by resonances with normal modes inside the planet (Hedman and Nicholson, 2013; Hedman et al., 2014; French et al., 2016, 2019; Hedman et al., 2019; French et al., 2021; Hedman et al., 2022), confirming predictions made by Marley and Porco (1993) and providing new insights into that planet's interior. Furthermore, Marley et al. (1988) performed preliminary calculations and found that resonances with a few Uranian normal modes could potentially fall close to some of the Uranian rings (see Table 5.5 in the Appendices). This paper therefore seeks to build upon that work and establish which planetary normal modes are most likely to fall close to the rings of Uranus and Neptune and thus are the most promising candidates for performing ring seismology at the ice giants.

In Section 4.3, we provide a brief overview of ring seismology and summarize the current state of knowledge about the ring systems. In Section 4.4, we describe the interior models that we use, and then we explain how we analyze the gravitational potential and calculate the resonance locations. In Section 4.5, we report the locations of these resonances and compare them with relevant structures in the ring systems of the two planets. In Section 4.6, we discuss which of the planetary normal mode resonances are most likely to be detectable in the rings, with remarks on several individual rings of interest. Complete tables of mode frequencies and associated resonance locations are provided in the Appendices.

4.3 Background

Before describing our methods for computing normal mode resonance locations, we first provide a brief overview of giant planet seismology in Subsection 4.3.1 and the relevant features in the rings of Uranus and Neptune in Subsection 4.3.2.

4.3.1 Overview of ring seismology

Planetary oscillations can be decomposed into a set of normal modes, each of which oscillates at a frequency that depends on the planet's profiles of density, adiabatic sound speed, and rotation frequency. Familiar families of oscillation modes include g-modes, whose restoring force is buoyancy, and p-modes, whose restoring force is pressure. Three numbers characterize planetary normal-mode oscillations: the number of radial nodes n, the spherical harmonic degree ℓ, and the azimuthal wavenumber m. In this paper, we adopt the convention that $m > 0$ correspond to prograde modes, i.e. modes that propagate in the same direction as the planet's rotation. While the mode amplitude spectrum is generally unknown, for the simplest assumption of energy equipartition, the strongest perturbations in the planet's gravitational field are produced by the fundamental modes ($n = 0$; f-modes), which can arise from a combination of predominantly gravity but also pressure as the restoring force (Unno et al., 1979). Saturn's f-modes, for example, produce the most obvious features in its rings (Hedman and Nicholson, 2013; Hedman et al., 2014; French et al., 2016, 2019, 2020; Hedman et al., 2019), as predicted by Marley and Porco (1993). For this reason, we will primarily consider the f-modes here.

Because the oscillation frequencies depend on the planet's density profile, measurements of these frequencies can probe the planet's internal structure. Efforts to detect oscillations with visible photometry, which were apparently successful for Jupiter (Gaulme et al., 2011), have not yet been successful for the ice giants (Rowe et al., 2017; Gaulme, 2017). Friedson (2020) found that for reasonable amplitudes, detection of pressure or temperature variations due to ice giant normal modes is not as promising as the prospect of detecting their gravitational influence on an orbiting spacecraft.

Fortunately, we can potentially also detect planetary normal modes by treating the ring material that orbits the planet as a seismograph. Any even $\ell - m$ mode is symmetric about the equator and would generate a Lindblad resonance in ring material, which excites density waves; whereas any odd $\ell - m$ mode is antisymmetric about the equator and would generate a vertical resonance, which excites bending waves. The $\ell = m$ modes are the modes that are expected to be the most easily observable at their Lindblad resonance locations because the amplitude of the gravitational perturbation in the ring plane suffers no destructive interference due to latitudinal variations in the phase of the planetary oscillation. Because Saturn's rings are the largest in our solar system and the dataset on them was the most extensive, they were naturally the first target for ring seismology. Voyager images and radio occultation profiles of Saturn's rings revealed spiral density waves and bending waves. Some of these waves could be explained in terms of resonances with Saturn's moons, but other waves in the C ring were far from any known satellite resonance (Rosen et al., 1991). Meanwhile, Marley (1991) and Marley and Porco (1993), building upon ideas from Stevenson (1982), showed that certain normal modes in Saturn's interior could cause gravitational perturbations in the C ring, and proposed potential correlations between some of the waves and specific planetary f-modes. Once the Cassini mission arrived at Saturn, new waves were detected (Baillié et al., 2011) and several features were confirmed to be generated by resonances with planetary oscillations and asymmetries (Hedman and Nicholson, 2013; Hedman et al., 2014; French et al., 2016, 2019; Hedman et al., 2019; French et al., 2021; Hedman et al., 2022). These studies yielded the azimuthal wavenumber and the precise frequency for a set of planetary normal modes that provide evidence for a stably stratified layer within the planet (Fuller, 2014), an estimate for Saturn's bulk rotation rate (Mankovich et al., 2019), evidence for a diffuse core (Mankovich and Fuller, 2021), and constraints on differential rotation (Dewberry et al., 2021).

4.3.2 The rings and inner moons of Uranus and Neptune

Table 4.1 displays the semi-major axes and eccentricities of the eight innermost Uranian moons and the five innermost Neptunian moons. Table 4.2 shows the semi-major axes and widths of the inner Uranian and Neptunian rings.

The Uranian ring system includes three broad rings (ζ, ν, and μ) and ten narrow rings (6, 5, 4, α, β, η, γ, δ, λ, and ϵ). The innermost Uranian moons, Cordelia and Ophelia, each with diameters of $\sim$ 40 km (Karkoschka, 2001), flank the λ and ϵ rings and play a role in shepherding the ϵ ring (French et al., 1991). The narrow rings except the λ ring are optically thick at visible wavelengths and are expected to be dominated by centimeter- to meter-sized particles (Nicholson et al., 2018). Several small moons of diameters 40-135 km

moon	a (km)	e
moons of Uranus		
Cordelia	49,752	0.00026
Ophelia	53,763	0.00992
Bianca	59,166	0.00092
Cressida	61,767	0.00036
Desdemona	62,658	0.00013
Juliet	64,358	0.00066
Portia	66,097	0.00005
Rosalind	69,927	0.00011
Cupid	74,392	-
Belinda	75,256	0.00007
Perdita	76,417	0.00329
Puck	86,004	0.00012
Mab	97,736	0.00254
moons of Neptune		
Naiad	48,228	0.00014
Thalassa	50,075	0.00019
Despina	52,526	0.00027
Galatea	61,953	0.00020
Larissa	73,548	0.00121
Hippocamp	105,253	0.00001
Proteus	117,647	0.00047

Table 4.1: Semi-major axes a and eccentricities e of the inner moons of Uranus, from Jacobson (1998) and Showalter and Lissauer (2006); and of Neptune, from Brozović et al. (2020).

(Ophelia, Bianca, Cressida, Desdemona, Juliet, and Portia; Karkoschka 2001) are located between the ϵ and ν rings, and several more, of diameters 20-160 km (Rosalind, Cupid, Belinda, Perdita, Puck, and Mab Karkoschka 2001; Showalter and Lissauer 2006), between the ν and μ rings. Portia and Puck are the largest moons in these regions, with diameters of 135 and 160 km, respectively. Beyond Mab are the five largest Uranian moons: Miranda, in a class of its own with a diameter of 470 km; and then Ariel, Umbriel, Titania, and Oberon, with diameters of 1150-1580 km (Thomas, 1988).

With such a quantity of moons exterior to the narrow rings, it is important to distinguish planetary normal mode resonances from resonances with satellites. A wave generated by a Lindblad resonance with an exterior moon propagates outward, whereas a wave generated by a Lindblad resonance with an interior moon or with most planetary normal modes propagates inward. Because we know where the moons are, we can calculate where their

ring	$\bar{a}$ (km)	$\bar{a}e$ (km)
narrow rings of Uranus		
6	41,838	43
5	42,235	80
4	42,572	45
α	44,719	34
β	45,661	20
η	47,176	-
γ	47,627	5
δ	48,301	-
λ	50,024	-
ϵ	51,150	406
broad rings of Uranus		W (km)
ζ (Voyager)	38,300	2500
ζ (Keck)	39,600	3500
ν	67,300	3800
μ	97,700	17,000
rings of Neptune		W (km)
Galle	42,000	2,000
Le Verrier	53,200	100
Lassell	55,200	4,000
Arago	57,200	-
Galatea co-orbital	61,953	-
Adams	62,933	15 (in arcs)

Table 4.2: Parameters of the rings of Uranus, from Nicholson et al. (2018); and of Neptune, from de Pater et al. (2018). $\bar{a}$ is the mean semi-major axis.

Lindblad resonances fall. Some of these line up nicely with some of the outer rings of Uranus, but none of them line up well with the inner rings (Hedman and Chancia, 2021). For example, the 6:5 resonance with Ophelia falls within the γ ring (Porco and Goldreich, 1987; Hedman and Chancia, 2021), even though its kinematics also includes $m = 0$ and $m = 1$ normal modes (French et al., 1991). The ϵ ring is shepherded by Cordelia and Ophelia: its inner edge coincides with the 24:25 outer eccentric resonance with Cordelia, while the outer edge coincides with the 14:13 inner eccentric resonance with Ophelia (Goldreich and Porco, 1987; French et al., 1991; French and Nicholson, 1995; Nicholson et al., 2018). The η ring's kinematics are influenced by a 3:2 inner Lindblad resonance with Cressida (Chancia et al., 2017). Finally, the δ ring's kinematics are well modeled by a single $m = 2$ normal mode of the ring itself (French et al., 1991). Nevertheless, no known satellite resonances are found close to the 6, 5, 4, α, and β rings.

Neptune has one large moon, Triton, which orbits with a high inclination and in the retrograde direction. Proteus orbits Neptune about one third the distance to Triton and is less than 1/500 the mass of Triton (Davies et al., 1991; Stooke, 1994), but is Neptune's next largest moon and can be considered the outermost of the inner moons. The other inner moons, from outward in, are the recently discovered 35-km diameter moon Hippocamp (Showalter et al., 2019); then three moons of diameters of 150-200 km, namely, Larissa, Galatea, and Despina; and finally Thalassa and Naiad, which have diameters of 60-80 km (Karkoschka, 2003).

de Pater et al. (2018) recently reviewed the current state of our knowledge of Neptune's rings. Neptune has two broad faint rings, the Galle ring and the Lassell ring, and four narrow rings: the Le Verrier ring, the Arago ring, an unnamed ring that is co-orbital with Galatea, and the Adams ring (see Table 4.2). The optical depth of the Le Verrier ring is comparable to that of the Adams ring outside of the arcs, while the optical depth of the Galle and Lassell rings is two orders of magnitude lower (Porco et al., 1995). It is still not entirely clear how any of these narrow rings are confined, and the rings seem to lack the fine-scale structure that Saturn's rings have.

4.4 Methods

In this Section, we first describe the interior models we use in Subsection 4.4.1. Then we show how we identify the sources of gravitational potential perturbations in Subsection 4.4.3. Last, we describe how we calculate the resonance locations in Subsection 4.4.4.

4.4.1 Interior models

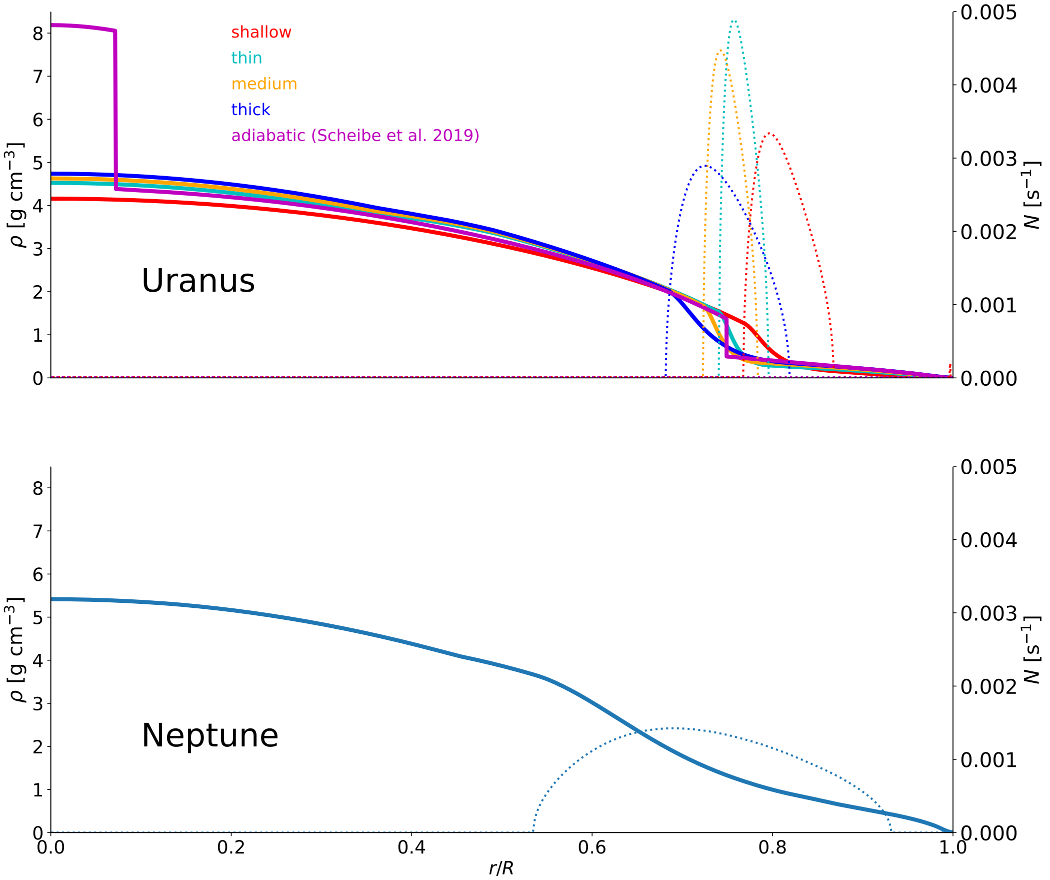

Figure 4.1: Density (solid lines) and Brunt-Väisälä frequency (dotted) for models of Uranus (top) and Neptune (bottom) as functions of the fractional radius r/R. The scales of the y-axes are set equal for both the top and bottom panels for easier comparison between Uranus and Neptune models.

The adiabatic normal mode spectrum for a star or planet depends on the profile of mass density ρ, adiabatic sound speed c, and rotation rate Ω. The adiabatic sound speed c is defined (Unno et al., 1979)

$$c^2 = \Gamma_1 \frac{P_0}{\rho_0}, \tag{4.1}$$

where P_0 and ρ_0 are the pressure and density of the unperturbed state, and the adiabatic exponent Γ_1 is

$$\Gamma_1 = \left(\frac{\partial \ln P}{\partial \ln \rho} \right)_{\mathrm{ad}}. \tag{4.2}$$

Non-adiabatic regions are characterized by a non-zero Brunt-Väisälä frequency N:

$$N^2 = -\frac{GM_r}{r} \left(\frac{d \ln \rho}{d \ln r} - \frac{1}{\Gamma_1} \frac{d \ln P}{d \ln r} \right), \tag{4.3}$$

where G is the gravitational constant, M_r is the mass interior to the radius r. For clarity, M without the subscript r will refer to the total mass of the planet. The Brunt-Väisälä frequency N quantifies the angular frequency with which a small parcel of gas oscillates radially with positive or negative buoyancy under local pressure balance with its surrounding gas (Unno et al., 1979).

Here we consider spherically symmetric models so that $\rho = \rho(r)$, $c = c(r)$, and make the further assumption of rigid rotation so that $\Omega(r) = \Omega = \text{constant}$. Although the cloud-level jet streams alone guarantee some degree of differential rotation in Uranus and Neptune (Kaspi et al., 2013), the uncertainty in their underlying bulk rotation rates means that rigidly rotating models are sufficient for our purposes.

The system of equations required to solve for the frequencies of the normal mode spectrum is found in classic works like Unno et al. (1979), and there is now a publicly available and extensively validated asteroseismology software package called `GYRE` that solves these equations (Townsend and Teitler, 2013). This code has recently been used successfully for Saturn (Mankovich et al., 2019; Markham et al., 2020).

Most models of the interiors of the ice giants make a number of simplifying assumptions, such as a three-layer structure: a rock-rich core, a water-rich envelope, and a hydrogen-rich atmosphere. Many models also assume an adiabatic interior (see, for example, Scheibe et al. 2019). Thermal evolution models, however, suggest that the classical assumption of an adiabatic interior is inconsistent with the luminosities of Uranus and Neptune, and for this reason, models are being explored that are not fully adiabatic, but instead have a thermal boundary layer (see, for example, Scheibe et al. 2021; Stixrude et al. 2021). The gravitational harmonics determined by the Voyager flybys and observations of the dynamics of rings and moons as well as theoretical considerations based on laboratory experiments work together to constrain the properties of the planets' layers. Some fundamental aspects of ice giant interiors, such as the ice-to-rock mass fraction, are poorly constrained (Helled et al., 2020; Podolak et al., 2019). Even the rotation rates measured by Voyager for Uranus (Desch et al., 1986; Warwick et al., 1986) and Neptune (Warwick et al., 1989) have been called into question (Helled et al., 2010). Given these uncertainties, it is worth considering a relatively broad range of models.

Figure 4.1 shows profiles of density and Brunt-Väisälä frequency of Uranus and Neptune interior models that we use in this work. What we have labeled the adiabatic model is from Scheibe et al. (2019). Adiabatic oscillation calculations in `GYRE` require the thermodynamic derivatives Γ_1 (Eq. 4.2) and

$$\nabla_{ad} = \frac{1}{\Gamma_1}\left(\frac{\partial \ln T}{\partial \ln \rho}\right)_{ad}, \tag{4.4}$$

which we calculate numerically from the adiabatic model's $\rho(P)$ and $T(P)$. Because this model assumes a three-layer structure and features density discontinuities owing to sudden composition changes, double mesh points were inserted at the core-envelope and inner-outer envelope boundaries ($r/R \sim 0.07$ and $r/R \sim 0.75$, respectively, where R is the planetary radius) in order for `GYRE` to apply the appropriate jump conditions at those locations.

We considered a Saturn model from Mankovich and Fuller (2021) and confirmed that our mode calculation reproduced results consistent with theirs, up to the expected error associated with our first-order treatment of rotation (see below).

We have also constructed new models of Uranus and Neptune using the method described in Mankovich and Fuller (2021). In brief, these models are calculated using the fourth-order theory of figures (Nettelmann, 2017), assuming H-He-H_2O mixtures modeled using the MH13-SCvH equation of state for hydrogen and helium (Militzer and Hubbard, 2013; Saumon et al., 1995; Miguel et al., 2016) and Mazevet et al. (2019) for water, combined in an additive-volume approximation. The Mazevet et al. (2019) equation of state for water transitions to that of an ideal gas below $T = 800$ K, following Scheibe et al. (2019). Rather than the common practice of imposing discontinuous changes in composition, these models impose a gradient in the water abundance between a homogeneous H-He dominated outer envelope and a homogeneous H_2O-dominated interior. Denoting the H, He and H_2O mass fractions by X, Y, and Z so that $X + Y + Z = 1$, we fix $Y/(X + Y) = 0.275$ throughout the model following the protosolar value estimated by Asplund et al. (2009), and for $Z(r)$ assume a sigmoid function with four free parameters specifying the inner and outer radii of the gradient region and the Z values at those boundaries (see Mankovich and Fuller 2021 for details). One of these parameters is eliminated by the condition that the model satisfy each planet's equatorial radius.

Despite the stabilizing influence of the composition gradient, these models assume for simplicity that temperature is adiabatically stratified, subject to the boundary condition that $T = 150$ K at $P = 10$ bar, consistent with atmosphere models (Fortney et al., 2011).

We present mode calculations for three Uranus models, one fitting J_2 and J_4 exactly, and two that are offset in J_4 relative to the observed value by approximately ± 1 times the measurement uncertainty $\sigma_{J_4} = 1.30 \times 10^{-6}$ (Jacobson, 2014). The models achieve this by varying the width of the Z gradient region and are accordingly labeled "thin", "medium" and "thick", corresponding to J_4 offsets of -0.89, 0, and $+0.79$ times σ_{J_4}, respectively. Another Uranus model we label 'shallow' has a Z gradient region closer to the planet's surface. For Neptune we present a single model that fits J_2 and J_4. These models are summarized in Table 4.3 and their interior structures shown in Figure 4.1, where the stably stratified composition gradient regions are visible as regions with positive Brunt-Väisälä frequency. Although we are primarily focusing our discussion on f-modes, the models with stably stratified composition regions also generate g-modes, which in principle can mix with the f-modes, and can also be associated with their own resonances.

4.4.2 Normal mode frequency calculation

Because the ratios of rotation rate to breakup frequency of Uranus and Neptune,

$$\frac{\Omega}{\sqrt{\frac{GM}{R^3}}} = \begin{cases} 0.175 \pm 0.004, & \text{Uranus} \\ 0.155 \pm 0.006, & \text{Neptune} \end{cases} \tag{4.5}$$

(with uncertainties dominated by uncertainties in the bulk rotation rate; see Desch et al. 1986; Warwick et al. 1986, 1989; Helled et al. 2010) are significant, Coriolis accelerations are not negligible compared to the other terms in the momentum equation. For this reason, the oscillation frequencies given by `GYRE` are corrected to first order in the planet's rotation rate Ω (Ledoux, 1951; Unno et al., 1979). These corrections account for the Doppler shift and the approximate intrinsic perturbation to mode frequencies due to the Coriolis force.

`GYRE` evaluates an integral to provide the rotation splitting coefficient β that is involved in the Coriolis perturbation for solid-body rotation. β can also be calculated for a given mode with the equation (cf. Unno et al. 1979)

$$\beta = 1 - \frac{\int_0^R \left(2\xi_r\xi_h + \xi_h^2\right)\rho r^2 dr}{\int_0^R \left[\xi_r^2 + \ell\left(\ell+1\right)\xi_h^2\right]\rho r^2 dr} \tag{4.6}$$

where ξ_r and ξ_h are the radial and horizontal components of the displacement eigenfunction (Unno et al., 1979), which is given by

$$\begin{aligned} \xi\left(r,\theta,\phi,t\right) = & \left[\xi_r\left(r\right)\hat{r} + \xi_h\left(r\right)\left(\hat{\theta}\frac{\partial}{\partial\theta} + \hat{\phi}\frac{1}{\sin\theta}\frac{\partial}{\partial\phi}\right)\right] \\ & \times Y_\ell^m\left(\theta,\phi\right)e^{i\sigma_{\ell mn}t}, \end{aligned} \tag{4.7}$$

We did verify that the β values returned by `GYRE` are consistent with this formula.

Because Uranus and Neptune rotate more slowly than Jupiter and Saturn, we do not include second-order terms associated with oblateness and the centrifugal force, which together tend to decrease the frequencies (Vorontsov and Zharkov, 1981). For this reason, our uncertainties in calculated mode frequencies, and thus resonance locations, are one-sided.

We calculate the moment of inertia for each model, assuming spherical symmetry, by integrating

$$\frac{I}{MR^2} = \frac{8\pi}{3} \frac{\int \rho\left(r\right) r^4 dr}{MR^2} \tag{4.8}$$

Table 4.3 shows the parameters that were used for each model, as well as each model's calculated moment of inertia.

4.4.3 Sources of gravitational potential perturbations

Following Marley and Porco (1993), we can write the total gravitational potential as a sum of an unperturbed component and a perturbed component:

$$\Phi = \Phi_0 + \Phi'\left(t\right), \tag{4.9}$$

where full expressions for the unperturbed component Φ_0 and for the perturbed component $\Phi'\left(t\right)$ can be found in Marley and Porco (1993). The integrals for the perturbed gravitational harmonics are taken over the Eulerian density perturbation

$$\rho'_{\ell mn} = \rho'_{\ell n}\left(r\right) Y_\ell^m\left(\theta, \phi\right) e^{-i\sigma_{\ell mn} t} \tag{4.10}$$

instead of over the unperturbed density ρ. In the above equation, $\sigma_{\ell mn}$ is the oscillation frequency in the reference frame that rotates with the planet, r is the radius, θ is the colatitude, and ϕ is the azimuthal angle. The surface spherical harmonics Y_ℓ^m are defined in terms of the associated Legendre polynomials P_ℓ^m. The displacement eigenfunction is given by

$$\begin{aligned} \xi\left(r, \theta, \phi, t\right) = & \left[\xi_r\left(r\right)\hat{r} + \xi_h\left(r\right)\left(\hat{\theta}\frac{\partial}{\partial\theta} + \hat{\phi}\frac{1}{\sin\theta}\frac{\partial}{\partial\phi}\right)\right] \\ & \times Y_\ell^m\left(\theta, \phi\right) e^{i\sigma_{\ell mn} t}, \end{aligned} \tag{4.11}$$

where ξ_r and ξ_h are the radial and horizontal components of the displacement eigenfunction (Unno et al., 1979). The equations for the gravitational harmonics that appear in the equations for $\Phi'\left(t\right)$ can be reduced to

$$MR^{\ell}J'_{\ell n} = -\left(\frac{4\pi}{2\ell+1}\right)^{1/2} e^{i\sigma_{\ell 0 n}t} \int_0^R \rho'_{\ell n}\left(r\right) r^{\ell+2} dr \tag{4.12}$$

for $m = 0$, and

$$\begin{aligned} MR^{\ell}C'_{\ell mn} = & \left(-1\right)^{\frac{m+|m|}{2}} \left[\frac{2\ell+1}{4\pi}\left(\frac{(\ell-|m|)!}{(\ell+|m|)!}\right)\right]^{1/2} \\ & \times e^{i\sigma_{\ell mn}t} \int_0^R \rho'_{\ell mn}\left(r\right) r^{\ell+2} dr \end{aligned} \tag{4.13}$$

for $m \neq 0$. $S'_{\ell mn}$ can be made to vanish by an appropriate choice of phase (Marley and Porco, 1993).

The radial displacement eigenfunctions of $\ell = 2, 6, 10$, and 14 from our medium model are plotted in the top panel of Figure 4.2, normalized to $\xi_r = 1$ at $r = R$. We also show the normalized Brunt-Väisälä frequency N as a dotted line to highlight its correlation with the warp in the radial displacement eigenfunctions. The middle panel of Figure 4.2 shows the Eulerian density perturbation of the same modes $\ell = 2, 6, 10$, and 14. The bottom panel of Figure 4.2 shows the integrand of Equations 4.12 and 4.13, $\rho' r^{\ell+2}$, for each of these modes. These plots illustrate how the modes of lower spherical harmonic degree ℓ can probe deeper into the planet, whereas the modes of higher spherical harmonic degree ℓ are more sensitive to the outer layers and to the parts of the planet that are stably stratified.

Only the spherical harmonic Y_{ℓ}^{0} contributes to the $J'_{\ell n}$ term due to the orthogonality of the spherical harmonics. Likewise, for $m \neq 0$, the contribution to each $C'_{\ell mn}$ term is only from the Y_{ℓ}^{m} harmonic. Each oscillation mode thus contributes to a single perturbed gravitational harmonic. The planet's rotation, however, can mix modes slightly. For Saturn, no more than 15% of the rotationally corrected radial displacement eigenfunction could be attributed to mode mixing (Marley and Porco, 1993); for Uranus and Neptune, which rotate more slowly than Saturn, we can expect mode mixing to influence the radial displacement eigenfunction to an even lesser extent.

4.4.4 Resonance calculation

We calculate the pattern frequency Ω_{pat} of each normal mode seen from inertial space,

model	R (km)	M ($\times 10^{25}$ kg)	Ω ($\times 10^{-4}$ s^{-1})	J_2 ($\times 10^{-4}$)	J_4 ($\times 10^{-4}$)	I/MR^2
Uranus shallow	25,559	8.68009	1.0527	35.1068	-0.341705	0.2279
Uranus thin	25,559	8.68009	1.0527	35.1068	-0.330171	0.2204
Uranus medium	25,559	8.68009	1.0527	35.1068	-0.341705	0.2202
Uranus thick	25,559	8.68009	1.0527	35.1069	-0.351949	0.2200
Uranus adiabatic†	25,559	8.68009	1.0124	35.107	-0.342	0.2266
Neptune	24,764	10.24092	0.9996	34.0843	-0.334	0.2509

Table 4.3: Parameters of the planetary models. Equatorial radii R are from Archinal et al. (2018). M, J_2, and J_4 of Uranus are from Jacobson (2014), while M, J_2, and J_4 of Neptune are from Jacobson (2009). The classical Uranus spin rate Ω is from Voyager 2 radio data (Desch et al., 1986; Warwick et al., 1986) and is used only in the adiabatic model, while alternate spin rates Ω based on the shapes and gravitational coefficients of the planets are from Helled et al. (2010) and are used in the other models. The classical Neptune spin rate Ω, not used in any of our models, is 1.0834×10^{-4} s^{-1} (Warwick et al., 1989). The moments of inertia are calculated using Equation 4.8.
† Scheibe et al. (2019)

$$\Omega_{\text{pat}} = \frac{1}{m}\left(\sigma^0_{\ell n} + m\beta\Omega\right), \tag{4.14}$$

where $\sigma^0_{\ell n}$ is the oscillation frequency in the non-rotating limit for the mode specified by ℓ and n and β is the rotation splitting coefficient defined in Equation 4.6. Our models for Uranus assume the rotation rate provided in Helled et al. (2010), called the fast rotation rate, corresponding to a period of 16.58 hours. The adiabatic model assumes the classical, or slow, rotation rate, corresponding to a period of 17.24 hours (Desch et al., 1986; Warwick et al., 1986). Our Neptune model likewise uses the rotation rate from Helled et al. (2010), corresponding to a period of 17.46 hours, which in contrast is slower than the classical rotation rate provided by Voyager 2 radio data, corresponding to a period of 16.11 hours (Warwick et al., 1989). In general, resonance locations of a faster rotator fall further inward than those of a slower rotator. Thus the rotation rate of these planets is another parameter that ring seismology could help constrain, similar to how Mankovich et al. (2019) calculated a seismological rotation rate for Saturn.

Then we calculate the resonance location numerically. Lindblad resonances occur at locations where the following relationship is satisfied (Goldreich and Tremaine, 1979):

$$m\left(n - \Omega_{\text{pat}}\right) = \pm q\kappa, \tag{4.15}$$

where the upper sign corresponds to an inner Lindblad resonance and the lower sign corresponds to an outer Lindblad resonance, q is a positive integer, and n and κ are the resonance location's mean motion and horizontal epicyclic frequency, respectively. These are calculated according to the second-order equations from Renner and Sicardy (2006).

Similarly, vertical resonances occur at locations where

$$m\left(n-\Omega_{\text{pat}}\right)=\pm b\mu, \tag{4.16}$$

where the upper sign corresponds to an inner vertical resonance and the lower sign corresponds to an outer vertical resonance, b is a positive integer, and μ is the resonance location's vertical epicyclic frequency, which is found using the equation from Shu et al. (1983):

$$\mu^2+\kappa^2=2n^2 \tag{4.17}$$

We are focusing only on first-order resonances, which have $q=b=1$, though higher-order resonances are possible (Marley, 2014).

Corotation resonances are potentially interesting to consider in the context of Neptune's Adams ring (see Section 4.6.4). Hence we compute corotation resonance locations for Neptune following the same procedures as in A'Hearn et al. (2021). That is, we find the radii where the mean motion n matches the pattern frequencies Ω_{pat} associated with the $\ell=m$ modes we have calculated from our Neptune model.

4.5 Results

Figures 4.3 and 4.4 show the calculated resonance locations with f-mode oscillations for all our Uranus models. Figure 4.3 shows the Lindblad resonances, while Figure 4.4 shows the vertical resonances. We show the resonance locations up to $\ell=25$. For every mode, the resonance location of the medium model falls in between those of the thin and thick models. The resonance location of the thick model typically falls further outward (and the resonance location of the thin model falls further inward), the $\ell=m=2$ mode being the sole exception. This general trend is set by the models' different predictions for density in the outer envelope, which the higher m modes are more sensitive to (cf. Figure 4.2).

The region of particular interest that we find spans from the 6 ring to the β ring. Satellite resonances do not line up with these inner rings (Hedman and Chancia, 2021), but several high-m mode resonances from our models do fall in this region. The predictions from our models as well as from Marley et al. (1988) include resonance locations that fall in the ζ ring for the modes with $\ell \leq 5$. The ζ ring, however, has low optical depth, and would not be expected to sustain a wave.

Lindblad resonances that fall among the inner rings are listed in Table 4.4, whereas vertical resonances are listed in Table 4.5. The resonance locations are given in general ranges, based on all our models as well as the frequency uncertainty from our calculations with first-order rotation corrections. Predictions based on individual interior models are found in the Appendices. We group the 6, 5, and 4 rings together, and the α and β rings together, in these tables, because the uncertainty associated with a mode's frequency or resonance location is comparable to the distance between these narrow rings. Differential rotation confined to the outer layers of the interior will have a greater effect on the higher-degree modes.

Among the 6, 5, and 4 rings, we expect that a Lindblad resonance with $m = 2$ or $7 \leq m \leq 13$, or a vertical resonance with $9 \leq m \leq 14$, could be from a planetary normal mode. Among the α and β rings, we expect that a Lindblad resonance with $11 \leq m \leq 18$, or a vertical resonance with $13 \leq m \leq 19$, could be from a planetary normal mode.

Although planetary normal mode resonances with $m > 15$ may fall among the η, γ, δ, λ, and ϵ rings, we expect the dynamics of these rings to be influenced more by the moons Cordelia and Ophelia. The case has been made that while Cordelia is the outer shepherd of the δ ring and the inner shepherd of the ϵ ring, Ophelia is the outer shepherd of both the ϵ and γ rings (Porco and Goldreich, 1987). Recently, the η ring was found to be influenced by Cressida (Chancia et al., 2017). Nevertheless, at Saturn the $\ell = m = 10$ mode was found to be anomalously strong (Hedman et al., 2019), and with this precedent the influence of planetary normal modes on the outer rings cannot be ruled out.

At Neptune, modes with $\ell = m = 16, ..., 21$ fall among the moons Naiad and Thalassa. Naiad and Thalassa are themselves in a 73:69 resonance (Brozović et al., 2020), made

ℓ	m	Ω_{pat} (deg/day)	r_{res} (km)
6, 5, or 4 ring			41,838; 42,235; 42,572
2	2	1995.2-2360.4	38571-43142
7	7	1585.4-1753.2	39244-41963
8	8	1517.2-1666.7	40166-42760
9	9	1460.4-1591.0	41088-43498
10	10	1412.3-1525.1	41981-44184
12	10	1506.0-1605.7	40565-42334
13	11	1450.1-1537.1	41532-43175
14	12	1402.8-1479.3	42409-43935
16	12	1466.5-1537.2	41338-42655
17	13	1419.4-1482.8	42176-43420
α or β ring			44,719; 45,661
11	11	1370.9-1467.8	42827-44822
12	12	1334.6-1418.1	43618-45417
13	13	1301.1-1375.0	44350-46012
14	14	1271.6-1337.3	45024-46562
15	15	1245.4-1304.3	45644-47070
16	14	1326.8-1387.5	43933-45262
17	15	1295.6-1350.5	44598-45850
18	16	1267.7-1318.0	45211-46397
19	15	1342.5-1395.1	43644-44776
20	16	1310.5-1359.2	44294-45382
21	17	1281.9-1327.2	44897-45949
22	18	1256.1-1298.6	45460-46480

Table 4.4: Predicted Lindblad resonance locations among the inner rings of Uranus. The ranges in frequencies and locations take into account the two most extreme models and include the error in the range given.

ℓ	m	Ω_{pat} (deg/day)	r_{res} (km)
6, 5, or 4 ring			41,838; 42,235; 42,572
10	9	1517.1-1642.0	40245-42420
11	10	1460.6-1566.9	41241-43216
12	11	1412.5-1503.4	42159-43945
14	11	1486.3-1569.6	40966-42481
15	12	1435.2-1508.5	41868-43281
17	12	1496.8-1565.4	40850-42086
18	13	1446.7-1508.4	41704-42882
19	14	1403.1-1459.4	42486-43614
α or β ring			44,719; 45,661
14	13	1332.1-1402.8	43769-45302
15	14	1299.6-1362.7	44471-45896
16	15	1270.9-1327.7	45115-46446
18	15	1319.4-1373.0	44117-45303
19	16	1289.4-1338.8	44748-45881
20	17	1262.6-1308.4	45333-46422
21	16	1331.0-1379.2	43872-44922
22	17	1300.7-1345.8	44491-45511
23	18	1273.4-1315.8	45069-46063
24	19	1248.7-1288.8	45612-46582

Table 4.5: Predicted vertical resonance locations near the inner rings of Uranus.

possible by Naiad's high inclination (4.7°). Should it be found that this resonance does not fully account for their orbits, perturbations from planetary normal modes may be part of the solution. Furthermore, it is not known how Naiad reached its high inclination. The most likely explanation is passage through a previous resonance with Despina (Banfield and Murray, 1992). Another possibility, however, is that Naiad's inclination was excited instead by a vertical resonance with a Neptunian normal mode.

The above calculations focused exclusively on the f-modes ($n = 0$). It is also interesting, however, to consider the $\ell = m$, $n = 1$ g-modes for the non-adiabatic models because these can also fall among the ring systems. In the Uranian system (Figure 4.6), $\ell = m$, $n = 1$ g-mode resonances are likely to fall in the mid- to outer-ring system as well as the innermost moons. The spread in resonance location predictions is greater for g-modes than for f-modes because the g-mode spectrum is sensitive mainly to the Brunt-Väisälä frequency $N(r)$. The thin-medium-thick triplet of models diverges more for higher ℓ, where the eigenfunctions have higher amplitudes in the g-mode cavity.

In the Neptunian system (Figure 4.7), $\ell = m$, $n = 1$ g-mode resonances are likely to fall among the inner moons and middle to outer rings. There is even a g-mode resonance that falls near the Adams ring, which we discuss in Section 4.6.4. G-modes at higher order ($n \geq 2$) are at lower frequency, and so their outer Lindblad resonance locations would fall farther out. Nevertheless, their gravity perturbations might be too small to matter because they are more effectively confined deep down than the $n = 1$ g-modes.

Note that the mean absolute model uncertainty, due to the approximate treatment of rotation, in the resonance locations for all the f-modes we calculated is $\delta r = 610$ km for the Uranus models and $\delta r = 450$ km for the Neptune model. The maximum uncertainty in f-mode resonance locations is $\delta r = 805$ km for the Uranus models and $\delta r = 557$ km for the Neptune model. These both correspond to the $\ell = m = 2$ f-mode. The uncertainty generally decreases with increasing m.

To decrease the uncertainty, frequency-correction calculations may be carried out to second-order using the perturbation theory techniques described in Vorontsov and Zharkov (1981) and summarized in the Appendix of Marley (1990). We leave the second-order calculations for possible future work. Further knowledge of the planets' interior structure, thermodynamic state, and rotational state can also improve the precision of resonance location predictions.

4.6 Discussion

We have found that planetary normal modes likely fall among the rings of Uranus and Neptune. The next question is whether normal mode resonances would be detectable in the Uranian and Neptunian rings. Potential signatures of such resonances could include wave-like structures in the dense Uranian rings, cross-correlations with Uranus's many narrow ring features, and longitudinal structures in more dusty rings. Each of these methods is discussed in more detail below.

Note that we do not attempt to compute the explicit amplitudes of the gravitational perturbations associated with these perturbations. While Marley and Porco (1993) estimated the strengths of the perturbations needed to produce the observed waves in Saturn's rings, more recent kronoseismology studies did not find strong correlations between the anticipated and the observed amplitudes of normal mode resonances (Hedman et al., 2019). Although it is expected that torques decrease as the oscillation degree ℓ increases because a smaller quantity of mass participates in the oscillation (Marley and Porco, 1993), the intrinsic amplitude spectrum of normal modes in the planet is unknown but the subject of much current research (Marley and Porco, 1993; Markham and Stevenson, 2018; Wu and Lithwick, 2019; Markham et al., 2020). For example, Markham and Stevenson (2018) examined mode excitation mechanisms in giant planet interiors. They found that moist convective storms associated with water condensation were not energetically feasible for Jupiter, but it remains to be seen whether that mechanism could excite Uranian or Neptunian modes to observable levels. Given all these theoretical uncertainties, we leave the computation of amplitudes for future work.

4.6.1 Occultations of narrow dense rings

One way to identify resonant perturbations would be the detection of density waves similar to those seen in Saturn's rings. This would best work in Uranus's narrow dense rings, where the search can be guided by **predictions for the locations of resonances with a given m, which corresponds to the number of spiral arms.** Note that the resolution achievable with an occultation is limited by the Fresnel scale: $\lambda_F \sim \sqrt{\lambda D}$. At $\lambda = 0.2\mu$m, the great distances D of Uranus (19.2 AU) and Neptune (30 AU) from Earth prevent ground-based or Earth-orbit-based stellar occultations from obtaining better resolution than about 750 m and 950 m, respectively. Given that wave-like variations in the dense rings have sub-kilometer wavelengths (Chancia and Hedman, 2016; Horn et al., 1988), we expect resolutions of order 200 m is needed to see any planet-generated waves. This resolution threshold, combined with the number of cuts required to uniquely determine the number of arms, which is of order the relevant m (about 20 for the waves of interest here), implies that the detection of planetary normal modes via wave identification will have to await an orbiter of Uranus or Neptune. An orbiter can observe occultations in ultraviolet, visible, near-infrared, and radio parts of the spectrum at a much closer distance, and it would be expected to produce radial profiles of the rings at a range of longitudes with sufficient resolution to determine the number of spiral arms in a wave. Observation of the ring plane from different incidence angles will also allow bending waves to be easily discerned from density waves.

While the overall shapes of the Uranian rings are dominated by factors that can be attributed to free modes in the rings themselves, this does not exclude the possibility that these rings can also preserve signals from planetary normal modes. The Uranian α and β rings are considered analogs of the Saturnian Maxwell and Colombo ringlets (Porco, 1990; Chiang and Culter, 2003). These rings are considered in Chiang and Culter (2003), who present a proof, relying on first steps taken by Borderies et al. (1983), that circular, nodally locked rings are linearly stable to perturbations to their inclinations and nodes. The Colombo ringlet, also named the Titan ringlet because it is in a 1:0 apsidal resonance with Saturn's moon Titan (Porco et al., 1984; Nicholson et al., 2014), is located near several planetary normal modes: $6 \leq \ell \leq 15$, $5 \leq m \leq 11$ (Mankovich et al., 2019). The Maxwell ringlet inside the Maxwell Gap in Saturn's C ring is perturbed by an $\ell = m = 2$ mode (French et al., 2016; Cuzzi et al., 2018), as predicted by Fuller (2014). For this reason, we are also hopeful that either the α or β rings, or both, are likewise perturbed by planetary normal modes. The Uranian ϵ ring is also considered to have similar properties to the Maxwell ringlet (French et al., 1991, 2016): sharp edges, a freely precessing elliptical shape, and a linear width-radius relation. The mean optical depth of the Maxwell ringlet is $\bar{\tau} = 0.968$ (French et al., 2016).

Horn et al. (1988) identified an inward-propagating density wave in the δ ring, which they interpreted to be evidence of a moonlet interior to the δ ring. Because no moonlet has yet been discovered interior to the δ ring, we consider that such a density wave could be a candidate planetary normal mode resonance. Horn et al. (1988) constrained the azimuthal wavenumber m of the resonance that generated this wave to be $48 \leq m \leq 112$, based on three conditions: that the torque exceed a critical value (Goldreich and Porco, 1987) for nonlinearity and the moonlet still remain undetected in the Voyager Imaging search (Smith et al., 1986), that the moonlet lie between the γ and δ rings, and that the separation in radius between first-order resonances be greater than half the width of the δ ring (Horn et al., 1988). The range of possible m values was thus not constrained by an m-lobed pattern detected in the ring itself. If instead the inward-propagating density wave in the δ ring is driven by a planetary normal mode resonance, none of the conditions given by Horn et al. (1988) would apply, though their measurement of the product of the wavelength and the distance from the resonance $\lambda d = 0.84 \pm 0.07$ km (Horn et al., 1988) makes it difficult for m to be less than 10. From our resonance location predictions, we can instead expect $17 \leq m \leq 23$, should the density wave in the δ ring be from an f-mode resonance. In addition to density waves, Lindblad resonances with satellites can perturb ring edges, generating non-circular shapes like those observed for the outer edge of Saturn's A and B rings (Goldreich and Tremaine, 1978; Nicholson et al., 2014; El Moutamid et al., 2016; Tajeddine et al., 2017) and for Uranus's ϵ ring (French et al., 1991) and η ring (Chancia et al., 2017).

4.6.2 Correlating Uranian ring features and resonance locations

Another potential way to identify these resonances would be to correlate the locations of multiple narrow ring features with expected resonant locations. For example, Figure 4.8 shows the brightness of the inner rings of Uranus as a function of radius, from a high-phase image (C2685219; see Hedman and Chancia 2021) that showed many more narrow ring features than the named rings. These features could potentially reflect additional locations where material is confined by resonances. Vertical dash-dotted lines show Lindblad resonance locations calculated from the medium model. Due to the uncertainty of our calculations, lining up ring features with resonances in this way is to be taken only as a demonstration of a way to correlate the models with ring features. Nevertheless, the way that the $\ell = m = 8, 9, 10, 11, 12$ modes line up with either peaks or troughs in the ring brightness is suggestive of a role they may play in perturbing ring material radially.

4.6.3 Longitudinal variations in diffuse rings

The Uranian ζ ring and the Neptunian Galle ring have low optical depth. Although many mode resonances fall within them, these rings are so tenuous that we do not expect them to be capable of sustaining a wave. Longitudinal structure can be driven by resonances with the planet's magnetic field, as is the case at magnetic Lindblad resonances in Saturn's D

Ring (Hedman et al., 2009a; Chancia et al., 2019), and we encourage future work exploring potential resonances between the Uranian and Neptunian magnetic fields and their ring systems. Nonetheless, planetary normal modes, particularly the stronger $\ell = m = 2$ modes, should be kept in mind in studies of longitudinal structures in diffuse rings.

4.6.4 Neptune's Le Verrier and Adams rings

Finally, we can consider whether planetary normal mode resonances could influence the dynamics of Neptune's narrow dusty rings in a detectable way.

While normal mode resonances could potentially play a role in confining the Le Verrier ring (Brooks et al., 2020), testing this idea is challenging. For one, the ring appears homogeneous in the Voyager images (Ferrari and Brahic, 1994), which limits our ability to identify signatures of external perturbations. Furthermore, this ring is also close to other resonances, including Thalassa's 21:23 resonance (Gaslac Gallardo et al., 2020). In addition, the 2:1 resonance with Neptune's rotation frequency, whose value is known with less certainty, falls in the Le Verrier ring region. Simply applying Kepler's Third Law to find the 2:1 resonance location, neglecting Neptune's oblateness, yields

$$a_{\rm res} = \left(\frac{GM}{n^2}\right)^{1/3} = \begin{cases} 52,607\,\text{km}, & \text{fast} \\ 55,507\,\text{km}, & \text{slow} \end{cases} \tag{4.18}$$

where the mean motion $n = 2\Omega$, and "fast" and "slow" refer to estimates for Neptune's rotation rate given in Table 4.3. The Le Verrier ring is located at 53,200 km (de Pater et al., 2018), in the middle of the resonance locations according to the two different rotation rates (Warwick et al., 1989; Helled et al., 2010).

It is also worth noting that $n = 1$ g-mode resonances can occur near Neptune's Adams ring, because this could potentially mean that these resonances may be relevant to understanding the arcs in that ring. The ring arcs in the Adams ring comprise the most studied part of Neptune's rings (see for example Porco et al. 1995; de Pater et al. 2018). Ring arcs in the Saturnian system are confined longitudinally by orbital resonances with moons (Spitale et al., 2006; Hedman et al., 2007b; Hedman et al., 2009b, 2010; Cooper et al., 2008;

A'Hearn et al., 2019). Although several ideas have been proposed about the particular resonance of Neptune's ring arcs, consensus has not been reached. Initial studies suspected that a 42:43 resonance with Galatea confined the ring arcs (Goldreich et al., 1986; Porco, 1991; Namouni and Porco, 2002). Deviations from the exact rate of different types of a corotation resonance with Galatea, however, support other possible explanations (Renner et al., 2014). Confinement due to shepherding by undetected satellites that are co-orbital with the Adams ring arcs has been proposed (Lissauer, 1985; Salo and Hanninen, 1998; Renner et al., 2014), though more recent investigation claims to rule out that co-orbital satellites could be the source of the dust (Giuliatti Winter et al., 2020). Another recent idea is that the Adams ring arcs are in a three-body resonance with Galatea and Larissa (Showalter et al., 2017).

One potential way to test whether planetary normal modes could be confining material in the Adams ring is to take another look at the distribution and extent of the arcs. A consequence of the initial 42:43 corotation resonance theory of confinement was that each of the 42 corotation sites, also called "pockets", spans only $\sim 9^\circ$. This posed a problem for the Fraternité arc, whose longitudinal extent is greater, and so it was assumed that Fraternité occupies two corotation sites.

Should the ring arcs instead be the effect of a corotation resonance with an oscillation degree $m < 42$, the corotation site would span a greater longitudinal extent θ, because

$$\theta = \frac{360^\circ}{m}, \tag{4.19}$$

which for low enough m could encompass the entirety of Fraternité in one corotation site. Although Lindblad resonances do not confine material, each Lindblad resonance can be associated with a corotation resonance, which can confine material. The planetary corotation resonance from the $\ell = m = 19$, $n = 1$ g-mode is calculated to fall in the range $62,844$-$63,230$ km, which encompasses the Adams ring. The $m = 19$ corotation site would span approximately 19°, over twice as much as an $m = 42$ corotation site, and could thus encompass the entirety of the Fraternité arc. We hope to explore this possibility further in a future work.

4.6.5 Conclusion

While none of the structures in the rings around Uranus and Neptune has yet been firmly attributed to a planetary normal mode, the above considerations indicate that ring seismology of the ice giants could be done when the appropriate data becomes available. To the extent that different interior models affect normal mode resonance locations, the detection of planet-driven ring waves or perturbations to moon orbits would allow a variety of interior models to be ruled out. These may provide evidence for or against a stably stratified layer or a diffuse core. Stable stratification, which occurs in all our interior models except the adiabatic model, allows the presence of g-modes, which could possibly be detected if they fall in or near rings (Fuller, 2014; Friedson, 2020). Should Uranus or Neptune additionally have a diffuse core, for example, the f-mode and g-mode resonances would be modified compared to our results here, particularly those corresponding to the $\ell = 2$ modes most sensitive to $\rho(r)$ and $N(r)$ in the deep interior.

To evaluate these predictions, attempts can be made with Voyager and ground-based observations. Nevertheless, we expect results from such observations to be inconclusive, and an orbiter with a primary mission duration of at least a year or two to measure pattern speeds to within around $0.1°$/day would likely be required to make the observations necessary to determine effects from planetary normal mode resonances in the rings of Uranus and Neptune.

4.7 Acknowledgements

We are grateful to many individuals for useful comments and discussions, including P. Nicholson, M. Tiscareno, M. Ćuk, L. Fletcher, M. Brozović, and K. Volk. We thank NASA for the support through the Solar System Workings grants NNX15AH45G and 80NSSC21K1865.

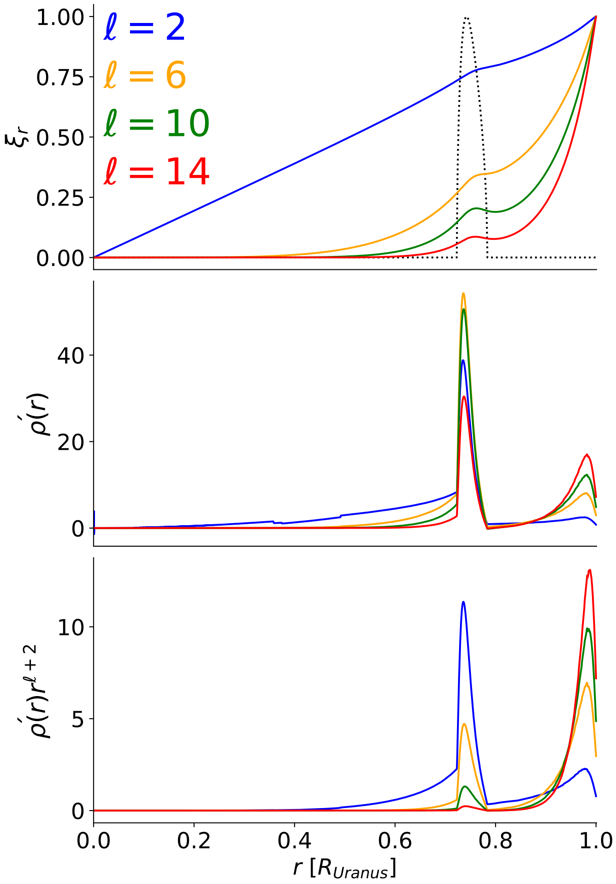

Figure 4.2: (Top) Radial displacement eigenfunctions for $\ell = 2, 6, 10$, and 14, normalized to $\xi_r = 1$ at $r = R$, from the medium Uranus model. The Brunt-Väisälä frequency N, normalized to peak at 1, is shown with dotted lines. (Middle) Eulerian density perturbation $\rho'(r)$ for the same four modes. (Bottom) Integrand of Equations 4.12 and 4.13, $\rho' r^{\ell+2}$, relevant for gravitational potential perturbations, for the same modes. The modes of lower oscillation degree ℓ are more sensitive to inner layers of the planet, while the modes of higher oscillation degree ℓ are more sensitive to outer layers of the planet.

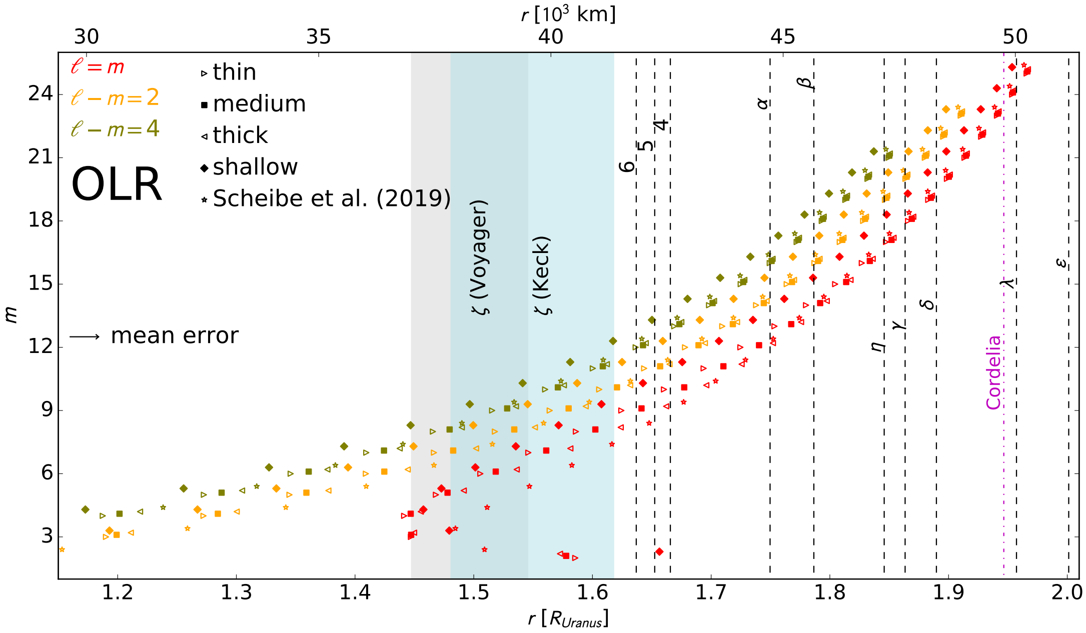

Figure 4.3: Normal mode outer Lindblad resonance (OLR) location predictions from all five Uranus models. The azimuthal order m (equivalent to the number of spiral arms) is the vertical axis, and distance from the center of Uranus is the horizontal axis, shown in Uranus radii on the bottom and in km on the top. OLRs can excite inward-propagating spiral density waves. The typical uncertainty of these resonance locations is shown by one bar on the left.

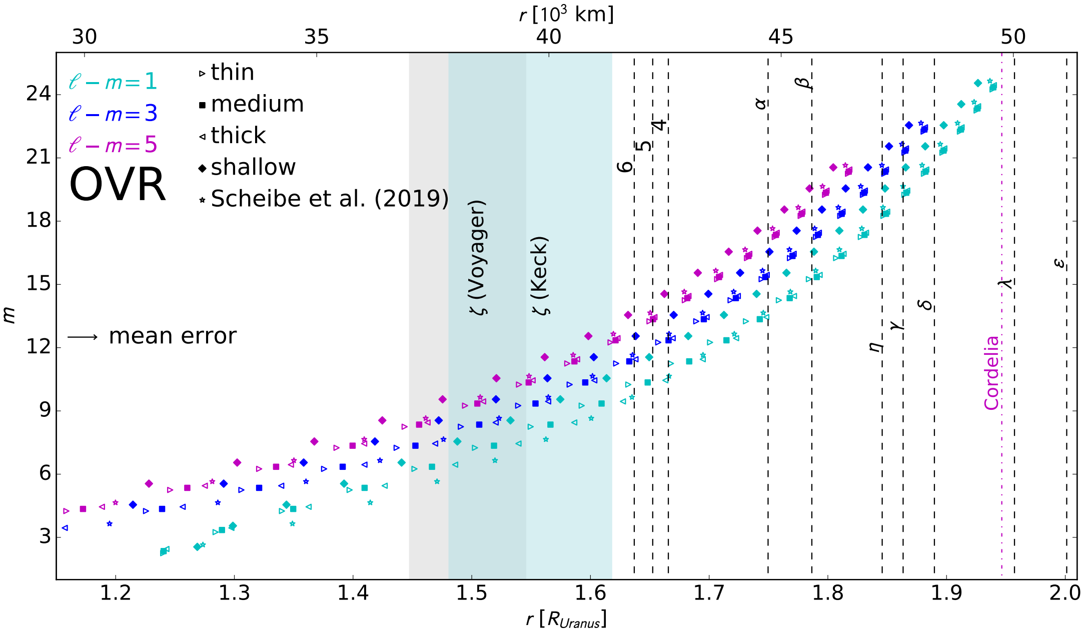

Figure 4.4: Normal mode outer vertical resonance (OVR) location predictions from all five Uranus models. The azimuthal order m (equivalent to the number of spiral arms) is the vertical axis, and distance from the center of Uranus is the horizontal axis, shown in Uranus radii on the bottom and in km on the top. OVRs can excite outward-propagating bending waves. The typical uncertainty of these resonance locations is shown by one bar on the left.

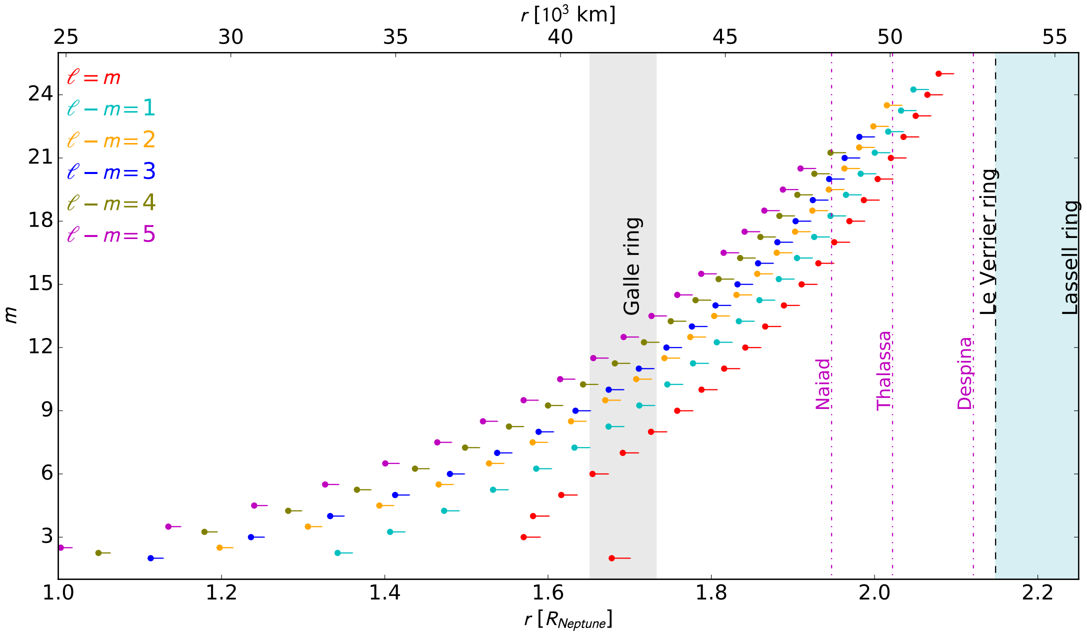

Figure 4.5: Normal mode resonance location predictions for Neptune. The azimuthal order m is the vertical axis, and distance from the center of Neptune is the horizontal axis, shown in Neptune radii on the bottom and in km on the top. Both outer Lindblad resonances (OLR) and outer vertical resonances (OVR) are shown. Several resonances fall in the Galle ring, and others may perturb the inner moons Naiad and Thalassa.

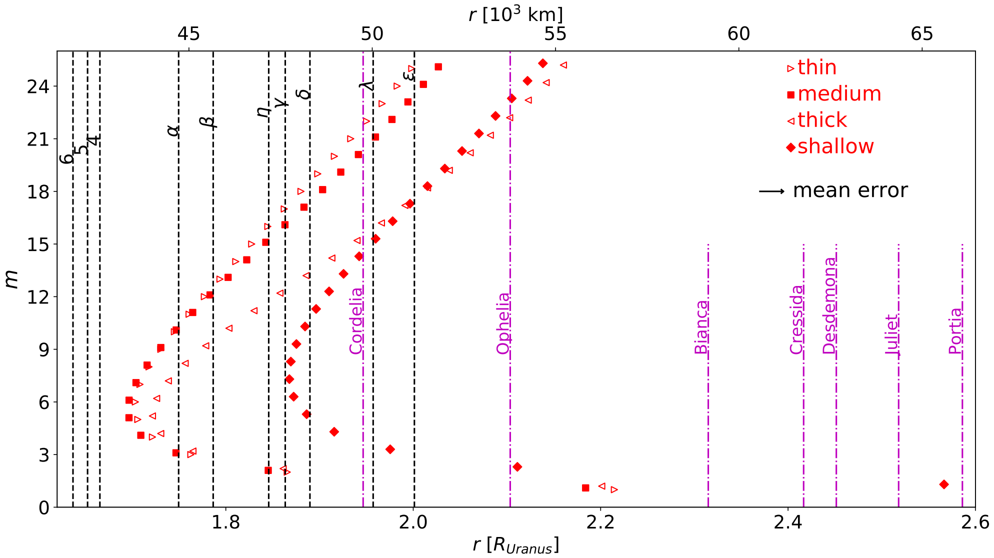

Figure 4.6: Resonance location predictions for Uranian g-modes. The azimuthal order m is the vertical axis, and distance from the center of Uranus is the horizontal axis, shown in Uranus radii on the bottom and in km on the top. Only outer Lindblad resonances (OLR) with $\ell = m$, $n = 1$ are shown.

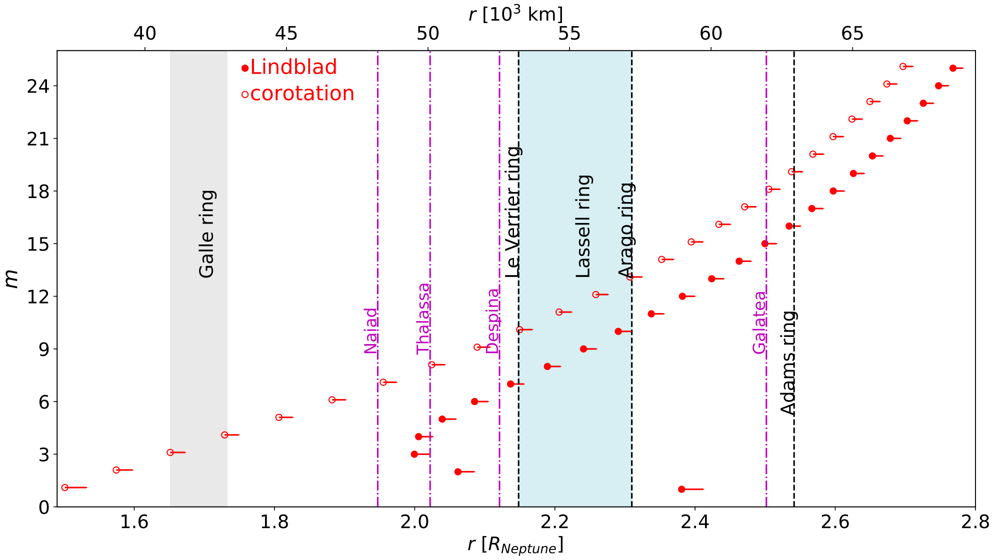

Figure 4.7: Resonance location predictions for Neptunian g-modes. The azimuthal order m is the vertical axis, and distance from the center of Neptune is the horizontal axis, shown in Neptune radii on the bottom and in km on the top. Outer Lindblad resonances (OLR) with $\ell = m$, $n = 1$ are shown as filled-in circles, while corotation resonances associated with these Lindblad resonances are shown with open circles.

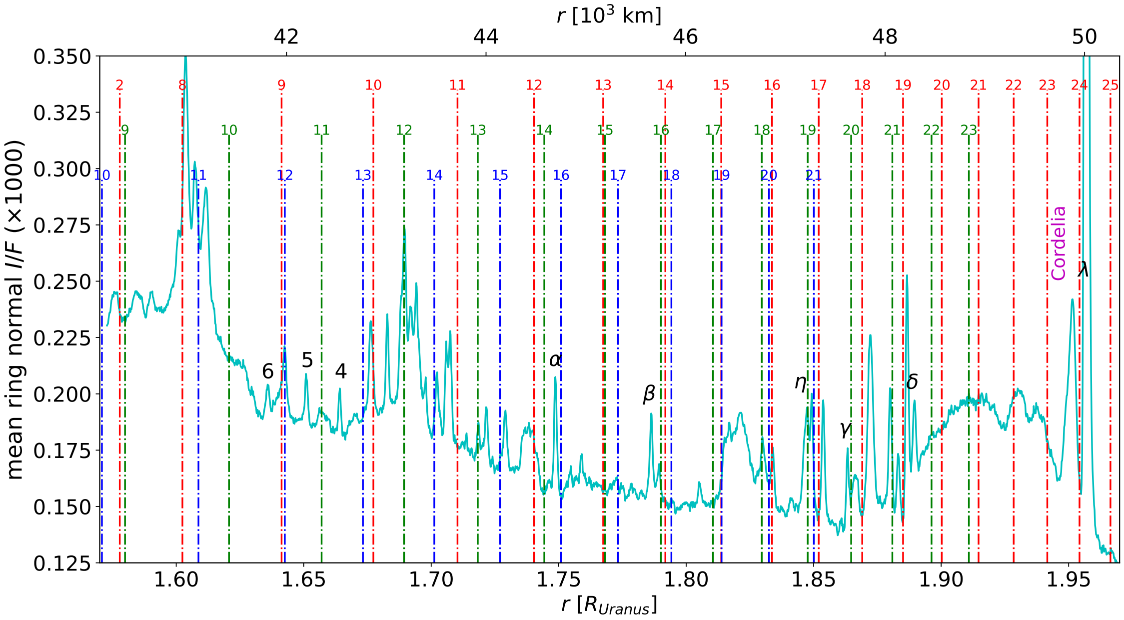

Figure 4.8: Radial scan of Uranian rings compared to Lindblad resonance predictions from the medium model. The cyan curve shows the mean ring normal I/F as a function of radius. While the named narrow rings are labeled, many other narrow features can be seen in this scan. The tallest dash-dotted lines, in red, show the locations of the $\ell = m$ mode resonances; the intermediate-sized dash-dotted lines, in green, show the locations of the $\ell - m = 2$ mode resonances, and the shortest dash-dotted lines, in blue, show the locations of the $\ell - m = 4$ mode resonances. The integer above each dash-dotted line corresponds to the azimuthal order m of the mode.

CHAPTER 5

Avenues for future work

In this thesis, I have shown how interactions among small bodies inside of resonances impact their orbital evolution, with special relevance to the Saturnian system. I have also calculated where to look in the Uranian and Neptunian rings for evidence of planetary normal mode resonances. Below are a number of possible avenues for future work related to these topics. In addition, I also present in Section 5.2.2 an excerpt about tidal evolution in the Saturnian system that I contributed to a multi-authored paper about Saturn's small moon Pallene, Muñoz-Gutiérrez et al. (2021).

5.1 Dynamics of Neptune's ring arcs

Neptune's ring arcs were introduced in Chapter 1. In Chapter 2, it was mentioned that the basic finding about energy conservation in corotation resonances has important implications for the stability of ring arcs in general, including dense arcs like those found in Neptune's Adams ring (A'Hearn et al., 2019). Due to the high density of particles, inter-particle collisions are expected to be common, and inelastic interactions such as accretion can occur. Numerical simulations of Neptune's ring arcs are likely needed to distinguish whether such interactions would tend to eject material out of the stable corotation sites.

To carry out these simulations properly, however, the specific mechanism that confines them ought to be known. Although several ideas have been proposed about the particular resonance of Neptune's ring arcs, we do not have certainty about which one is responsible. It was first suggested that they could be shepherded at a Lagrange point by an undiscovered moon (Lissauer, 1985). Goldreich et al. (1986) then proposed a corotation resonance as their explanation, even before the discovery of Galatea. Galatea was then found in the Voyager 2 images (Smith et al., 1989) of the same order of magnitude predicted by Goldreich et al. (1986). The Adams ring has several ring arcs that move at rates close to a 42:43 corotation resonance with Galatea. At first, it was suspected that the Adams ring arcs were in a corotation inclination resonance (Porco, 1991) Later, evidence was put forward that it is rather a corotation eccentricity resonance that explains the ring arcs' confinement (Namouni and Porco, 2002). Deviations in the observed motion of the arcs from the predicted rate of either type of corotation resonance, however, support other possible explanations (Renner et al., 2014). The presence of undetected satellites that are co-orbital with the Adams ring arcs has been proposed (Salo and Hanninen, 1998; Renner et al., 2014), though more recent investigation claims to rule out that co-orbital satellites could be the source of the dust (Giuliatti Winter et al., 2020). Another recent idea is that the Adams ring arcs are in a three-body resonance with Galatea and Larissa (Showalter et al., 2017). Nevertheless, none of these theories explain how two of the ring arcs could have faded since 1989, while the other two have survived (de Pater et al., 2018).

One way this can be done is with an impulse from an interplanetary rock. Similar to a derivation I have previously laid out (A'Hearn et al., 2021), for nearly circular orbits, the standard orbital perturbation equations can describe the rate of change of semi-major axis over time as (Burns, 1976; Hedman, 2018)

$$\frac{\delta a}{\delta t} = 2na\frac{F_p}{F_G} \tag{5.1}$$

where the mean motion $n = \sqrt{GM/a^3} \simeq 819.8^\circ/\text{day}$, F_p is the azimuthal component of the perturbing force, $F_G = GMm/a^2 = n^2am$ is the gravitational force on the ring arc from Neptune's center, M is Neptune's mass, and m is the mass of the ring arc, which we can rewrite in terms of surface mass density and area $m = \sigma A$. The ring arc particles will thus undergo a semi-major axis change δa upon receiving an azimuthal impulse

$$F_p\delta t = \frac{F_G}{2na}\delta a = \frac{1}{2}n\sigma A\delta a. \tag{5.2}$$

Because the width of the ring arc is approximately 15 km (de Pater et al., 2018), the δa required to disrupt the ring arc must be greater than half its width. For a collision between a ring arc and an interplanetary rock, we can estimate the impact speed as comparable to the ring arc's orbit speed $v = na \simeq 10.4$ km/s. We can then divide the impulse by this orbit speed to get a lower bound mass estimate for the interplanetary rock. An upper bound mass estimate can also be found because we require the other ring arcs not to be disrupted. This could then be tested with numerical simulations.

Another possibility that could explain the disappearance of the rings arcs is that the dust has re-coagulated onto the source bodies that had previously provided the ring arcs with dust. If neither of the above scenarios are deemed plausible, perhaps the fading of the arcs could be explained simply by dissipation through solar radiation pressure and Poynting-Robertson drag (Foryta and Sicardy, 1996; Giuliatti Winter et al., 2020).

5.2 Orbital migration

5.2.1 Tidal evolution

Tides are a result of objects not being point-masses but bodies with three spatial dimensions (Murray and Dermott, 1999). Torques produced by tides eventually drive changes in the orbits especially of moons. Retrograde moons such as Neptune's Triton as well as prograde moons that orbit faster than their host planet spins are doomed to migrate inward until they cross the Roche limit and are eventually torn apart. Prograde moons that orbit more slowly than their host planet spins are migrating away from it. Such is the case of our Moon and of most major moons in the Solar system. The rate at which moons migrate, however, is difficult to know with much certainty.

Recent tidal evolution studies have called into question the assumption that many of the moons of our Solar system are primordial (Lainey, 2016; Ćuk et al., 2016). Instead, a cyclic process between moons and rings may be at play, in which an inward migrating moon is disrupted by tidal forces. While a portion of the disrupted moon falls into the planet, another portion forms a ring system, and eventually the outer part of the ring system accretes into new moons, which will migrate inward and continue this process as long as they are inside the corotation radius (Hesselbrock and Minton, 2017, 2019). Not only can determination of tidal evolution rates help us constrain the history of satellite systems, but it can also tell us about the interiors of these planets (Lainey, 2016).

We have learned lessons about tidal evolution from the Jovian and Saturnian systems (Park et al., 2019). The volcanic activity of Jupiter's moon Io is tied to the evolution of its eccentricity and semi-major axis (de Kleer et al., 2019), and gravitational effects on Io have led to detection of dynamical tides in Jupiter, which are expected to elucidate the existence of a dilute core in Jupiter (Idini and Stevenson, 2021). Jupiter's moon Europa and Saturn's moon Enceladus are both icy satellites with subsurface oceans that are tidally heated, and these tidal interactions influence their thermal, rotational, and orbital evolution (Matsuyama et al., 2018; Rovira-Navarro et al., 2019).

5.2.2 Mimas, Enceladus, and Pallene

Reproduced below in this Subsection is an excerpt from a published journal article of which I am a co-author:

M.A. Muñoz-Gutiérrez, A.P. Granados Contreras, G. Madeira, G., J.A. A'Hearn, S. Giuliatti Winter, "Long-term Dynamical Evolution of Pallene (Saturn XXXIII) and Its Diffuse, Dusty Ring" *Monthly Notices of the Royal Astronomical Society*, stab3627, 2021

The paper sought to carry out a comprehensive study of the long-term dynamics of Pallene, as well as of the possible origin and dynamical evolution of its diffuse dusty ring, formed by micrometer-sized particles subject to gravitational and non-gravitational forces. My contribution to the paper was mainly the tidal evolution section, along with summaries of this section that appeared in the introduction and conclusion. Considering the tidal evolution of Pallene set limits on timescales over which to consider long-term evolution using `Mercury6`*, which does not include tides in its orbital integration. It also presented a plausible previous resonance from which Pallene may have escaped.*

Tables 5.1 and 5.2 appeared in between the paper's Introduction and Methods sections, but are included below because the text I have excerpted refers to them. Note also that although Figure 5.1 did not appear in the final published version of the paper, I have decided to include it here.

From the Introduction:

To examine the big picture of Pallene's tidal evolution, we use a simple model based on Murray and Dermott (1999), which assumes a linear tidal dissipation mechanism and a constant Q, independent of frequency. We only examine the tidal evolution of Pallene and the large moons in its vicinity, Mimas and Enceladus, in order to look at resonances that may have been crossed in the recent past, as well as to establish a time limit of the validity of the current orbital configuration of the system for the longer-term simulations.

Tidal evolution Section:

To gain an appropriate perspective on the timescales of Pallene's dynamical evolution, we first look at Pallene's tidal evolution in between Mimas and Enceladus. Although more complex analyses of tidal evolution in the Saturn system have recently been done (e.g. Fuller et al. 2016; Lainey et al. 2020), here we employ a simpler model to gain a general understanding of the context in which Pallene may have evolved. Using Equation 4.213 from Murray and Dermott (1999), we can calculate previous semi-major axes

$$a = a_0 \left[1 - \left(\frac{k_2}{Q} \frac{39 M_m R_S^5}{2 a_0^{13/2}} \sqrt{\frac{G}{M_S}} t \right) \right]^{2/13} , \tag{5.3}$$

assuming that the tidal dissipation mechanism is linear and that Q is frequency-independent.

For our tidal evolution calculations, we take our value for Saturn's Love number, $k_2 = 0.390$, from Lainey et al. (2017). We estimate a quality factor $Q = 2000$ also based on Lainey et al. (2017) and similar to what is used in Ćuk et al. (2016), which was based on the earlier work of Lainey et al. (2012), though there is less agreement on this value and it is meant to apply only near the semi-major axes roughly around Mimas and Enceladus. Previous estimates of Q an order of magnitude higher were due to the assumption that Mimas was primordial (Murray and Dermott, 1999; Meyer and Wisdom, 2008). However, recent studies that argue Saturn's rings and the mid-sized moons are probably young, use a Q value in the range we have assumed (Ćuk et al., 2016; Fuller et al., 2016; Lainey et al., 2017; Neveu and Rhoden, 2019; Hesselbrock and Minton, 2019). Other values for this calculation are given in 5.1 and 5.2.

Using these values, we measured the change in semi-major axis with respect to today's semi-major axis value $\frac{\Delta a}{a}$ over the past five million years for Mimas, Pallene, Enceladus, Tethys, and Dione. Out of these measurements, Mimas has $\frac{\Delta a}{a} = 0.0017$, which is the largest among these moons. Because this change in semi-major axis due to tidal evolution is small, we expect our long-term simulations of 5 Myr without the inclusion of tidal evolution to be accurate enough.

Table 5.1: Saturn's physical parameters.

Parameter	Value	Reference
R_S [km]	60 330	Kliore et al. (1980)
GM_S [km^3 s^{-2}]	3.793120749865220E+07	*gm_de431.tpc* [a]
J_2	1.6290573E-02	Iess et al. (2019)
J_4	-9.35314E-04	Iess et al. (2019)
J_6	8.6340E-05	Iess et al. (2019)
Ω_S [rad s^{-1}]	1.65269E-04	Helled et al. (2015)

[a] Available at https://naif.jpl.nasa.gov/pub/naif/generic_kernels/pck/gm_de431.tpc

Table 5.2: Summary of physical parameters of the six large moons in our system.

Name	GM_m [a] [km^3 s^{-2}]	ρ_m [g cm^{-3}]	R_m [b] [km]
Mimas	2.503522884661795E+00	1.152	198.2
Enceladus	7.211292085479989E+00	1.606	252.6
Tethys	4.121117207701302E+01	0.956	537.5
Dione	7.311635322923193E+01	1.469	561.4
Rhea	1.539422045545342E+02	1.233	763.8
Titan	8.978138845307376E+03	1.880	2574.7

[a] GM_m values are taken from the planetary constant kernel *gm_de431.tpc*.

[b] Radius values, R_m, are taken from the planetary constant kernel *pck00010.tpc* (available at https://naif.jpl.nasa.gov/pub/naif/generic$_k$*ernels/pck/pck*00010*.tpc*, *Archinalet al.* 2011).

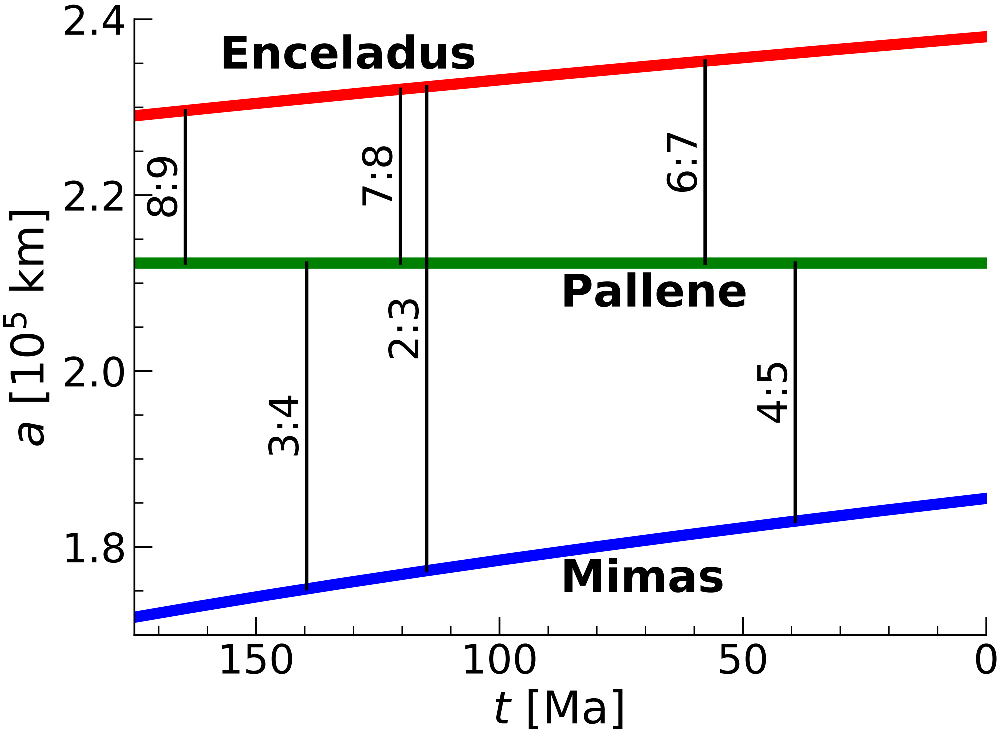

Figure 5.1: Tidal evolution of Enceladus, Pallene, and Mimas over the past 175 Ma based on Equation 5.3 (Murray and Dermott, 1999) with $Q = 2000$ and $k_2 = 0.390$ (Lainey et al., 2017). Pallene may have recently crossed the 4:5 resonance with Mimas and the 7:6 resonance with Enceladus. If Pallene were trapped in a resonance like one of these, it could have migrated with the larger moon for some period of time. Ultimately, Pallene's orbit may have crossed that of Enceladus, suggesting that Pallene could be a fragment from Enceladus.

From the semi-major axis calculations, if Pallene is old enough, it may have recently escaped the 4:5 resonance with Mimas (40 Myr ago with $Q = 2000$). Prior to escape, Pallene could have migrated with Mimas for a substantial period of time. For this reason, it becomes difficult to project Pallene's previous tidal evolution with much certainty. If Pallene was not captured in any resonance with Mimas for a significant period of time, which is unlikely because their orbits are converging, then further in the past Pallene's orbit may have crossed that of Enceladus (400 Myr ago with $Q = 2000$), suggesting that Pallene could be a fragment from Enceladus, similar to the way Showalter et al. (2019) propose that Hippocamp could have fragmented off of Proteus, possibly from a cometary impact.

Hippocamp is close to the orbit that is synchronous with Neptune's rotation, which, together with the fact that it is the least massive of Neptune's moons, implies that the rest of Neptune's moons are diverging from Hippocamp. In contrast, Pallene's orbit is converging with Mimas's orbit. For this reason, Pallene is expected to have been captured into resonance with Mimas at each resonance crossing, but it is difficult to determine the duration of the capture in each resonance.

Proteus and Hippocamp have mean radii of 203.8 km and 17.4 km (Showalter et al., 2019), while Enceladus and Pallene have mean radii of 252 km and 2.23 km (Roatsch et al., 2009; Thomas et al., 2013). Using these mean radii and masses of 1.08×10^{20} kg for Enceladus (Jacobson et al., 2006) and 4.4×10^{19} kg for Proteus (multiplying the volume from Stooke (1994) by an assumed density of 1.3 g/cm^3), the escape velocity $v_{\rm esc} = \sqrt{2GM_m/R_m}$ from the surface of Enceladus is 240 m/s, while for Proteus it is 170 m/s. Pallene has a smaller size ratio to Enceladus than Hippocamp has to Proteus, but perhaps Pallene is evidence of the proposed impactor in the south polar terrain of Enceladus (Roberts and Stickle, 2017).

Not too long in the past, however, is the Mimas-Enceladus 3:2 resonance crossing (115 Myr ago with $Q = 2000$). Meyer and Wisdom (2008) studied a triplet of Mimas-Enceladus 3:2 resonances and found that Mimas's eccentricity can be explained either by passage through the 3:2 e-Mimas resonance or the 6:4 ee'-mixed resonance (but not the 3:2 e-Enceladus resonance), and found dynamical escape to be possible for both of these resonances. Ćuk et al. (2016) proposed that Tethys, Dione, and Rhea all formed in one event about 100 Myr ago, and suggests that Mimas and Enceladus could have formed during the same epoch or could be even younger. Neveu and Rhoden (2019), however, have suggested that Mimas could be significantly younger than Enceladus. This last scenario allows for the possibility of Pallene migrating away from Enceladus after an impact before the formation of Mimas.

Thus, given a constant Q tidal model, it looks like Pallene has crossed some resonances, which, especially if it had been trapped in any of them for some period of time, could have affected its eccentricity and inclination. However, the new tidal models indicate the evolution of the satellites could be more complex than previously thought (Fuller et al., 2016; Lainey et al., 2020). Still, small moons such as Pallene are likely sensitive probes of this tidal evolution (see, for example, El Moutamid et al. 2017) and so should be considered in those contexts.

From the Conclusion:

We used a simple tidal evolution calculation for Mimas, Pallene, and Enceladus in order to set the context for our longer-term simulations. We made note that the most recent resonance Pallene may have escaped from is the 4:5 resonance with Mimas. Pallene's current eccentricity or inclination could be signs of this or another past resonance crossing.

From the Acknowledgements:

J. A'Hearn thanks M. Hedman, M. Tiscareno, and M. Showalter for useful discussions; and also thanks NASA for partial support through the *Cassini* Data Analysis and Participating Scientist Program grant NNX15AQ67G.

5.2.3 Inner Neptunian system

The Neptunian system provides an opportunity for us to apply lessons we have learned and to increase our understanding of tidal evolution. While the dynamics of the Neptunian system have thus far been only partially explored (see for example Banfield and Murray 1992; Porco et al. 1995), recent discoveries in the Neptunian system (Showalter et al., 2019; Brozović et al., 2020) as well as developments in tidal modeling (Fuller et al., 2016; Hesselbrock and Minton, 2019) have opened up the door for the Neptunian system to play a role in enlightening our understanding of tidal evolution.

Tidal evolution draws the inner prograde moons further inward, and resonance crossings can leave signatures on orbital parameters such as eccentricity and inclination, though for the Neptunian system the eccentricity damping timescale is significantly shorter than the inclination damping timescale (Zhang and Hamilton, 2007).

Naiad's high inclination (4.7°) has allowed it to be captured into a 73:69 resonance with Thalassa (Brozović et al., 2020). In particular, this means that the resonant argument $73\lambda_{\mathrm{Thalassa}} - 69\lambda_{\mathrm{Naiad}} - 4\Omega_{\mathrm{Naiad}}$ librates around 180°, where the orbital parameters λ represents the corresponding moon's mean longitude, and Ω represents the longitude of its ascending node. This is the only fourth-order resonance known between moons of the outer planets, and results in increasing the stability of the Naiad-Thalassa pair despite their proximity in semi-major axis because, whenever Naiad passes Thalassa, they have greater vertical than radial separation (Brozović et al., 2020). Naiad's inclination was most likely excited by a previous resonance (Banfield and Murray, 1992).

Multiple studies have looked at the past tidal evolution of Neptune's moons with a simple approach, using a constant, frequency-independent tidal dissipation parameter Q (Banfield and Murray, 1992; Zhang and Hamilton, 2007, 2008). I have reproduced this simple calculation (see Figure 5.2) with Equation 5.3, using $k_2 = 0.127$ (Gavrilov and Zharkov, 1977; Lainey, 2016), $Q = 12,000$ (Banfield and Murray, 1992; Showalter et al., 2019), $R = 24,764$ km (Archinal et al., 2018), $M = 1.024126 \times 10^{26}$ kg (Jacobson, 2009), and satellite masses m from Brozović (2020).

Banfield and Murray (1992) identified 35 candidate resonances and calculated the probabilities that Naiad had been captured in them, isolating three of these candidate resonances as the most probable, but they did not perform numerical orbital simulations.

Since these studies, Neptune's moon Hippocamp has been discovered in between the orbits of Larissa and Proteus (Showalter et al., 2019), and our understanding of tidal evolution has developed, including the cases of coupled ring-moon systems (Hesselbrock and Minton, 2017, 2019), of two moons in a resonance lock with each other (Gomes, 1997, 1998),

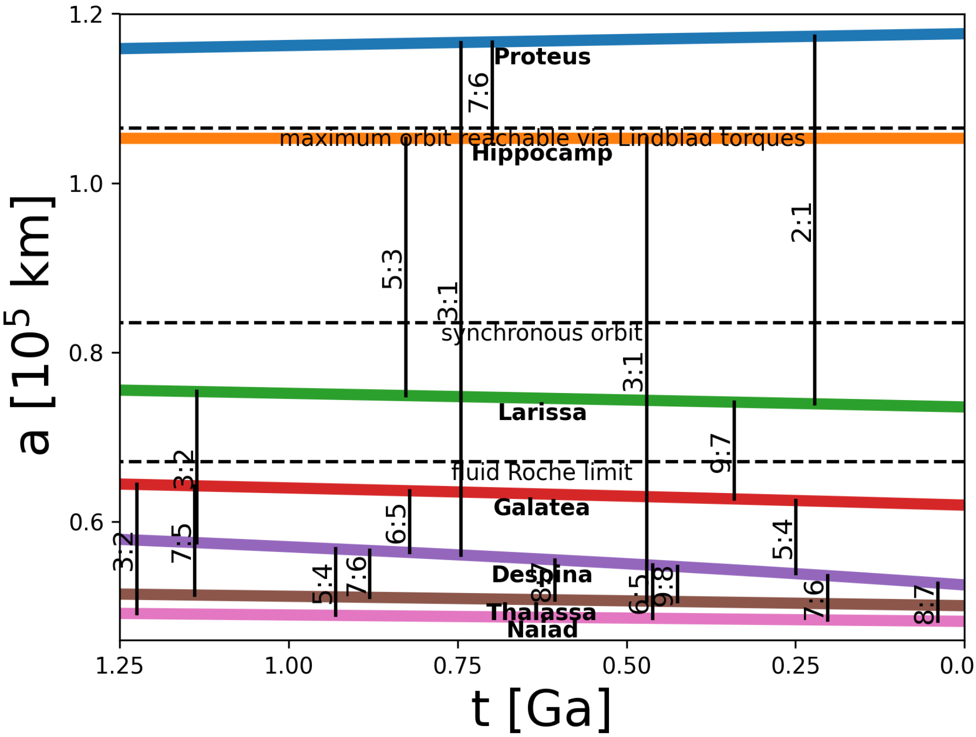

Figure 5.2: Semi-major axis vs. time into the past according to a simple tidal model. Only first- and second-order resonance crossings with $m < 10$ are shown. One or a number of previous second-order resonances are expected to have excited Naiad's inclination.

and of a moon in a resonance lock with a planetary normal mode (see below; Fuller et al. 2016). These advances have been applied in studies of the systems of Mars (Hesselbrock and Minton, 2017; Ćuk et al., 2020), Saturn (Fuller et al., 2016; Lainey et al., 2020), and Uranus (Hesselbrock and Minton, 2019). The locations of planetary normal mode resonances are dependent on the interior model, especially for low azimuthal order m. Some interior models place Neptunian normal mode resonances close to Naiad (see Chapter 4). Thus, how a moon might interact with a planetary normal mode resonance is a relevant question for the orbital evolution of Neptune's inner moons, especially Naiad and Thalassa.

The theory of resonance capture has focused on first- and second-order resonances, because these are the strongest and most common (Borderies and Goldreich, 1984; Dermott et al., 1988; Champenois and Vienne, 1999; Luan, 2014; Batygin, 2015; El Moutamid et al., 2017). The recent discovery of Naiad and Thalassa's fourth-order resonance (Brozović et al., 2020) provides a motivation to extend the theory of resonance capture to fourth order.

Using an equation for resonance width that is intended to apply to first-order resonances (El Moutamid et al., 2017; A'Hearn et al., 2019), I have estimated the width of the Naiad-Thalassa resonance to be only about 4 km, but derivation of an equation that is specific to fourth-order resonances can clarify this quantity. Capture probability depends on the order of the resonance, resonance width, drift rate, and initial eccentricity and inclination (Quillen, 2006; Namouni and Morais, 2017). The development of theory for fourth-order resonances and the analysis through numerical simulations constitute an avenue for possible future research. Understanding the conditions that allowed capture into the Naiad-Thalassa resonance will help constrain tidal evolution rates in the Neptunian system, which can shed light on Neptune's interior and the history of the Neptunian system.

An investigation starting with Equation 5.3 and also taking into account resonances between moons (Gomes, 1997, 1998) is all that may be required to examine tidal evolution through the three most probable candidate resonances that are thought to have excited Naiad's inclination to its current value: the 12:10, 11:9, and 10:8 inclination resonances (Banfield and Murray, 1992). In addition to resonances between moons, other factors that can affect tidal evolution are feedbacks between rotational, orbital, and thermal evolution (Park et al., 2019). Furthermore, other interactions that can be important include ring torques (Hesselbrock and Minton, 2017, 2019) and resonances with planetary normal modes (Fuller et al., 2016).

Neptune's current ring system is much less massive compared to Saturn and Uranus, but it may have been larger in the past. Modeling the interaction between ring torques and moons can be done with a code called `RINGMOONS` (Hesselbrock and Minton, 2017), which approximates the gridspace of the ring as a one-dimensional Eulerian series of bins, extending from the surface of the planet to the fluid Roche limit. `RINGMOONS` has recently been integrated into a more general N-body code called Swiftest (Duncan et al., 1998; Minton et al., 2021). Looking at these interactions can help us constrain how ring torques may have played a role in the evolution of Neptune's inner moons, and likewise how the inner moons could constrain the history of Neptune's current rings.

So far there exists theory concerning how planetary normal mode resonances interact with rings (Marley and Porco, 1993). There is room to further develop the theory of how planetary normal mode resonances interact with moons on short timescales, which can be applied to Neptune's rings and inner moons to improve our understanding of the recent past tidal evolution of the Neptunian system. A particular test is to see if Naiad's inclination could have been excited by a vertical resonance with a planetary normal mode instead of by an inclination resonance with Despina, as mentioned in Chapter 4.

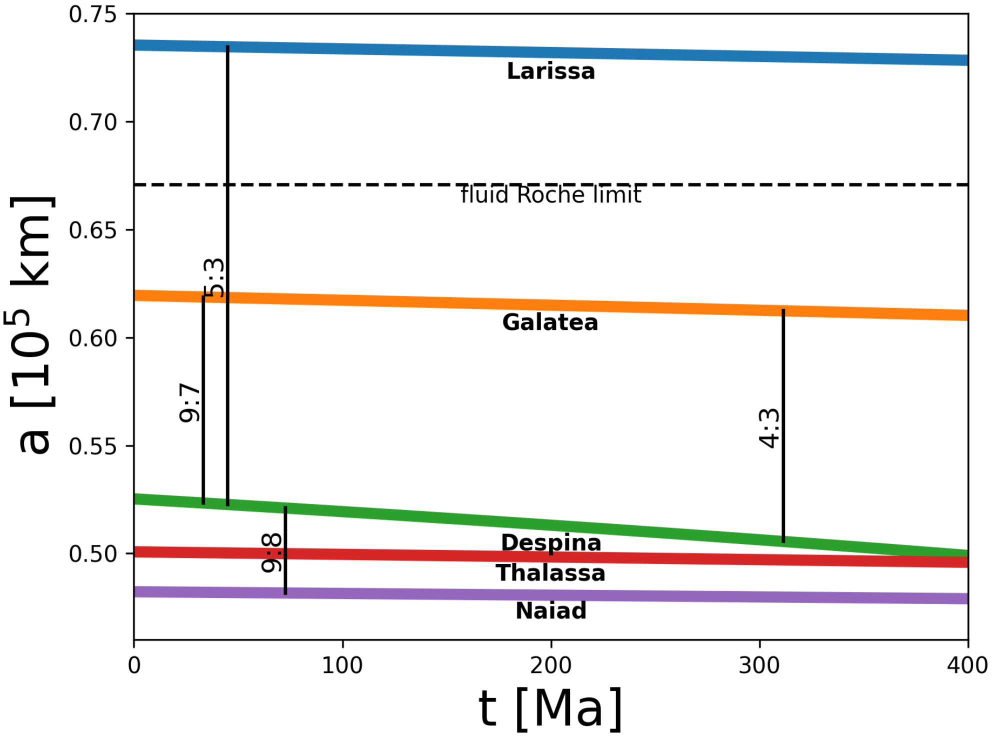

Figure 5.3: Semi-major axis vs. time into the future according to a simple tidal model. A few hundred million years into the future, Despina will approach Thalassa and Naiad to form what we expect to be an increasingly unstable tightly packed system. Note that this Figure is an extension that continues further to the right from where Figure 5.2 leaves off.

Despina is evolving inward via tides faster than other nearby moons due to its larger mass. In the future, Despina's perturbations on Naiad and Thalassa could destabilize the inner Neptune system sometime in the next few hundred million years, according to a simple tidal model calculation (see Figure 5.3). Thus, a detailed investigation of how we can expect the disruption of Neptune's inner moons to play out is of interest. Many studies of closely packed planetary systems will be relevant for this investigation (Wisdom, 1980; Gladman, 1993; Smith and Lissauer, 2009; Funk et al., 2010; Quillen, 2011; Deck et al., 2013; Boley et al., 2014; Hussain and Tamayo, 2020; Petit et al., 2020; Lissauer and Gavino, 2021).

5.2.4 Resonance locking

Orbits of moons and planets change over time due to many factors, including tidal interactions with their host bodies and resonant interactions with other orbiting bodies. Tidal heating and coupled orbital migration are key to the evolution and habitability of worlds, including several moons in the outer Solar system as well as exoplanets (Park et al., 2019). Nevertheless, we still have a poor grasp on the origin of tidal energy dissipation required for this orbital evolution around giant planets and stars. A variety of mechanisms can produce accelerated tidal migration. Standard mechanisms are interaction with rings (Goldreich and Tremaine, 1980) and resonances with other moons (Gomes, 1998). These two mechanisms can often be in competition with each other (Dawson and Murray-Clay, 2013). Recent work, however, shows that another mechanism, resonance locking with the planet's internal oscillation (normal) modes, can also produce rapid tidal migration (Fuller et al., 2016). Without disregarding the importance of ring-satellite interactions or resonances between moons, we must improve our understanding of resonance locking with planetary normal modes to better understand orbital evolution around giant planets and small stars.

As a planet or star ages, its oscillation mode frequencies evolve. Resonance locking occurs when the coupled evolution of the oscillation mode frequency of the central body and the orbital frequency of the perturbing body allows the perturber to remain near resonance with the oscillation mode. Resonance locking predicts a migration timescale that is similar to tidal evolution with constant tidal quality factor Q, but with a different effective Q governing each moon or planet's migration (Fuller et al., 2016). Planetary contraction alone would lead to spin-up, due to conservation of angular momentum. Over time, however, planetary interiors cool (Fortney and Nettelmann, 2010). Cooling as well as transfer of angular momentum from the planet to its moons can allow the planet's rotation rate to slow down, which moves the inertial wave frequencies outward. So far, no interior evolution studies have been performed of inertial waves in evolving planets (Fuller et al., 2016).

One avenue for possible future research, therefore, is to explore how internal oscillation modes evolve with the planet and how this might affect satellite orbital evolution. In Figure

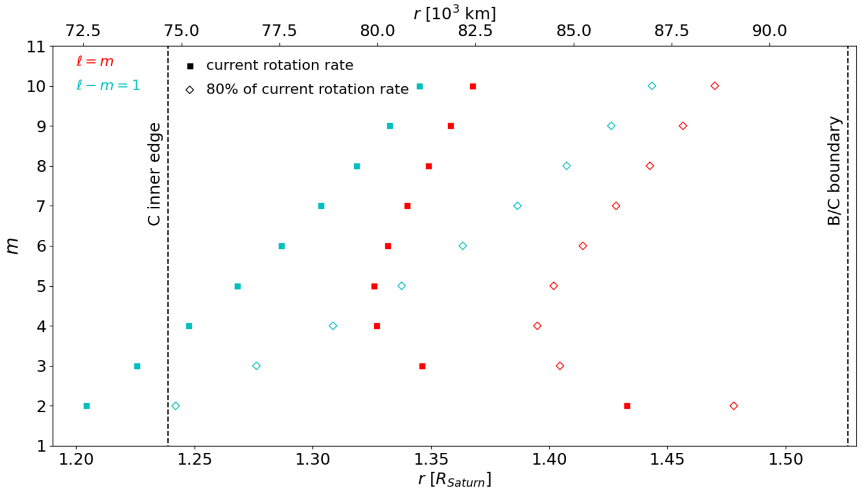

Figure 5.4: Internal oscillation mode resonance locations that fall in Saturn's C ring based on an interior model from C. Mankovich. Oscillation order m is plotted against radial distance r. Filled-in square points correspond to resonance locations using Saturn's current rotation rate; whereas empty diamond points correspond to resonance locations using a slower rotation rate (80% of Saturn's current rotation rate). This demonstrates how resonance locations can change as a planet evolves, and in particular, that the resonance locations do not all change by the same amount. For modeling resonance locking dynamics, however, a more comprehensive and self-consistent interior evolutionary model is desirable.

5.4, I show the difference in resonance locations by modifying only the planet's rotation rate, which is merely one quantity that changes as a planet evolves. The resonance locations of different oscillation orders m change by different amounts. To model resonance locking dynamics, a more comprehensive and self-consistent interior evolutionary model is desired.

The first step would be to generate a suite of models that correspond to an evolving giant planet at different time steps to investigate the evolution of planetary normal modes. To do this, it may be possible to use the new planetary evolution code `planetsynth` (Müller and Helled, 2021) that was designed specifically for giant planets. Otherwise, following the methods outlined in Mankovich and Fuller (2021) to generate these models would be sufficient. Orbital evolution rates that result from different planetary evolution models can then be explored in order to test and refine resonance locking theory.

A second step would be to examine how planet-driven migration and satellite resonances interact. This investigation could include resonance locks of moons with planetary normal modes (Fuller et al., 2016), resonances between moons (Gomes, 1997, 1998), and coupled ring-moon systems (Hesselbrock and Minton, 2017, 2019). The combination of all three of these processes could be analyzed in order to produce an improved model. This could be done by considering the cases of Neptune, as explained previously, and of Saturn and exoplanets, as explained below. In these cases a comparison can be made between the effects on a rocky moon vs. a moon with a subsurface ocean.

The orbital evolution of the Saturnian system is an active field, with different theories about the ages and migration of Saturn's inner mid-sized moons: Mimas, Enceladus, Tethys, Dione, and Rhea (Ćuk et al., 2016; Asphaug and Reufer, 2013; Neveu and Rhoden, 2019). Numerical simulations of these moons that couple thermal, geophysical, and simplified orbital evolution have reproduced the observed characteristics of their orbits and interiors, as long as the outer four moons are old (Neveu and Rhoden, 2019). Mimas's proximity to Saturn's rings generates interactions that cause such rapid orbital expansion that Mimas must have formed 10^8-10^9 years ago if it postdates the rings (Neveu and Rhoden, 2019). Saturn's mid-sized moons each evolve with a different effective tidal Q (Fuller et al., 2016; Lainey, 2016; Lainey et al., 2020). Although Mimas has long been considered a dead world, a case has recently been made that Mimas may in fact be a "stealth" ocean world (Rhoden and Walker, 2022). The application of resonance locking studies to the Saturnian system could also shed light on this unsettled issue.

All the relevant mechanisms must be included to explain how the Saturnian system has evolved. Ring torques are important due to the mass of Saturn's rings (Hesselbrock and Minton, 2019; Nakajima et al., 2020). Many of Saturn's moons are in resonances, including the Mimas-Tethys 4:2 resonance and the Enceladus-Dione 2:1 resonance (Murray and Dermott, 1999), and recent work has shown that also three-body resonances, which have been neglected in past studies, must be taken into account for an accurate investigation of the Saturnian system's past (Ćuk and El Moutamid, 2022). Resonance locking with normal modes in the planet can allow subsurface oceans to persist even in small moons like Enceladus and can also serve as the mechanism to drive rapid tidal expansion in Saturn's large moon Titan (Fuller et al., 2016; Park et al., 2019; Lainey et al., 2020). The combination of these mechanisms should be studied in order to provide a more detailed model of how the system has evolved.

Exoplanet systems are then left as the final case to be explored based on insights from the previous two case studies. The study of nonradial oscillations developed first for stars before giant planets (Unno et al., 1979). With the developments contributed first for giant planets, these can then be extended primarily to small stars, such as M dwarfs. Rotation rates of a minority but still significant amount of M dwarfs are not too different from those of our Solar system's giant planets (Reiners et al., 2018). Many exoplanetary systems around a broader range of stellar spectral types have planets that are just wide of resonance (Fabrycky, 2010; Fabrycky et al., 2014), indicating that resonances between planets are insufficient to explain the dynamics that are at play.

For this research avenue, one can run M dwarf system simulations that evolve both the star and what orbits it. `MESA` code (Paxton et al., 2011) has been widely used for stellar evolution. For orbital evolution, one could use a combination of `RINGMOONS`, `SIMPL`, and `MERCURY6`. `RINGMOONS` can best model the final stages when a protoplanetary disk is still present, thus involving disk-planet torques, analogous to the ring-moon torques among the outer planets of our Solar system. `SIMPL` simulations can explore resonance locking with internal oscillation modes and resonant dynamics between planets. `MERCURY6` simulations can be used to investigate small timescales if planets become tightly packed and would experience close encounters with each other (`SIMPL` does not handle close encounters). The objective of these simulations would be to produce orbital architectures that are similar to what we observe today among the population of M dwarf exoplanetary systems (Fabrycky, 2010; Fabrycky et al., 2014).

5.3 Further co-orbital satellite dynamics studies

In Chapter 3 I presented an application of co-orbital dynamics to Saturn's D68 clumps. Here I share additional topics that I have begun to explore related to co-orbital satellite dynamics.

The study of the dynamics of co-orbital systems is motivated by the many cases of co-orbital systems we find in our solar system as well as the potential for finding cases of co-orbitals among exoplanetary systems. We are especially interested here in systems in which the co-orbitals have comparable masses. The best known system this would apply to would be the horseshoe orbits of Janus and Epimetheus (Dermott and Murray, 1981a).

5.3.1 Janus and Epimetheus

Saturn's moons Janus and Epimetheus are co-orbital. Though one of them is almost always closer to Saturn than the other, they swap orbits every four years. A demonstration I have simulated of this orbital swap is shown in Figure 5.5. Janus is 3.6 times more massive than Epimetheus (Jacobson et al., 2008), which is directly proportional to how much their semi-major axes change during an orbital swap: $\sim$ 21 km for Janus and $\sim$ 76 km for Epimetheus, preserving the ratio of 3.6 (El Moutamid et al., 2016). When Epimetheus is closer to Saturn than Janus, it has a shorter orbital period and approaches Janus from behind. The closer they approach each other, the stronger their gravitational interaction, and the faster the rate of angular momentum transfer. Janus pulls Epimetheus forward, while Epimetheus pulls Janus backward. As Janus slows down, it falls toward Saturn in its orbit, now taking an inside track, while Epimetheus speeds up and thus rises away from Saturn in its orbit, moving to an outside track. In this manner they swap their orbits. The same procedure happens, though switching "Janus" for "Epimetheus" and vice versa in the above explanation, when Janus approaches Epimetheus from behind.

5.3.2 Discovery of horseshoe-like trajectories for $N = 3$ co-orbitals

This Section presents a discovery I have made and presented at a conference, but have not yet finished writing up as a scientific journal article.

Although no co-orbital systems have yet been found among exoplanets, it is expected that they should exist. Granados Contreras and Boley (2018) suggest that in some cases co-orbitals can form from tightly packed systems. Veras et al. (2016) state that co-orbital configurations of nearly equal-mass objects may be produced upon the fragmentation or disintegration of objects orbiting near the disruption radius of their host star. Moreover, planetary system formation models predict the formation of some co-orbital systems (Laughlin and Chambers, 2002; Beaugé et al., 2007). If such a system were to be found, it would be necessary to distinguish the system of N co-orbitals orbiting once per period T from a hypothetical planet orbiting N times per period T.

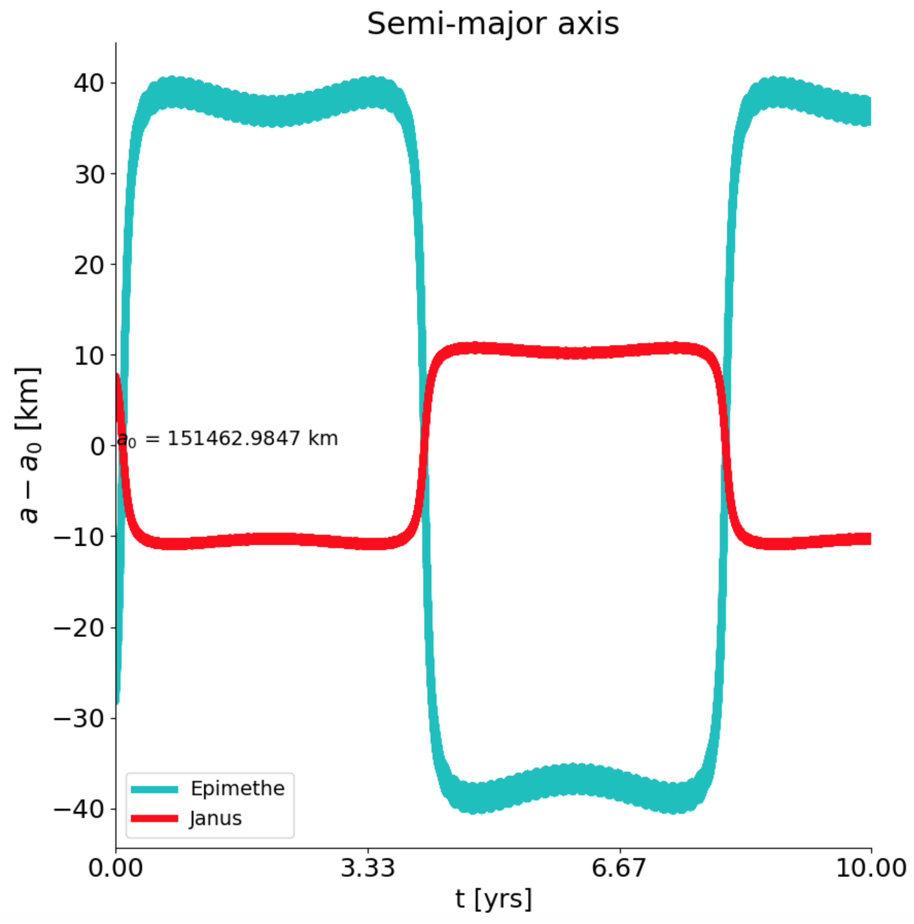

Figure 5.5: Semi-major axis vs. time for a simulation I ran of Janus and Epimetheus, showcasing their periodic orbital swap.

Some studies have considered the detectability of co-orbitals from radial velocity data (Laughlin and Chambers, 2002; Giuppone et al., 2012; Leleu et al., 2015). Others have also investigated the effect of co-orbitals on transit-timing variations (Vokrouhlický and Nesvorný, 2014; Leleu et al., 2017). Most work on co-orbital systems has focused on the case with $N = 2$ co-orbitals. In this Section I build on previous work, but focus my attention on the case of $N = 3$ co-orbitals. Verrier and McInnes (2014) grouped into families some of the periodic orbits for $N = 3$ and $N = 4$ co-orbitals. Here I report a new family of horseshoe-like orbits for $N = 3$ equal-mass co-orbital systems. I also investigate preferred longitudinal separations, which is relevant for breaking the degeneracy for transit-timing variations.

Salo and Yoder (1988) originally examined stationary configurations of equal-mass co-orbital satellites for small N ($N \leq 9$) using a simple first-order theory, neglecting terms of the order $(m/M)^{3/2}$, where m and M are the masses of the satellite and the primary. A numerical search revealed three distinct types of stationary solutions, of which we are here concerned with only one, which Salo and Yoder (1988) label Type Ia: an equilibrium where all the N satellites are most concentrated on the same side of the common orbit. The case where $N = 2$ is the well known Trojan configuration, with an angular separation of 60 degrees. Type Ia configurations are stable for $2 \leq N \leq 8$ but are not found for $N \geq 9$ (Salo and Yoder, 1988). With increasing N, each angle in the Type Ia configuration becomes more compact until $N = 8$. For $N = 8$ the angular separations between the middle six co-orbitals are more compact, as expected, but the angular separations are more expanded between the leading and second co-orbitals and between the trailing and penultimate co-orbitals, probably because the leading and trailing co-orbitals are extended beyond the semi-circumference (180 degrees) centered on the mid-point between the middle two co-orbitals. This study focuses on configurations with $N = 3$.

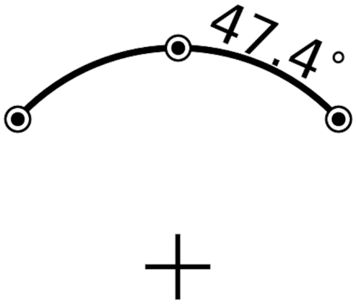

Figure 5.6: The stable compact configuration (Type Ia) for $N = 3$ co-orbitals.

The fact that co-orbital exoplanets have not yet been discovered may be partially due to observational bias, because near certain equilibrium points the difference in transit timing may be attributed to a perturbation from a planet on a different orbit (Leleu et al., 2017). Leleu et al. (2015) showed that the precision required to identify a pair of co-orbital planets depends only on the libration amplitude and the planets' mass ratio.

Salo and Yoder (1988) spoke of different modes of motion around the fixed solutions. The first mode they speak of we call the symmetric expansion mode. This became our approach for looking for periodic orbits. It's the simplest to implement because all N bodies begin

Table 5.3: Parameters used for numerical simulations, based on a typical M1 dwarf (Kaltenegger and Traub, 2009) .

Parameter	Value
R	$0.49R_{\odot}$
M	$0.49M_{\odot}$

with the exact same semi-major axis and differ only in longitude. Also, because Salo and Yoder (1988) say that all the modes mix in the symmetric expansion mode, this mode also serves as the best test for stability.

Verrier and McInnes (2014) studied periodic orbits for three and four co-orbital bodies. They find three different families of orbits for three co-orbitals and six different families of orbits for four co-orbitals. Their approach involves small oscillations from equilibrium. We didn't limit our initial longitudes to small oscillations. Instead, we ran orbital simulations with initial longitudes through the entire longitude range, with a longitude step of 5 degrees.

We carried out our simulations using `Mercury6` code (Chambers, 1999) for a range of masses for $N = 2$ and $N = 3$. Plots we found useful for analyzing the stability and evolution of different initial configurations include an aerial view in a co-rotating frame and a plot of relative longitude over time.

My initial orbital simulations used Saturn as the central mass, though in order to present this discovery more fittingly to the exoplanet community, I later changed the radius and mass of the central body to that of a typical M1 dwarf (Kaltenegger and Traub, 2009) (see Table 5.3) and neglected gravitational harmonics ($J_2 = J_4 = J_6 = 0$).

To express our results in a more general way, however, we convert time to orbits, we use mass ratios rather than absolute masses, and we express distances in terms of either the common semi-major axis of the co-orbitals or the Hill radius of each co-orbital mass. The highest mass we used was $m = 2.0 \times 10^{20}$ kg, which corresponds to a mass ratio of each co-orbital mass m_i to the central body's mass M of $\frac{m_i}{M} = 3.5 \times 10^{-7}$. Orbital oscillations and evolution happen faster at higher masses.

Using Kepler's 3rd Law $n^2 a^3 = \mu = GM$, we calculated the semi-major axis that would correspond to a period of one day if the masses of the co-orbitals are ignored, and rounded this result to $a = 2,308,120$ km. We used a time step of 0.1 days, a tenth of the orbital

Table 5.4: Parameters of co-orbitals used for numerical simulations

Parameter	Value
a	2,308,120 km

period.

To explore how a transiting co-orbital exoplanet might appear to observers, we created synthetic transit data from some of our orbital simulations. This was done by choosing an arbitrary reference angle from which an observer might observe the star at an infinite distance. We produce an output file with time and normalized flux data, including random noise of ±0.001 in the normalized flux data. What remains to be done is to then use the exoplanet code for transit-fitting.

We explored variations in two parameters: mass and perturbations in initial longitude. When we start the bodies out at their equilibrium points, we can see that their relative longitude stays pretty much constant throughout the whole simulation. When we expand their initial longitudes, we can see small oscillations in a tadpole-like region, and then a chaotic zone, and at the very end a small horseshoe-like region. The horseshoe- and tadpole-like regions scale differently with mass, though more work is required to confirm the exponents that describe these relations. We get larger horseshoe-like regions for smaller masses.

This simulation was closest to the edge of the tadpole-like region. The middle body remains in the middle. The leading and trailing bodies exhibit pretty symmetric features.

Far from equilibrium and beyond the chaotic zone, we find a horseshoe-like region. Because it's $N = 3$ and not $N = 2$ we don't get a completed horseshoe, but we call it horseshoe-like because the bodies swap orbits with an exchange of energy and angular momentum, like Janus and Epimetheus.

Kaplan and Cengiz (2020) observe that the maximum semi-major axis libration range is found in horseshoe-type co-orbitals. We observe this also in our simulations. Horseshoe-type co-orbitals also have the greatest difference between points of closest approach and farthest distance away. For lower masses we ran longer simulations and confirm that the horseshoe-like region is larger because it scales differently with mass than the tadpole-like

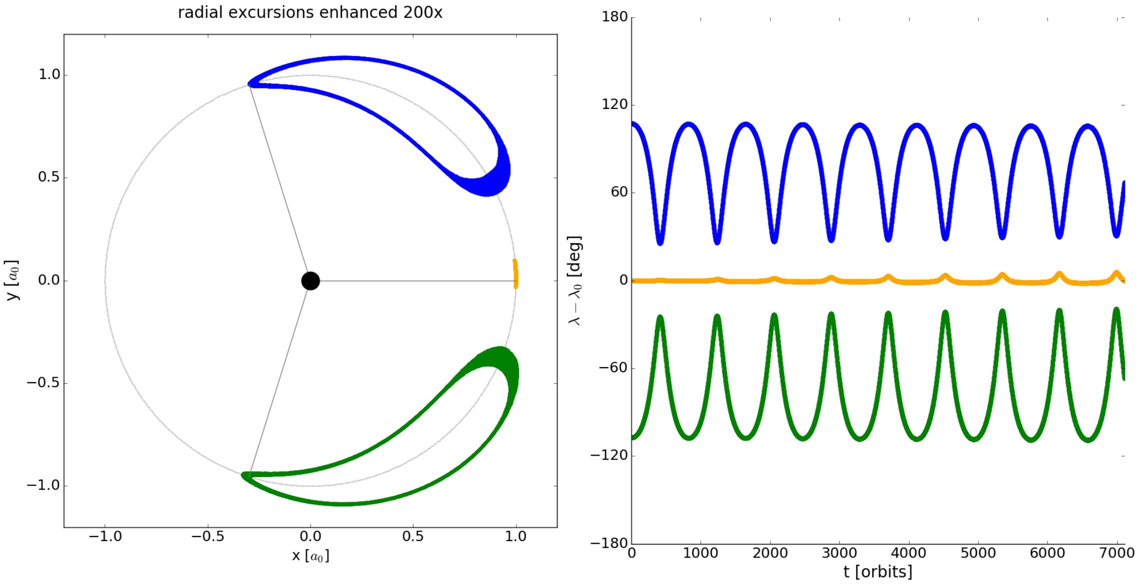

Figure 5.7: An example simulation with the initial longitudes close to the edge of the tadpole-like region.

region. The specific scaling of these regions still needs to be confirmed.

With a little bit wider initial angular separation than the tadpole region, we are on the fringe of the chaotic zone. With the next simulation, we know we're well into the chaotic zone. The middle body changes and becomes the trailing body. Salo and Yoder (1988)'s Type II configuration for $N = 3$ where the bodies begin with an equiangular distance between them, 120 degrees apart, is an unstable equilibrium. This simulation was the closest one to that unstable equilibrium. We can see that the bodies like to be about 120 degrees apart (see Figure 5.10), but when they start crowding in, they do that fast, and then go out again. The middle body switches among all three bodies. As we continue to increase the initial angular separation between the leading body and middle body and between the middle body and trailing body, we find several simulations in which the middle body is intended to be a certain one of them, but from the beginning, it becomes a different one. Then we get back to more chaos in which the middle body switches. In no simulations do we get a body on a different orbit so that it drifts by the other bodies. They all maintain co-orbital status no matter how chaotic the simulation becomes.

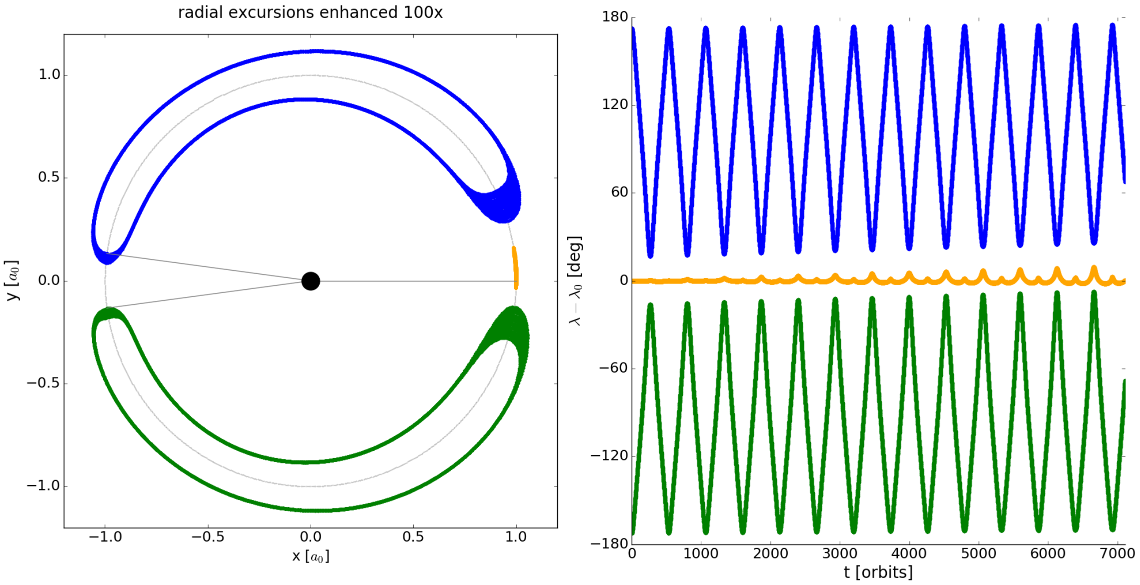

Figure 5.8: An example simulation with the initial longitudes far from equilibrium points. The results are horseshoe-like orbits.

Salo and Yoder (1988) provide an important investigation into coorbital satellite systems. For a system of N coorbital bodies, there are $N-1$ modes. For example, a system with $N=3$ coorbitals has a symmetric mode and an asymmetric mode. Thus for each additional co-orbital, the system acquires a new dimension of complexity. For simplicity, we focus on the mode of symmetric expansion (or contraction), which Salo and Yoder (1988) found to mix the other modes and to be the most unstable.

Our findings are consistent with Laughlin and Chambers (2002) and Ćuk et al. (2012). With the largest masses that we used, 2.0×10^{20} kg each, and with Saturn as the central mass, the highest mass ratio of satellites to the whole system is

$$\mu_{max} = \frac{2m}{2m+M} = 7.0 \times 10^{-7} \tag{5.4}$$

which is well below the stability limits for an equal-mass $N=2$ co-orbital system determined by Laughlin and Chambers (2002): $\mu < 4 \times 10^{-4}$ for horseshoe configurations and $\mu < 3.812 \times 10^{-2}$ for equilateral (tadpole) configurations.

To summarize our simulations, we can look at radial oscillation amplitude with respect

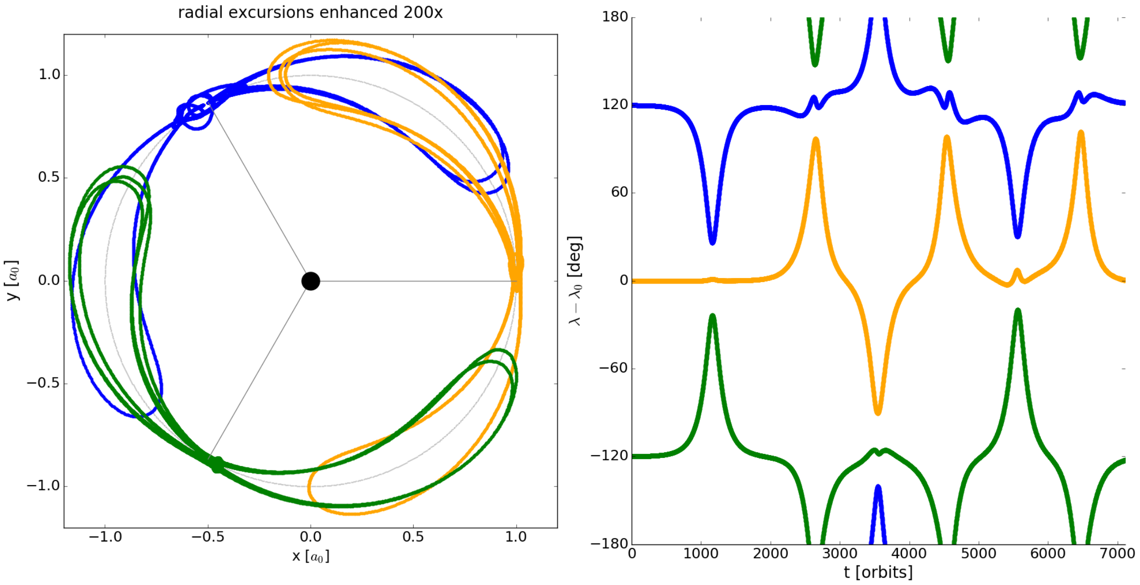

Figure 5.9: An example simulation with the initial longitudes close to the unstable equilibrium points.

to initial separation between the bodies (see Figure 5.13). Radial oscillation amplitude is defined as the maximum of any of the N bodies, and the initial separation is between the leading body and second body. Note that the scale for radial oscillation amplitude is logarithmic. The big dip happens close to equilibrium. This inflection point near the edges is due to the horseshoe-like region. The other dip is probably just due to the simulation not being long enough because the libration timescale is larger close to the region of unstable equilibrium.

To sum up, here are a few highlights. We found a new horseshoe-like family of periodic orbits far from equilibrium. We found a chaotic zone associated with the unstable equally spaced initial configuration. We confirm that the horseshoe-like and tadpole-like ranges scale differently with mass.

I have also performed simulations with $N = 4$ and $N = 5$ and have observed similar dynamics. Instead of investigating each case separately, however, I see this as an opportunity to apply machine learning techniques for arbitrary N, especially large N.

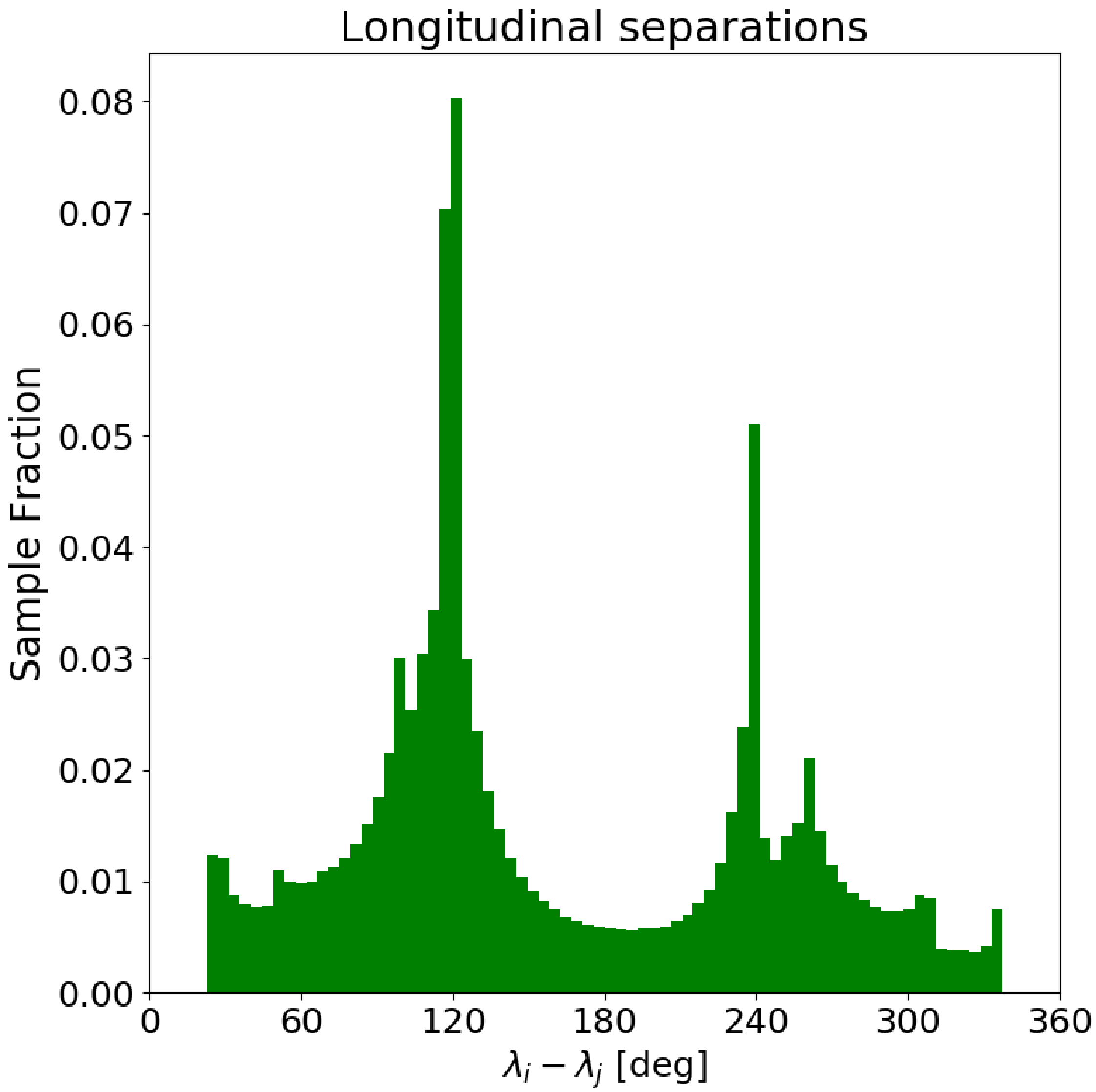

Figure 5.10: Histogram of the longitudinal separations for the simulation closest to the $N = 3$ unstable equiangular initial configuration. The bodies spend more time close to the equiangular configuration.

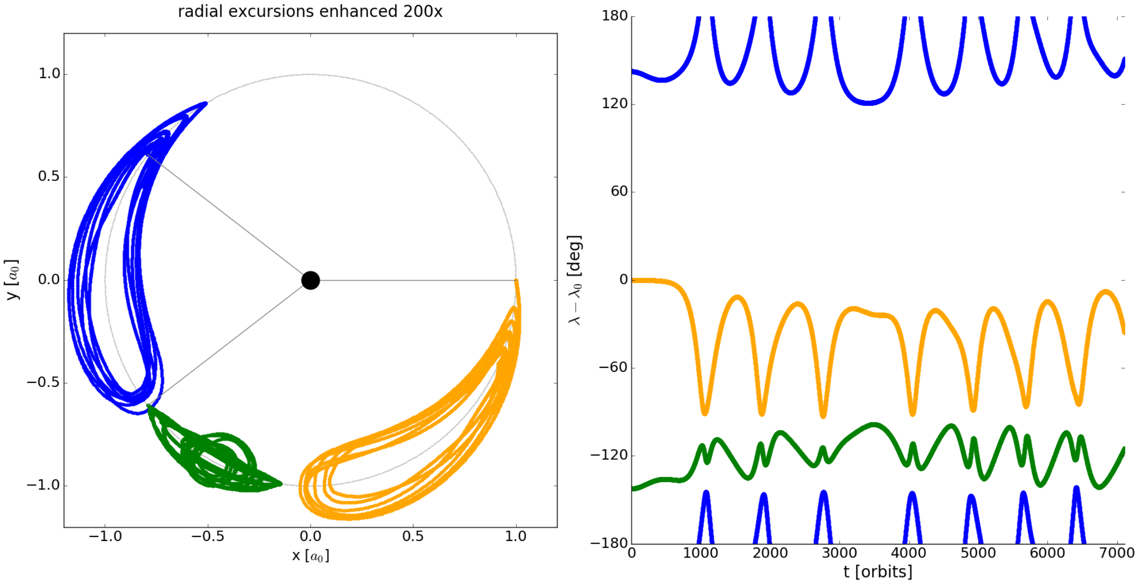

Figure 5.11: An example simulation with the initial longitudes in the chaotic region. The middle body ends up being one that was intended to be the trailing body.

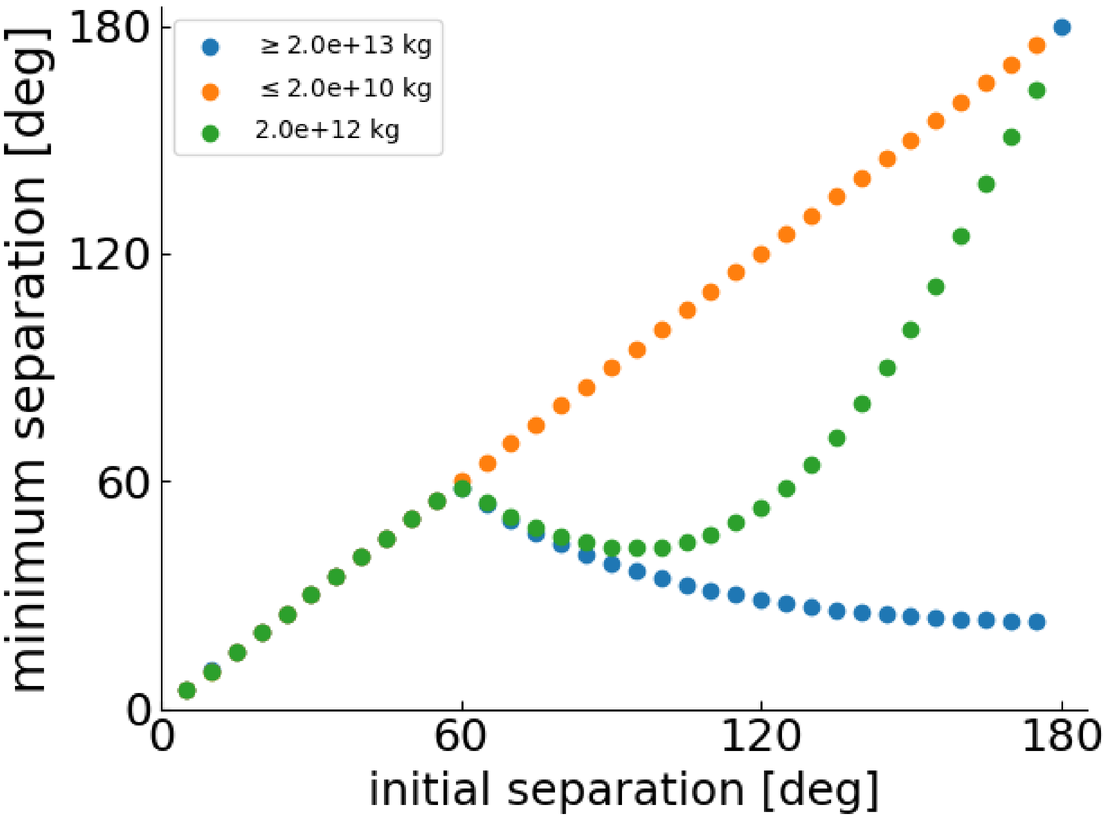

Figure 5.12: Masses smaller than a certain threshold maintain their initial longitudinal separation. Large masses exhibit regions of tadpole motion and regions of horseshoe motion.

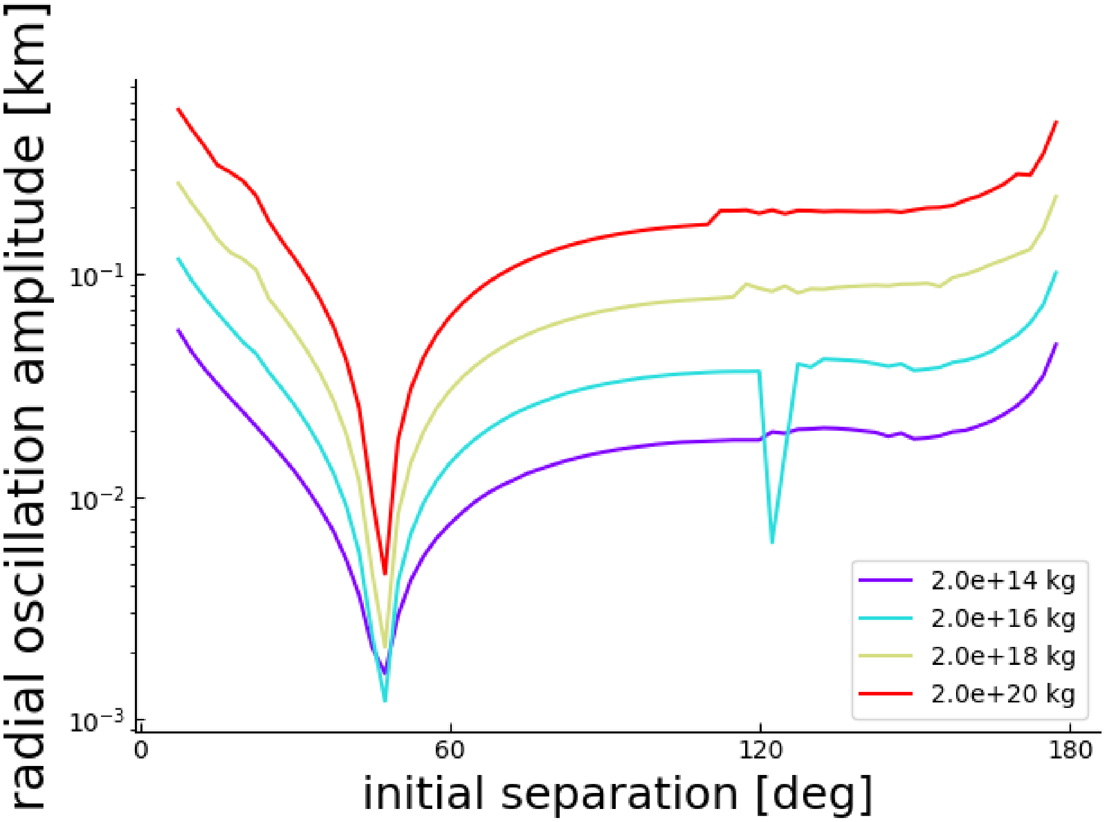

Figure 5.13: Radial oscillation amplitude, defined as the maximum of any of the N bodies, vs. initial separation between the leading body and second body. The equilibrium point at 47.4° is the dominant influence on the trends. Near 180° are inflection points that mark a transition to a horseshoe-like region. The trough particular to the cyan line near 120° is likely due to a single simulation being not long enough to observe libration.

Bibliography

C. H. Acton. Ancillary data services of NASA's Navigation and Ancillary Information Facility. , 44:65–70, January 1996. doi: 10.1016/0032-0633(95)00107-7.

Joseph A. A'Hearn, Matthew M. Hedman, and Maryame El Moutamid. Dynamics of Multiple Bodies in a Corotation Resonance: Conserved Quantities and Relevance to Ring Arcs. *The Astrophysical Journal*, 882(1):66, Sep 2019. doi: 10.3847/1538-4357/ab31af.

Joseph A. A'Hearn, Matthew M. Hedman, and Douglas P. Hamilton. Modeling Saturn's D68 Clumps as a Co-orbital Satellite System. *The Planetary Science Journal*, 2(2):74, April 2021. doi: 10.3847/PSJ/abed57.

B. A. Archinal, M. F. A'Hearn, E. Bowell, A. Conrad, G. J. Consolmagno, R. Courtin, T. Fukushima, D. Hestroffer, J. L. Hilton, G. A. Krasinsky, G. Neumann, J. Oberst, P. K. Seidelmann, P. Stooke, D. J. Tholen, P. C. Thomas, and I. P. Williams. Report of the IAU Working Group on Cartographic Coordinates and Rotational Elements: 2009. *Celestial Mechanics and Dynamical Astronomy*, 109(2):101–135, February 2011. doi: 10.1007/s10569-010-9320-4.

B. A. Archinal, C. H. Acton, M. F. A'Hearn, A. Conrad, G. J. Consolmagno, T. Duxbury, D. Hestroffer, J. L. Hilton, R. L. Kirk, S. A. Klioner, D. McCarthy, K. Meech, J. Oberst, J. Ping, P. K. Seidelmann, D. J. Tholen, P. C. Thomas, and I. P. Williams. Report of the IAU Working Group on Cartographic Coordinates and Rotational Elements: 2015. *CMDA*, 130(3):22, Mar 2018. doi: 10.1007/s10569-017-9805-5.

Erik Asphaug and Andreas Reufer. Late origin of the Saturn system. *Icarus*, 223(1):544–565, March 2013. doi: 10.1016/j.icarus.2012.12.009.

Martin Asplund, Nicolas Grevesse, A. Jacques Sauval, and Pat Scott. The Chemical Composition of the Sun. , 47(1):481–522, September 2009. doi: 10.1146/annurev.astro.46.060407.145222.

Kévin Baillié, Joshua E. Colwell, Jack J. Lissauer, Larry W. Esposito, and Miodrag Sremčević. Waves in Cassini UVIS stellar occultations. 2. The C ring. , 216(1):292–308, Nov 2011. doi: 10.1016/j.icarus.2011.05.019.

Don Banfield and Norm Murray. A dynamical history of the inner Neptunian satellites. *Icarus*, 99(2):390–401, October 1992. doi: 10.1016/0019-1035(92)90155-Z.

Konstantin Batygin. Capture of planets into mean-motion resonances and the origins of extrasolar orbital architectures. *MNRAS*, 451(3):2589–2609, August 2015. doi: 10.1093/mnras/stv1063.

C. Beaugé, Zs. Sándor, B. Érdi, and Á. Süli. Co-orbital terrestrial planets in exoplanetary systems: a formation scenario. *A&A*, 463(1):359–367, February 2007. doi: 10.1051/0004-6361:20066582.

M. Bethkenhagen, E. R. Meyer, S. Hamel, N. Nettelmann, M. French, L. Scheibe, C. Ticknor, L. A. Collins, J. D. Kress, J. J. Fortney, and R. Redmer. Planetary Ices and the Linear Mixing Approximation. , 848(1):67, Oct 2017. doi: 10.3847/1538-4357/aa8b14.

A. C. Boley, M. A. Morris, and E. B. Ford. Overcoming the Meter Barrier and the Formation of Systems with Tightly Packed Inner Planets (STIPs). *ApJL*, 792(2):L27, September 2014. doi: 10.1088/2041-8205/792/2/L27.

N. Borderies and P. Goldreich. A Simple Derivation of Capture Probabilities for the J+1:J and J+2:J Orbit-Orbit Resonance Problems. *Celestial Mechanics*, 32(2):127–136, February 1984. doi: 10.1007/BF01231120.

N. Borderies, P. Goldreich, and S. Tremaine. The dynamics of elliptical rings. , 88:1560–1568, October 1983. doi: 10.1086/113446.

F. Braga-Ribas, B. Sicardy, J. L. Ortiz, C. Snodgrass, F. Roques, R. Vieira-Martins, J. I. B. Camargo, M. Assafin, R. Duffard, E. Jehin, J. Pollock, R. Leiva, M. Emilio, D. I. Machado, C. Colazo, E. Lellouch, J. Skottfelt, M. Gillon, N. Ligier, L. Maquet, G. Benedetti-Rossi, A. Ramos Gomes, P. Kervella, H. Monteiro, R. Sfair, M. El Moutamid, G. Tancredi, J. Spagnotto, A. Maury, N. Morales, R. Gil-Hutton, S. Roland,

A. Ceretta, S. H. Gu, X. B. Wang, K. Harpsøe, M. Rabus, J. Manfroid, C. Opitom, L. Vanzi, L. Mehret, L. Lorenzini, E. M. Schneiter, R. Melia, J. Lecacheux, F. Colas, F. Vachier, T. Widemann, L. Almenares, R. G. Sandness, F. Char, V. Perez, P. Lemos, N. Martinez, U. G. Jørgensen, M. Dominik, F. Roig, D. E. Reichart, A. P. Lacluyze, J. B. Haislip, K. M. Ivarsen, J. P. Moore, N. R. Frank, and D. G. Lambas. A ring system detected around the Centaur (10199) Chariklo. *Nature*, 508(7494):72–75, April 2014. doi: 10.1038/nature13155.

Shawn M. Brooks, Tracy M. Becker, K. Baillié, H. N. Becker, E. T. Bradley, J. E. Colwell, J. N. Cuzzi, I. de Pater, S. Eckert, M. El Moutamid, S. G. Edgington, P. R. Estrada, M. W. Evans, A. Flandes, R. G. French, Á. García, M. K. Gordon, M. M. Hedman, H. W. Hsu, R. G. Jerousek, E. A. Marouf, B. K. Meinke, P. D. Nicholson, S. H. Pilorz, M. R. Showalter, L. J. Spilker, H. B. Throop, and M. S. Tiscareno. Frontiers in Planetary Rings Science. *arXiv e-prints*, art. arXiv:2008.12418, August 2020.

D. Brouwer and G. M. Clemence. *Methods of celestial mechanics.* 1961.

M. Brozović. In *Update of the inner Neptunian satellite orbits: NEP097*, Horizons/NAIF, 2020.

Marina Brozović and Robert A. Jacobson. The Orbits of the inner satellites of Uranus: solution URA115. In *Interoffice Memo. 392R-19-007 (internal document)*, 2019.

Marina Brozović, Mark R. Showalter, Robert A. Jacobson, Robert S. French, Jack J. Lissauer, and Imke de Pater. Orbits and resonances of the regular moons of Neptune. *Icarus*, 338:113462, March 2020. doi: 10.1016/j.icarus.2019.113462.

J. A. Burns. Elementary derivation of the perturbation equations of celestial mechanics. *American Journal of Physics*, 44(10):944–949, October 1976. doi: 10.1119/1.10237.

C. Cavazzoni, G. L. Chiarotti, S. Scandolo, E. Tosatti, M. Bernasconi, and M. Parrinello. Superionic and Metallic States of Water and Ammonia at Giant Planet Conditions. *Science*, 283:44, January 1999. doi: 10.1126/science.283.5398.44.

J. E. Chambers. A hybrid symplectic integrator that permits close encounters between massive bodies. , 304(4):793–799, April 1999. doi: 10.1046/j.1365-8711.1999.02379.x.

Sylvain Champenois and Alain Vienne. The Role of Secondary Resonances in the Evolution of the Mimas-Tethys System. *Icarus*, 140(1):106–121, July 1999. doi: 10.1006/icar.1999.6115.

R. O. Chancia and M. M. Hedman. Are There Moonlets Near the Uranian α and β Rings? , 152(6):211, December 2016. doi: 10.3847/0004-6256/152/6/211.

R. O. Chancia, M. M. Hedman, S. W. H. Cowley, G. Provan, and S. Y. Ye. Seasonal structures in Saturn's dusty Roche Division correspond to periodicities of the planet's magnetosphere. , 330:230–255, September 2019. doi: 10.1016/j.icarus.2019.04.012.

Robert O. Chancia, Matthew M. Hedman, and Richard G. French. Weighing Uranus' Moon Cressida with the η Ring. , 154(4):153, October 2017. doi: 10.3847/1538-3881/aa880e.

Eugene I. Chiang and Christopher J. Culter. Three-dimensional Dynamics of Narrow Planetary Rings. , 599(1):675–685, December 2003. doi: 10.1086/379151.

N. J. Cooper, C. D. Murray, M. W. Evans, K. Beurle, R. A. Jacobson, and C. C. Porco. Astrometry and dynamics of Anthe (S/2007 S 4), a new satellite of Saturn. , 195:765–777, June 2008. doi: 10.1016/j.icarus.2008.01.006.

Matija Ćuk and Maryame El Moutamid. Three-Body Resonances in the Saturnian System. *arXiv e-prints*, art. arXiv:2201.12313, January 2022.

Matija Ćuk, Douglas P. Hamilton, and Matthew J. Holman. Long-term stability of horseshoe orbits. , 426(4):3051–3056, November 2012. doi: 10.1111/j.1365-2966.2012.21964.x.

Matija Ćuk, Luke Dones, and David Nesvorný. Dynamical Evidence for a Late Formation of Saturn's Moons. *The Astrophysical Journal*, 820(2):97, April 2016. doi: 10.3847/0004-637X/820/2/97.

Matija Ćuk, David A. Minton, Jennifer L. L. Pouplin, and Carlisle Wishard. Evidence for a Past Martian Ring from the Orbital Inclination of Deimos. *ApJL*, 896(2):L28, June 2020. doi: 10.3847/2041-8213/ab974f.

J. N. Cuzzi, G. Filacchione, and E. A. Marouf. The Rings of Saturn. In M. S. Tiscareno and C. D. Murray, editors, *Planetary Ring Systems. Properties, Structure, and Evolution*, pages 51–92. Cambridge, 2018. doi: 10.1017/9781316286791.003.

Merton E. Davies, Patricia G. Rogers, and Tim R. Colvin. A control network of Triton. *J. Geophys. Res.*, 96(E1):15675–15681, August 1991. doi: 10.1029/91JE00976.

Rebekah I. Dawson and Ruth A. Murray-Clay. Giant Planets Orbiting Metal-rich Stars Show Signatures of Planet-Planet Interactions. *The Astrophysical Journal Letters*, 767 (2):L24, April 2013. doi: 10.1088/2041-8205/767/2/L24.

Katherine de Kleer, Francis Nimmo, and Edwin Kite. Variability in Io's Volcanism on Timescales of Periodic Orbital Changes. *Geophysical Research Letters*, 46(12):6327–6332, June 2019. doi: 10.1029/2019GL082691.

I. de Pater, S. Renner, M. R. Showalter, and B. Sicardy. *The Rings of Neptune*, pages 112–124. 2018. doi: 10.1017/9781316286791.005.

Katherine M. Deck, Matthew Payne, and Matthew J. Holman. First-order Resonance Overlap and the Stability of Close Two-planet Systems. *ApJ*, 774(2):129, September 2013. doi: 10.1088/0004-637X/774/2/129.

Stanley F. Dermott and Carl D. Murray. The dynamics of tadpole and horseshoe orbits II. The coorbital satellites of saturn. , 48(1):12–22, October 1981a. doi: 10.1016/0019-1035(81)90148-2.

Stanley F. Dermott and Carl D. Murray. The dynamics of tadpole and horseshoe orbits II. The coorbital satellites of saturn. , 48(1):12–22, October 1981b. doi: 10.1016/0019-1035(81)90148-2.

Stanley F. Dermott, Renu Malhotra, and Carl D. Murray. Dynamics of the Uranian and Saturnian satelite systems: A chaotic route to melting Miranda? , 76(2):295–334, November 1988. doi: 10.1016/0019-1035(88)90074-7.

M. D. Desch, J. E. P. Connerney, and M. L. Kaiser. The rotation period of Uranus. *Nature*, 322(6074):42–43, July 1986. doi: 10.1038/322042a0.

Janosz W. Dewberry, Christopher R. Mankovich, Jim Fuller, Dong Lai, and Wenrui Xu. Constraining Saturn's Interior with Ring Seismology: Effects of Differential Rotation and Stable Stratification. *Planetary Science Journal*, 2(5):198, October 2021. doi: 10.3847/PSJ/ac0e2a.

Martin J. Duncan, Harold F. Levison, and Man Hoi Lee. A Multiple Time Step Symplectic Algorithm for Integrating Close Encounters. *AJ*, 116(4):2067–2077, October 1998. doi: 10.1086/300541.

M. El Moutamid, B. Sicardy, and S. Renner. Coupling between corotation and Lindblad resonances in the presence of secular precession rates. *Celestial Mechanics and Dynamical Astronomy*, 118:235–252, March 2014. doi: 10.1007/s10569-014-9533-z.

M. El Moutamid, B. Sicardy, and S. Renner. Derivation of capture probabilities for the corotation eccentric mean motion resonances. , 469:2380–2386, August 2017. doi: 10.1093/mnras/stx996.

Maryame El Moutamid, Philip D. Nicholson, Richard G. French, Matthew S. Tiscareno, Carl D. Murray, Michael W. Evans, Colleen McGhee French, Matthew M. Hedman, and Joseph A. Burns. How janus' orbital swap affects the edge of saturn's a ring? *Icarus*, 279:125–140, Nov 2016. ISSN 0019-1035. doi: 10.1016/j.icarus.2015.10.025. URL `http://dx.doi.org/10.1016/j.icarus.2015.10.025`.

D. C. Fabrycky. *Non-Keplerian Dynamics of Exoplanets*, pages 217–238. 2010.

Daniel C. Fabrycky, Jack J. Lissauer, Darin Ragozzine, Jason F. Rowe, Jason H. Steffen, Eric Agol, Thomas Barclay, Natalie Batalha, William Borucki, David R. Ciardi, Eric B. Ford, Thomas N. Gautier, John C. Geary, Matthew J. Holman, Jon M. Jenkins, Jie Li, Robert C. Morehead, Robert L. Morris, Avi Shporer, Jeffrey C. Smith, Martin Still, and Jeffrey Van Cleve. Architecture of Kepler's Multi-transiting Systems. II. New Investigations with Twice as Many Candidates. *The Astrophysical Journal*, 790(2):146, August 2014. doi: 10.1088/0004-637X/790/2/146.

Cecile Ferrari and Andre Brahic. Azimuthal Brightness Asymmetries in Planetary Rings.

I. Neptune's Arcs and Naarrow Rings. , 111(1):193–210, September 1994. doi: 10.1006/icar.1994.1140.

J. J. Fortney, M. Ikoma, N. Nettelmann, T. Guillot, and M. S. Marley. Self-consistent Model Atmospheres and the Cooling of the Solar System's Giant Planets. , 729(1):32, March 2011. doi: 10.1088/0004-637X/729/1/32.

Jonathan J. Fortney and Nadine Nettelmann. The Interior Structure, Composition, and Evolution of Giant Planets. *Space Science Reviews*, 152(1-4):423–447, May 2010. doi: 10.1007/s11214-009-9582-x.

Dietmar W. Foryta and Bruno Sicardy. The Dynamics of the Neptunian ADAMS Ring's Arcs. , 123(1):129–167, September 1996. doi: 10.1006/icar.1996.0146.

Martin French and Nadine Nettelmann. Viscosity and Prandtl Number of Warm Dense Water as in Ice Giant Planets. , 881(1):81, August 2019. doi: 10.3847/1538-4357/ab2d21.

R. G. French and P. D. Nicholson. Edge waves and librations in the Uranus epsilon ring. In *American Astronomical Society Meeting Abstracts #186*, volume 186 of *American Astronomical Society Meeting Abstracts*, page 33.02, May 1995.

R. G. French, W. Bridges, M. Hedman, P. Nicholson, C. Mankovich, and C. McGhee-French. A panoply of waves in Saturn's C ring driven by internal planetary oscillations. In *AAS/Division for Planetary Sciences Meeting Abstracts*, volume 52 of *AAS/Division for Planetary Sciences Meeting Abstracts*, page 513.06, October 2020.

Richard G. French, Philip D. Nicholson, Carolyn C. Porco, and Essam A. Marouf. *Dynamics and structure of the Uranian rings.*, pages 327–409. University of Arizona Press, 1991.

Richard G. French, Philip D. Nicholson, Mathew M. Hedman, Joseph M. Hahn, Colleen A. McGhee-French, Joshua E. Colwell, Essam A. Marouf, and Nicole J. Rappaport. Deciphering the embedded wave in Saturn's Maxwell ringlet. , 279:62–77, Nov 2016. doi: 10.1016/j.icarus.2015.08.020.

Richard G. French, Colleen A. McGhee-French, Philip D. Nicholson, and Mathew M. Hedman. Kronoseismology III: Waves in Saturn's inner C ring. *Icarus*, 319:599–626, February 2019. doi: 10.1016/j.icarus.2018.10.013.

Richard G. French, Bill Bridges, Matthew M. Hedman, Philip D. Nicholson, Christopher Mankovich, and Colleen A. McGhee-French. Kronoseismology V: A panoply of waves in Saturn's C ring driven by high-order internal planetary oscillations. , 370:114660, December 2021. doi: 10.1016/j.icarus.2021.114660.

A. James Friedson. Ice giant seismology: prospecting for normal modes. *Philosophical Transactions of the Royal Society of London Series A*, 378(2187):20190475, December 2020. doi: 10.1098/rsta.2019.0475.

Jim Fuller. Saturn ring seismology: Evidence for stable stratification in the deep interior of Saturn. , 242:283–296, November 2014. doi: 10.1016/j.icarus.2014.08.006.

Jim Fuller, Jing Luan, and Eliot Quataert. Resonance locking as the source of rapid tidal migration in the Jupiter and Saturn moon systems. *Monthly Notices of the Royal Astronomical Society*, 458(4):3867–3879, June 2016. doi: 10.1093/mnras/stw609.

B. Funk, G. Wuchterl, R. Schwarz, E. Pilat-Lohinger, and S. Eggl. The stability of ultra-compact planetary systems. *A&A*, 516:A82, June 2010. doi: 10.1051/0004-6361/200912698.

D. M. Gaslac Gallardo, S. M. Giuliatti Winter, G. Madeira, and M. A. Muñoz-Gutiérrez. Analysing the region of the rings and small satellites of Neptune. , 365(1):5, January 2020. doi: 10.1007/s10509-019-3717-7.

P. Gaulme, F. X. Schmider, T. Guillot, and J. Gay. Evidence of Jovian acoustic global modes. In *EPSC-DPS Joint Meeting 2011*, volume 2011, page 256, Oct 2011.

Patrick Gaulme. Seismology of Giant Planets: General Overview and Results from the Kepler K2 Observations of Neptune. In *European Physical Journal Web of Conferences*, volume 160 of *European Physical Journal Web of Conferences*, page 05012, Oct 2017. doi: 10.1051/epjconf/201716005012.

S. V. Gavrilov and V. N. Zharkov. Love Numbers of the Giant Planets. *Icarus*, 32(4): 443–449, December 1977. doi: 10.1016/0019-1035(77)90015-X.

S. M. Giuliatti Winter, G. Madeira, and R. Sfair. Neptune's ring arcs confined by coorbital satellites: dust orbital evolution through solar radiation. *MNRAS*, 496(1):590–597, July 2020. doi: 10.1093/mnras/staa1519.

C. A. Giuppone, P. Benítez-Llambay, and C. Beaugé. Origin and detectability of co-orbital planets from radial velocity data. , 421(1):356–368, March 2012. doi: 10.1111/j.1365-2966.2011.20310.x.

Brett Gladman. Dynamics of Systems of Two Close Planets. *Icarus*, 106(1):247–263, November 1993. doi: 10.1006/icar.1993.1169.

P. Goldreich and S. Tremaine. The excitation of density waves at the Lindblad and corotation resonances by an external potential. , 233:857–871, November 1979. doi: 10.1086/157448.

P. Goldreich and S. Tremaine. Disk-satellite interactions. *The Astrophysical Journal*, 241: 425–441, October 1980. doi: 10.1086/158356.

P. Goldreich and S. D. Tremaine. The formation of the Cassini division in Saturn's rings. , 34(2):240–253, May 1978. doi: 10.1016/0019-1035(78)90165-3.

P. Goldreich, S. Tremaine, and N. Borderies. Towards a theory for Neptune's arc rings. , 92:490–494, August 1986. doi: 10.1086/114178.

Peter Goldreich and Carolyn C. Porco. Shepherding of the Uranian Rings. II. Dynamics. , 93:730, March 1987. doi: 10.1086/114355.

R. S. Gomes. Orbital Evolution in Resonance Lock.I.The Restricted 3-Body Problem. *AJ*, 114:2166, November 1997. doi: 10.1086/118637.

R. S. Gomes. Orbital Evolution in Resonance Lock. II. Two Mutually Perturbing Bodies. *AJ*, 116(2):997–1005, August 1998. doi: 10.1086/300445.

Agueda Paula Granados Contreras and Aaron Boley. The formation of co-orbital planets and their resulting transit signatures. In *AAS/Division of Dynamical Astronomy Meeting*, AAS/Division of Dynamical Astronomy Meeting, page 202.07, April 2018.

M Hedman, J Burns, M Showalter, C Porco, P Nicholson, A Bosh, M Tiscareno, R Brown, B Buratti, and K Baines. Saturn's dynamic d ring. *Icarus*, 188(1): 89–107, May 2007a. ISSN 0019-1035. doi: 10.1016/j.icarus.2006.11.017. URL `http://dx.doi.org/10.1016/j.icarus.2006.11.017`.

M. M. Hedman. *An Introduction to Planetary Ring Dynamics*, pages 30–48. February 2018. doi: 10.1017/9781316286791.002.

M. M. Hedman and P. D. Nicholson. Kronoseismology: Using Density Waves in Saturn's C Ring to Probe the Planet's Interior. *The Astronomical Journal*, 146(1):12, July 2013. doi: 10.1088/0004-6256/146/1/12.

M. M. Hedman, J. A. Burns, M. S. Tiscareno, C. C. Porco, G. H. Jones, E. Roussos, N. Krupp, C. Paranicas, and S. Kempf. The source of saturn's g ring. *Science*, 317 (5838):653–656, Aug 2007b. ISSN 1095-9203. doi: 10.1126/science.1143964. URL `http://dx.doi.org/10.1126/science.1143964`.

M. M. Hedman, J. A. Burns, M. S. Tiscareno, C. C. Porco, G. H. Jones, E. Roussos, N. Krupp, C. Paranicas, and S. Kempf. The source of saturn's g ring. *Science*, 317(5838):653–656, Aug 2007c. ISSN 1095-9203. doi: 10.1126/science.1143964. URL `http://dx.doi.org/10.1126/science.1143964`.

M. M. Hedman, J. A. Burns, M. S. Tiscareno, and C. C. Porco. Organizing some very tenuous things: Resonant structures in Saturn's faint rings. , 202(1):260–279, July 2009a. doi: 10.1016/j.icarus.2009.02.016.

M. M. Hedman, C. D. Murray, N. J. Cooper, M. S. Tiscareno, K. Beurle, M. W. Evans, and J. A. Burns. Three tenuous rings/arcs for three tiny moons. , 199:378–386, February 2009b. doi: 10.1016/j.icarus.2008.11.001.

M. M. Hedman, N. J. Cooper, C. D. Murray, K. Beurle, M. W. Evans, M. S. Tiscareno, and J. A. Burns. Aegaeon (Saturn LIII), a G-ring object. , 207:433–447, May 2010. doi: 10.1016/j.icarus.2009.10.024.

M. M. Hedman, P. D. Nicholson, and R. G. French. Kronoseismology. IV. Six Previously Unidentified Waves in Saturn's Middle C Ring. *The Astronomical Journal*, 157(1):18, January 2019. doi: 10.3847/1538-3881/aaf0a6.

M. M. Hedman, P. D. Nicholson, M. El Moutamid, and S. Smotherman. Kronoseismology VI: Reading the recent history of Saturn's gravity field in its rings. *arXiv e-prints*, art. arXiv:2201.08489, January 2022.

Mathew Hedman and Bill Bridges. Changes in a Dusty Ringlet in the Cassini Division after 2010. *The Planetary Science Journal*, 1(2):43, September 2020. doi: 10.3847/PSJ/abacc7.

Matthew Hedman and Rob Chancia. Uranus's Hidden Narrow Rings. , 2(3):107, June 2021. doi: 10.3847/PSJ/abfdb6.

M.M. Hedman. Bright clumps in the d68 ringlet near the end of the cassini mission. *Icarus*, 323:62–75, May 2019. ISSN 0019-1035. doi: 10.1016/j.icarus.2019.01.007. URL `http://dx.doi.org/10.1016/j.icarus.2019.01.007`.

M.M. Hedman, J.A. Burt, J.A. Burns, and M.R. Showalter. Non-circular features in saturn's d ring: D68. *Icarus*, 233:147–162, May 2014. ISSN 0019-1035. doi: 10.1016/j.icarus.2014.01.022. URL `http://dx.doi.org/10.1016/j.icarus.2014.01.022`.

Ravit Helled and Jonathan J. Fortney. The Interiors of Uranus and Neptune: Current Understanding and Open Questions. *arXiv e-prints*, art. arXiv:2007.10783, July 2020.

Ravit Helled, John D. Anderson, and Gerald Schubert. Uranus and Neptune: Shape and rotation. , 210(1):446–454, November 2010. doi: 10.1016/j.icarus.2010.06.037.

Ravit Helled, Eli Galanti, and Yohai Kaspi. Saturn's fast spin determined from its gravitational field and oblateness. *Nature*, 520(7546):202–204, April 2015. doi: 10.1038/nature14278.

Ravit Helled, Nadine Nettelmann, and Tristan Guillot. Uranus and Neptune: Origin, Evolution and Internal Structure. , 216(3):38, March 2020. doi: 10.1007/s11214-020-00660-3.

Andrew J. Hesselbrock and David A. Minton. An ongoing satellite-ring cycle of Mars and the origins of Phobos and Deimos. *Nature Geoscience*, 10(4):266–269, March 2017. doi: 10.1038/ngeo2916.

Andrew J. Hesselbrock and David A. Minton. Three Dynamical Evolution Regimes for Coupled Ring-satellite Systems and Implications for the Formation of the Uranian Satellite Miranda. *The Astronomical Journal*, 157(1):30, January 2019. doi: 10.3847/1538-3881/aaf23a.

L. J. Horn, P. A. Yanamandra-Fisher, L. W. Esposito, and A. L. Lane. Physical properties of Uranian delta ring from a possible density wave. , 76(3):485–492, December 1988. doi: 10.1016/0019-1035(88)90016-4.

W. B. Hubbard, A. Brahic, P. Bouchet, L. R. Elicer, R. Haefner, J. Manfroid, F. Roques, B. Sicardy, and F. Vilas. Occultation detection of a Neptune ring segment. In *16th Lunar and Planetary Science Conference*, volume 559, page 35, Jan 1985.

W. B. Hubbard, A. Brahic, B. Sicardy, L. R. Elicer, F. Roques, and F. Vilas. Occultation detection of a neptunian ring-like arc. *Nature*, 319(6055):636–640, February 1986. doi: 10.1038/319636a0.

Naireen Hussain and Daniel Tamayo. Fundamental limits from chaos on instability time predictions in compact planetary systems. *MNRAS*, 491(4):5258–5267, February 2020. doi: 10.1093/mnras/stz3402.

Benjamin Idini and David J. Stevenson. Dynamical Tides in Jupiter as Revealed by Juno. *PSJ*, 2(2):69, April 2021. doi: 10.3847/PSJ/abe715.

L. Iess, B. Militzer, Y. Kaspi, P. Nicholson, D. Durante, P. Racioppa, A. Anabtawi, E. Galanti, W. Hubbard, M. J. Mariani, P. Tortora, S. Wahl, and M. Zannoni. Measurement and implications of Saturn's gravity field and ring mass. *Science*, 364(6445): aat2965, June 2019. doi: 10.1126/science.aat2965.

R. A. Jacobson. The Orbits of the Inner Uranian Satellites from Hubble Space Telescope and Voyager 2 Observations. , 115(3):1195–1199, March 1998. doi: 10.1086/300263.

R. A. Jacobson. The Orbits of the Neptunian Satellites and the Orientation of the Pole of Neptune. , 137(5):4322–4329, May 2009. doi: 10.1088/0004-6256/137/5/4322.

R. A. Jacobson. Ephemerides of the Major Saturnian Satellites–Current Status, Future Prospects. In *AAS/Division of Dynamical Astronomy Meeting #41*, volume 42 of *Bulletin of the American Astronomical Society*, page 933, May 2010.

R. A. Jacobson. The Orbits of the Uranian Satellites and Rings, the Gravity Field of the Uranian System, and the Orientation of the Pole of Uranus. , 148(5):76, November 2014. doi: 10.1088/0004-6256/148/5/76.

R. A. Jacobson, P. G. Antreasian, J. J. Bordi, K. E. Criddle, R. Ionasescu, J. B. Jones, R. A. Mackenzie, M. C. Meek, D. Parcher, F. J. Pelletier, W. M. Owen, Jr., D. C. Roth, I. M. Roundhill, and J. R. Stauch. The Gravity Field of the Saturnian System from Satellite Observations and Spacecraft Tracking Data. , 132:2520–2526, December 2006. doi: 10.1086/508812.

R. A. Jacobson, J. Spitale, C. C. Porco, K. Beurle, N. J. Cooper, M. W. Evans, and C. D. Murray. Revised Orbits of Saturn's Small Inner Satellites. , 135(1):261–263, January 2008. doi: 10.1088/0004-6256/135/1/261.

Lisa Kaltenegger and Wesley A. Traub. Transits of Earth-like Planets. , 698(1):519–527, June 2009. doi: 10.1088/0004-637X/698/1/519.

Murat Kaplan and Sergen Cengiz. Horseshoe Co-orbitals of Earth: Current Population and New Candidates. *arXiv e-prints*, art. arXiv:2006.14451, June 2020.

Erich Karkoschka. Voyager's Eleventh Discovery of a Satellite of Uranus and Photometry and the First Size Measurements of Nine Satellites. , 151(1):69–77, May 2001. doi: 10.1006/icar.2001.6597.

Erich Karkoschka. Sizes, shapes, and albedos of the inner satellites of Neptune. , 162(2): 400–407, April 2003. doi: 10.1016/S0019-1035(03)00002-2.

Yohai Kaspi, Adam P. Showman, William B. Hubbard, Oded Aharonson, and Ravit Helled. Atmospheric confinement of jet streams on Uranus and Neptune. *Nature*, 497(7449):344–347, May 2013. doi: 10.1038/nature12131.

A. J. Kliore, I. R. Patel, G. F. Lindal, D. N. Sweetnam, H. B. Hotz, J. H. Waite, and T. McDonough. Structure of the Ionosphere and Atmosphere of Saturn From Pioneer 11 Saturn Radio Occultation. *J. Geophys. Res.*, 85(A11):5857–5870, November 1980. doi: 10.1029/JA085iA11p05857.

M. D. Knudson, M. P. Desjarlais, R. W. Lemke, T. R. Mattsson, M. French, N. Nettelmann, and R. Redmer. Probing the Interiors of the Ice Giants: Shock Compression of Water to 700 GPa and 3.8g/cm^3. , 108(9):091102, March 2012. doi: 10.1103/PhysRevLett.108.091102.

Job Kozhamthadam. *The Discovery of Kepler's Laws: The Interaction of Science, Philosophy, and Religion.* University of Notre Dame Press, 1994.

Valéry Lainey. Quantification of tidal parameters from Solar System data. *CMDA*, 126 (1-3):145–156, November 2016. doi: 10.1007/s10569-016-9695-y.

Valéry Lainey, Özgür Karatekin, Josselin Desmars, Sébastien Charnoz, Jean-Eudes Arlot, Nicolai Emelyanov, Christophe Le Poncin-Lafitte, Stéphane Mathis, Françoise Remus, Gabriel Tobie, and Jean-Paul Zahn. Strong Tidal Dissipation in Saturn and Constraints on Enceladus' Thermal State from Astrometry. , 752(1):14, June 2012. doi: 10.1088/0004-637X/752/1/14.

Valéry Lainey, Robert A. Jacobson, Radwan Tajeddine, Nicholas J. Cooper, Carl Murray, Vincent Robert, Gabriel Tobie, Tristan Guillot, Stéphane Mathis, Françoise Remus, Josselin Desmars, Jean-Eudes Arlot, Jean-Pierre De Cuyper, Véronique Dehant, Dan Pascu, William Thuillot, Christophe Le Poncin-Lafitte, and Jean-Paul Zahn. New constraints on Saturn's interior from Cassini astrometric data. *Icarus*, 281:286–296, January 2017. doi: 10.1016/j.icarus.2016.07.014.

Valéry Lainey, Luis Gomez Casajus, Jim Fuller, Marco Zannoni, Paolo Tortora, Nicholas

Cooper, Carl Murray, Dario Modenini, Ryan S. Park, Vincent Robert, and Qingfeng Zhang. Resonance locking in giant planets indicated by the rapid orbital expansion of Titan. *Nature Astronomy*, 4:1053–1058, June 2020. doi: 10.1038/s41550-020-1120-5.

Gregory Laughlin and John E. Chambers. Extrasolar Trojans: The Viability and Detectability of Planets in the 1:1 Resonance. , 124(1):592–600, July 2002. doi: 10.1086/341173.

P. Ledoux. The Nonradial Oscillations of Gaseous Stars and the Problem of Beta Canis Majoris. , 114:373, November 1951. doi: 10.1086/145477.

A. Leleu, P. Robutel, A. C. M. Correia, and J. Lillo-Box. Detection of co-orbital planets by combining transit and radial-velocity measurements. *A&A*, 599:L7, March 2017. doi: 10.1051/0004-6361/201630073.

Adrien Leleu, Philippe Robutel, and Alexandre C. M. Correia. Detectability of quasi-circular co-orbital planets. Application to the radial velocity technique. *A&A*, 581:A128, September 2015. doi: 10.1051/0004-6361/201526175.

J. J. Lissauer. Shepherding model for Neptune's arc ring. *Nature*, 318(6046):544–545, December 1985. doi: 10.1038/318544a0.

Jack J. Lissauer and Sacha Gavino. Orbital stability of compact three-planet systems, I: Dependence of system lifetimes on initial orbital separations and longitudes. *Icarus*, 364: 114470, August 2021. doi: 10.1016/j.icarus.2021.114470.

Jing Luan. Special mean motion resonance pairs: Mimas-Tethys and Titan-Hyperion. *arXiv e-prints*, art. arXiv:1410.2648, October 2014.

G. Madeira, S. M. Giuliatti Winter, T. Ribeiro, and O. C. Winter. Dynamics around non-spherical symmetric bodies - I. The case of a spherical body with mass anomaly. , 510 (1):1450–1469, February 2022. doi: 10.1093/mnras/stab3552.

Gustavo Madeira, R Sfair, D C Mourão, and S M Giuliatti Winter. Production and fate of the g ring arc particles due to aegaeon (saturn liii). *Monthly Notices of the Royal Astronomical Society*, 475(4):5474–5479, Jan 2018. ISSN 1365-2966. doi: 10.1093/mnras/sty179. URL `http://dx.doi.org/10.1093/mnras/sty179`.

J. Manfroid, R. Haefner, and P. Bouchet. New evidence for a ring around Neptune. *A&A*, 157(1):L3–L5, Mar 1986.

Christopher Mankovich, Mark S. Marley, Jonathan J. Fortney, and Naor Movshovitz. Cassini Ring Seismology as a Probe of Saturn's Interior. I. Rigid Rotation. , 871(1): 1, January 2019. doi: 10.3847/1538-4357/aaf798.

Christopher R. Mankovich and Jim Fuller. A diffuse core in Saturn revealed by ring seismology. *Nature Astronomy*, August 2021. doi: 10.1038/s41550-021-01448-3.

Steve Markham and Dave Stevenson. Excitation mechanisms for Jovian seismic modes. , 306:200–213, May 2018. doi: 10.1016/j.icarus.2018.02.015.

Steve Markham, Daniele Durante, Luciano Iess, and Dave Stevenson. Possible Evidence of p-modes in Cassini Measurements of Saturn's Gravity Field. , 1(2):27, September 2020. doi: 10.3847/PSJ/ab9f21.

Mark S. Marley. Nonradial oscillations of Saturn. , 94(2):420–435, Dec 1991. doi: 10.1016/0019-1035(91)90239-P.

Mark S. Marley. Saturn ring seismology: Looking beyond first order resonances. , 234: 194–199, May 2014. doi: 10.1016/j.icarus.2014.02.002.

Mark S. Marley and Carolyn C. Porco. Planetary Acoustic Mode Seismology: Saturn's Rings. , 106(2):508–524, December 1993. doi: 10.1006/icar.1993.1189.

Mark S. Marley, W.B. Hubbard, and C.C. Porco. Do Uranian acoustic oscillations shepherd the rings? *Uranus Colloquium Abstracts*, 1988.

Mark Scott Marley. *Nonradial Oscillations of Saturn: Implications for Ring System Structure.* PhD thesis, Arizona Univ., Tucson., January 1990.

Isamu Matsuyama, Mikael Beuthe, Hamish C. F. C. Hay, Francis Nimmo, and Shunichi Kamata. Ocean tidal heating in icy satellites with solid shells. *Icarus*, 312:208–230, September 2018. doi: 10.1016/j.icarus.2018.04.013.

S. Mazevet, A. Licari, G. Chabrier, and A. Y. Potekhin. Ab initio based equation of state of dense water for planetary and exoplanetary modeling. *A&A*, 621:A128, January 2019. doi: 10.1051/0004-6361/201833963.

Jennifer Meyer and Jack Wisdom. Tidal evolution of Mimas, Enceladus, and Dione. , 193 (1):213–223, January 2008. doi: 10.1016/j.icarus.2007.09.008.

Y. Miguel, T. Guillot, and L. Fayon. Jupiter internal structure: the effect of different equations of state. *A&A*, 596:A114, December 2016. doi: 10.1051/0004-6361/201629732.

B. Militzer and W. B. Hubbard. Ab Initio Equation of State for Hydrogen-Helium Mixtures with Recalibration of the Giant-planet Mass-Radius Relation. , 774(2):148, September 2013. doi: 10.1088/0004-637X/774/2/148.

Marius Millot, Sebastien Hamel, J. Ryan Rygg, Peter M. Celliers, Gilbert W. Collins, Federica Coppari, Dayne E. Fratanduono, Raymond Jeanloz, Damian C. Swift, and Jon H. Eggert. Experimental evidence for superionic water ice using shock compression. *Nature Physics*, 14(3):297–302, February 2018. doi: 10.1038/s41567-017-0017-4.

Marius Millot, Federica Coppari, J. Ryan Rygg, Antonio Correa Barrios, Sebastien Hamel, Damian C. Swift, and Jon H. Eggert. Nanosecond X-ray diffraction of shock-compressed superionic water ice. *Nature*, 569(7755):251–255, May 2019. doi: 10.1038/s41586-019-1114-6.

David Minton, Carlisle Wishard, Jennifer Pouplin, Jacob Elliott, and Dana Singh. Swiftest: Modernizing a classic n-body integrator with Object Oriented Fortran. In *DPS Meeting*, volume 53 of *AAS*, page 411.03, October 2021.

M. A. Muñoz-Gutiérrez and S. Giuliatti Winter. Long-term evolution and stability of Saturnian small satellites: Aegaeon, Methone, Anthe and Pallene. , 470:3750–3764, September 2017. doi: 10.1093/mnras/stx1537.

Marco A. Muñoz-Gutiérrez, A. P. Granados Contreras, Gustavo Madeira, Joseph A. A'Hearn, and Silvia Giuliatti Winter. Long-term dynamical evolution of pallene (Saturn XXXIII) and its diffuse, dusty ring. , December 2021. doi: 10.1093/mnras/stab3627.

Simon Müller and Ravit Helled. Synthetic evolution tracks of giant planets. *Monthly Notices of the Royal Astronomical Society*, 507(2):2094–2102, October 2021. doi: 10.1093/mnras/stab2250.

C. D. Murray and S. F. Dermott. *Solar system dynamics.* 1999.

Carl D. Murray and Robert P. Thompson. Orbits of shepherd satellites deduced from the structure of the rings of Uranus. *Nature*, 348(6301):499–502, December 1990. doi: 10.1038/348499a0.

Ayano Nakajima, Shigeru Ida, and Yota Ishigaki. Orbital evolution of Saturn's satellites due to the interaction between the moons and the massive rings. *Astronomy & Astrophysics*, 640:L15, August 2020. doi: 10.1051/0004-6361/202038743.

F. Namouni and M. H. M. Morais. Resonance capture at arbitrary inclination - II. Effect of the radial drift rate. *MNRAS*, 467(3):2673–2683, May 2017. doi: 10.1093/mnras/stx290.

Fathi Namouni and Carolyn Porco. The confinement of Neptune's ring arcs by the moon Galatea. *Nature*, 417(6884):45–47, May 2002. doi: 10.1038/417045a.

N. Nettelmann. Low- and high-order gravitational harmonics of rigidly rotating Jupiter. *A&A*, 606:A139, October 2017. doi: 10.1051/0004-6361/201731550.

Marc Neveu and Alyssa R. Rhoden. Evolution of Saturn's mid-sized moons. *Nature Astronomy*, 3:543–552, April 2019. doi: 10.1038/s41550-019-0726-y.

Isaac Newton. *Philosophiae Naturalis Principia Mathematica.* 1687. doi: 10.3931/e-rara-440.

P. D. Nicholson, I. de Pater, R. G. French, and M. R. Showalter. *The Rings of Uranus*, pages 93–111. Cambridge, 2018. doi: 10.1017/9781316286791.004.

Philip D. Nicholson, Richard G. French, Colleen A. McGhee-French, Matthew M. Hedman, Essam A. Marouf, Joshua E. Colwell, Katherine Lonergan, and Talia Sepersky. Noncircular features in Saturn's rings II: The C ring. , 241:373–396, October 2014. doi: 10.1016/j.icarus.2014.06.024.

J. L. Ortiz, R. Duffard, N. Pinilla-Alonso, A. Alvarez-Candal, P. Santos-Sanz, N. Morales, E. Fernández-Valenzuela, J. Licandro, A. Campo Bagatin, and A. Thirouin. Possible ring material around centaur (2060) Chiron. *A&A*, 576:A18, April 2015. doi: 10.1051/0004-6361/201424461.

J. L. Ortiz, P. Santos-Sanz, B. Sicardy, G. Benedetti-Rossi, D. Bérard, N. Morales, R. Duffard, F. Braga-Ribas, U. Hopp, C. Ries, V. Nascimbeni, F. Marzari, V. Granata, A. Pál, C. Kiss, T. Pribulla, R. Komžík, K. Hornoch, P. Pravec, P. Bacci, M. Maestripieri, L. Nerli, L. Mazzei, M. Bachini, F. Martinelli, G. Succi, F. Ciabattari, H. Mikuz, A. Carbognani, B. Gaehrken, S. Mottola, S. Hellmich, F. L. Rommel, E. Fernández-Valenzuela, A. Campo Bagatin, S. Cikota, A. Cikota, J. Lecacheux, R. Vieira-Martins, J. I. B. Camargo, M. Assafin, F. Colas, R. Behrend, J. Desmars, E. Meza, A. Alvarez-Candal, W. Beisker, A. R. Gomes-Junior, B. E. Morgado, F. Roques, F. Vachier, J. Berthier, T. G. Mueller, J. M. Madiedo, O. Unsalan, E. Sonbas, N. Karaman, O. Erece, D. T. Koseoglu, T. Ozisik, S. Kalkan, Y. Guney, M. S. Niaei, O. Satir, C. Yesilyaprak, C. Puskullu, A. Kabas, O. Demircan, J. Alikakos, V. Charmandaris, G. Leto, J. Ohlert, J. M. Christille, R. Szakáts, A. Takácsné Farkas, E. Varga-Verebélyi, G. Marton, A. Marciniak, P. Bartczak, T. Santana-Ros, M. Butkiewicz-Bak, G. Dudziński, V. Alí-Lagoa, K. Gazeas, L. Tzouganatos, N. Paschalis, V. Tsamis, A. Sánchez-Lavega, S. Pérez-Hoyos, R. Hueso, J. C. Guirado, V. Peris, and R. Iglesias-Marzoa. The size, shape, density and ring of the dwarf planet Haumea from a stellar occultation. *Nature*, 550(7675):219–223, October 2017. doi: 10.1038/nature24051.

R. S. Park, K. de Kleer, A. McEwen, C. J. Bierson, A. G. Davies, D. DellaGiustina, A. I. Ermakov, J. Fuller, C. Hamilton, C. Harris, H. Hay, R. Jacobson, J. Keane, L. Kestay, K. Khurana, K. Kirby, V. Lainey, I. Matsuyama, C. McCarthy, F. Nimmo, M. Panning, A. Pommier, J. Rathbun, G. Steinbrügge, D. Stevenson, V. C. Tsai, and E. Turtle. Tidal Heating: Lessons from Io and the Jovian System (Report from the KISS Workshop). Lunar and Planetary Science Conference, page 1925, March 2019.

Bill Paxton, Lars Bildsten, Aaron Dotter, Falk Herwig, Pierre Lesaffre, and Frank Timmes.

Modules for Experiments in Stellar Astrophysics (MESA). *The Astrophysical Journal Supplement*, 192(1):3, January 2011. doi: 10.1088/0067-0049/192/1/3.

Antoine C. Petit, Gabriele Pichierri, Melvyn B. Davies, and Anders Johansen. The path to instability in compact multi-planetary systems. *A&A*, 641:A176, September 2020. doi: 10.1051/0004-6361/202038764.

Morris Podolak, Ravit Helled, and Gerald Schubert. Effect of non-adiabatic thermal profiles on the inferred compositions of Uranus and Neptune. , 487(2):2653–2664, August 2019. doi: 10.1093/mnras/stz1467.

P. Pokorný and M. Kuchner. Co-orbital Asteroids as the Source of Venus's Zodiacal Dust Ring. *The Astrophysical Journal Letters*, 873:L16, March 2019. doi: 10.3847/2041-8213/ab0827.

C. Porco, P. D. Nicholson, N. Borderies, G. E. Danielson, P. Goldreich, J. B. Holberg, and A. L. Lane. The eccentric Saturnian ringlets at 1.29 R_s and 1.45 R_s. , 60(1):1–16, October 1984. doi: 10.1016/0019-1035(84)90134-9.

C. C. Porco. Narrow rings: Observations and theory. *Advances in Space Research*, 10(1): 221–229, January 1990. doi: 10.1016/0273-1177(90)90107-B.

C. C. Porco and P. Goldreich. Shepherding of the Uranian Rings. I. Kinematics. , 93:724, March 1987. doi: 10.1086/114354.

C. C. Porco, P. D. Nicholson, J. N. Cuzzi, J. J. Lissauer, and L. W. Esposito. Neptune's ring system. In D. P. Cruikshank, M. S. Matthews, and A. M. Schumann, editors, *Neptune and Triton*, pages 703–804, 1995.

Carolyn C. Porco. An Explanation for Neptune's Ring Arcs. *Science*, 253(5023):995–1001, August 1991. doi: 10.1126/science.253.5023.995.

Alice C. Quillen. Reducing the probability of capture into resonance. *MNRAS*, 365(4): 1367–1382, February 2006. doi: 10.1111/j.1365-2966.2005.09826.x.

Alice C. Quillen. Three-body resonance overlap in closely spaced multiple-planet systems. *MNRAS*, 418(2):1043–1054, December 2011. doi: 10.1111/j.1365-2966.2011.19555.x.

A. Reiners, M. Zechmeister, J. A. Caballero, I. Ribas, J. C. Morales, S. V. Jeffers, P. Schöfer, L. Tal-Or, A. Quirrenbach, P. J. Amado, A. Kaminski, W. Seifert, M. Abril, J. Aceituno, F. J. Alonso-Floriano, M. Ammler-von Eiff, R. Antona, G. Anglada-Escudé, H. Anwand-Heerwart, B. Arroyo-Torres, M. Azzaro, D. Baroch, D. Barrado, F. F. Bauer, S. Becerril, V. J. S. Béjar, D. Benítez, Z. M. BerdinasÌ, G. Bergond, M. Blümcke, M. Brinkmöller, C. del Burgo, J. Cano, M. C. Cárdenas Vázquez, E. Casal, C. Cifuentes, A. Claret, J. Colomé, M. Cortés-Contreras, S. Czesla, E. Díez-Alonso, S. Dreizler, C. Feiz, M. Fernández, I. M. Ferro, B. Fuhrmeister, D. Galadí-Enríquez, A. Garcia-Piquer, M. L. García Vargas, L. Gesa, V. Gómez Galera, J. I. González Hernández, R. González-Peinado, U. Grözinger, S. Grohnert, J. Guàrdia, E. W. Guenther, A. Guijarro, E. de Guindos, J. Gutiérrez-Soto, H. J. Hagen, A. P. Hatzes, P. H. Hauschildt, R. P. Hedrosa, J. Helmling, Th. Henning, I. Hermelo, R. Hernández Arabí, L. Hernández Castaño, F. Hernández Hernando, E. Herrero, A. Huber, P. Huke, E. N. Johnson, E. de Juan, M. Kim, R. Klein, J. Klüter, A. Klutsch, M. Kürster, M. Lafarga, A. Lamert, M. Lampón, L. M. Lara, W. Laun, U. Lemke, R. Lenzen, R. Launhardt, M. López del Fresno, J. López-González, M. López-Puertas, J. F. López Salas, J. López-Santiago, R. Luque, H. Magán Madinabeitia, U. Mall, L. Mancini, H. Mandel, E. Marfil, J. A. Marín Molina, D. Maroto Fernández, E. L. Martín, S. Martín-Ruiz, C. J. Marvin, R. J. Mathar, E. Mirabet, D. Montes, M. E. Moreno-Raya, A. Moya, R. Mundt, E. Nagel, V. Naranjo, L. Nortmann, G. Nowak, A. Ofir, R. Oreiro, E. Pallé, J. Panduro, J. Pascual, V. M. Passegger, A. Pavlov, S. Pedraz, A. Pérez-Calpena, D. Pérez Medialdea, M. Perger, M. A. C. Perryman, M. Pluto, O. Rabaza, A. Ramón, R. Rebolo, P. Redondo, S. Reffert, S. Reinhart, P. Rhode, H. W. Rix, F. Rodler, E. Rodríguez, C. Rodríguez-López, A. Rodríguez Trinidad, R. R. Rohloff, A. Rosich, S. Sadegi, E. Sánchez-Blanco, M. A. Sánchez Carrasco, A. Sánchez-López, J. Sanz-Forcada, P. Sarkis, L. F. Sarmiento, S. Schäfer, J. H. M. M. Schmitt, J. Schiller, A. Schweitzer, E. Solano, O. Stahl, J. B. P. Strachan, J. Stürmer, J. C. Suárez, H. M. Tabernero, M. Tala, T. Trifonov, S. M. Tulloch, R. G. Ulbrich, G. Veredas, J. I. Vico Linares, F. Vilardell, K. Wagner, J. Winkler, V. Wolthoff, W. Xu, F. Yan, and M. R. Zapatero Osorio. The CARMENES search for exoplanets around M dwarfs. High-resolution optical and near-infrared spectroscopy of 324 survey stars. *Astronomy & Astrophysics*, 612:A49, April 2018. doi: 10.1051/0004-6361/201732054.

S. Renner and B. Sicardy. Use of the Geometric Elements in Numerical Simulations. *Celestial Mechanics and Dynamical Astronomy*, 94:237–248, February 2006. doi: 10.1007/s10569-005-5533-3.

S. Renner, B. Sicardy, D. Souami, B. Carry, and C. Dumas. Neptune's ring arcs: VLT/-NACO near-infrared observations and a model to explain their stability. *A&A*, 563:A133, March 2014. doi: 10.1051/0004-6361/201321910.

Stéfan Renner and Bruno Sicardy. Stationary configurations for co-orbital satellites with small arbitrary masses. *Celestial Mechanics and Dynamical Astronomy*, 88(4): 397–414, Apr 2004. ISSN 0923-2958. doi: 10.1023/b:cele.0000023420.80881.67. URL `http://dx.doi.org/10.1023/B:CELE.0000023420.80881.67`.

Alyssa Rose Rhoden and Matthew E. Walker. The case for an ocean-bearing Mimas from tidal heating analysis. *Icarus*, 376:114872, April 2022. doi: 10.1016/j.icarus.2021.114872.

Th. Roatsch, R. Jaumann, K. Stephan, and P. C. Thomas. *Cartographic Mapping of the Icy Satellites Using ISS and VIMS Data*, page 763. 2009. doi: 10.1007/978-1-4020-9217-$6_2$4.

J. H. Roberts and A. M. Stickle. Break the World's Shell: An Impact on Enceladus: Bringing the Ocean to the Surface. In *Lunar and Planetary Science Conference*, Lunar and Planetary Science Conference, page 1955, March 2017.

Paul A. Rosen, G. L. Tyler, Essam A. Marouf, and Jack J. Lissauer. Resonance structures in Saturn's rings probed by radio occultation II. Results and interpretation. , 93(1):25–44, Sep 1991. doi: 10.1016/0019-1035(91)90161-L.

Marc Rovira-Navarro, Michel Rieutord, Theo Gerkema, Leo R. M. Maas, Wouter van der Wal, and Bert Vermeersen. Do tidally-generated inertial waves heat the subsurface oceans of Europa and Enceladus? *Icarus*, 321:126–140, March 2019. doi: 10.1016/j.icarus.2018.11.010.

Jason F. Rowe, Patrick Gaulme, Jack J. Lissauer, Mark S. Marley, Amy A. Simon, Heidi B. Hammel, Víctor Silva Aguirre, Thomas Barclay, Othman Benomar, Patrick Boumier, Douglas A. Caldwell, Sarah L. Casewell, William J. Chaplin, Knicole D. Colón, Enrico Corsaro, G. R. Davies, Jonathan J. Fortney, Rafael A. Garcia, John E. Gizis, Michael R. Haas, Benoît Mosser, and François-Xavier Schmider. Time-series Analysis of Broadband Photometry of Neptune from K2. , 153(4):149, Apr 2017. doi: 10.3847/1538-3881/aa6119.

H. Salo and C. F. Yoder. The dynamics of coorbital satellite systems. *A&A*, 205:309–327, October 1988.

Heikki Salo and Jyrki Hanninen. Neptune's Partial Rings: Action of Galatea on Self-Gravitating Arc Particles. *Science*, 282:1102, November 1998. doi: 10.1126/science.282.5391.1102.

D. Saumon, G. Chabrier, and H. M. van Horn. An Equation of State for Low-Mass Stars and Giant Planets. , 99:713, August 1995. doi: 10.1086/192204.

Ludwig Scheibe, Nadine Nettelmann, and Ronald Redmer. Thermal evolution of Uranus and Neptune. I. Adiabatic models. *A&A*, 632:A70, Dec 2019. doi: 10.1051/0004-6361/201936378.

Ludwig Scheibe, Nadine Nettelmann, and Ronald Redmer. Thermal evolution of Uranus and Neptune. II. Deep thermal boundary layer. *A&A*, 650:A200, June 2021. doi: 10.1051/0004-6361/202140663.

M. Showalter, J. J. Lissauer, I. de Pater, and R. S. French. A Three-Body Resonance Confines the Ring-Arcs of Neptune. In *AAS/Division for Planetary Sciences Meeting Abstracts #49*, volume 49 of *AAS/Division for Planetary Sciences Meeting Abstracts*, page 104.01, October 2017.

M. R. Showalter. The Rings of Uranus: Shepherded, or Not? In *EPSC-DPS Joint Meeting 2011*, volume 2011, page 1224, October 2011.

M. R. Showalter, I. de Pater, J. J. Lissauer, and R. S. French. The seventh inner moon of Neptune. *Nature*, 566(7744):350–353, February 2019. doi: 10.1038/s41586-019-0909-9.

Mark R. Showalter. Saturn's d ring in the voyager images. *Icarus*, 124(2): 677–689, Dec 1996. ISSN 0019-1035. doi: 10.1006/icar.1996.0241. URL `http://dx.doi.org/10.1006/icar.1996.0241`.

Mark R. Showalter and Jack J. Lissauer. The Second Ring-Moon System of Uranus: Discovery and Dynamics. *Science*, 311(5763):973–977, February 2006. doi: 10.1126/science.1122882.

F. H. Shu, J. N. Cuzzi, and J. J. Lissauer. Bending waves in Saturn's rings. , 53(2):185–206, February 1983. doi: 10.1016/0019-1035(83)90141-0.

B. Sicardy. Numerical exploration of planetary arc dynamics. , 89:197–219, February 1991. doi: 10.1016/0019-1035(91)90174-R.

B. Sicardy, R. Leiva, S. Renner, F. Roques, M. El Moutamid, P. Santos-Sanz, and J. Desmars. Ring dynamics around non-axisymmetric bodies with application to Chariklo and Haumea. *Nature Astronomy*, 3:146–153, April 2019. doi: 10.1038/s41550-018-0616-8.

Bruno Sicardy. Resonances in Nonaxisymmetric Gravitational Potentials. , 159(3):102, March 2020. doi: 10.3847/1538-3881/ab6d06.

Bruno Sicardy and Jack J. Lissauer. Dynamical models of the arcs in Neptune's 63K ring (1989N1R). *Advances in Space Research*, 12(11):81–95, November 1992. doi: 10.1016/0273-1177(92)90425-W.

Bruno Sicardy, Heikki Salo, Damya Souami, Stéfan Renner, Bruno Morgado, Felipe Braga-Ribas, Gustavo Benedetti-Rossi, and Thamiris de Santana. Rings around small bodies: the 1/3 resonance is key. In *European Planetary Science Congress*, pages EPSC2021–91, September 2021. doi: 10.5194/espc2021-91.

A. T. Sinclair. The orbital resonance amongst the Galilean satellites of Jupiter. , 171:59–72, April 1975. doi: 10.1093/mnras/171.1.59.

Andrew W. Smith and Jack J. Lissauer. Orbital stability of systems of closely-spaced planets. *Icarus*, 201(1):381–394, May 2009. doi: 10.1016/j.icarus.2008.12.027.

B. A. Smith, L. A. Soderblom, R. Beebe, D. Bliss, J. M. Boyce, A. Brahic, G. A. Briggs, R. H. Brown, S. A. Collins, A. F. Cook, S. K. Croft, J. N. Cuzzi, G. E. Danielson, M. E. Davies, T. E. Dowling, D. Godfrey, C. J. Hansen, C. Harris, G. E. Hunt, A. P. Ingersoll, T. V. Johnson, R. J. Krauss, H. Masursky, D. Morrison, T. Owen, J. B. Plescia, J. B. Pollack, C. C. Porco, K. Rages, C. Sagan, E. M. Shoemaker, L. A. Sromovsky, C. Stoker, R. G. Strom, V. E. Suomi, S. P. Synnott, R. J. Terrile, P. Thomas, W. R. Thompson, and J. Veverka. Voyager 2 in the Uranian System: Imaging Science Results. *Science*, 233(4759): 43–64, July 1986. doi: 10.1126/science.233.4759.43.

B. A. Smith, L. A. Soderblom, D. Banfield, C. Barnet, A. T. Basilevksy, R. F. Beebe, K. Bollinger, J. M. Boyce, A. Brahic, G. A. Briggs, R. H. Brown, C. Chyba, S. A. Collins, T. Colvin, A. F. Cook, D. Crisp, S. K. Croft, D. Cruikshank, J. N. Cuzzi, G. E. Danielson, M. E. Davies, E. de Jong, L. Dones, D. Godfrey, J. Goguen, I. Grenier, V. R. Haemmerle, H. Hammel, C. J. Hansen, C. P. Helfenstein, C. Howell, G. E. Hunt, A. P. Ingersoll, T. V. Johnson, J. Kargel, R. Kirk, D. I. Kuehn, S. Limaye, H. Masursky, A. McEwen, D. Morrison, T. Owen, W. Owen, J. B. Pollack, C. C. Porco, K. Rages, P. Rogers, D. Rudy, C. Sagan, J. Schwartz, E. M. Shoemaker, M. Showalter, B. Sicardy, D. Simonelli, J. Spencer, L. A. Sromovsky, C. Stoker, R. G. Strom, V. E. Suomi, S. P. Synott, R. J. Terrile, P. Thomas, W. R. Thompson, A. Verbiscer, and J. Veverka. Voyager 2 at Neptune: Imaging Science Results. *Science*, 246:1422–1449, December 1989. doi: 10.1126/science.246.4936.1422.

D. Souami, S. Renner, B. Sicardy, M. Langlois, B. Carry, P. Delorme, and P. Golaszewska. Neptune's ring arcs from VLT/SPHERE-IRDIS near-infrared observations. *arXiv e-prints*, art. arXiv:2110.12669, October 2021.

J. N. Spitale, R. A. Jacobson, C. C. Porco, and W. M. Owen, Jr. The Orbits of Saturn's Small Satellites Derived from Combined Historic and Cassini Imaging Observations. , 132: 692–710, August 2006. doi: 10.1086/505206.

D. Stevenson. EOS Transactions. In *EOS Transactions*, number 63, page 1020, 1982.

Lars Stixrude, Stefano Baroni, and Federico Grasselli. Thermal and Tidal Evolution of Uranus with a Growing Frozen Core. , 2(6):222, December 2021. doi: 10.3847/PSJ/ac2a47.

Philip J. Stooke. The Surfaces of Larissa and Proteus. *Earth Moon and Planets*, 65(1):31–54, January 1994. doi: 10.1007/BF00572198.

K.-L. Sun, M. Seiß, M. M. Hedman, and F. Spahn. Dust in the arcs of Methone and Anthe. , 284:206–215, March 2017. doi: 10.1016/j.icarus.2016.11.009.

D. Suzuki, D. P. Bennett, T. Sumi, I. A. Bond, L. A. Rogers, F. Abe, Y. Asakura, A. Bhattacharya, M. Donachie, M. Freeman, A. Fukui, Y. Hirao, Y. Itow, N. Koshimoto, M. C. A. Li, C. H. Ling, K. Masuda, Y. Matsubara, Y. Muraki, M. Nagakane, K. Onishi, H. Oyokawa, N. Rattenbury, To. Saito, A. Sharan, H. Shibai, D. J. Sullivan, P. J. Tristram, A. Yonehara, and MOA Collaboration. The Exoplanet Mass-ratio Function from the MOA-II Survey: Discovery of a Break and Likely Peak at a Neptune Mass. , 833(2):145, December 2016. doi: 10.3847/1538-4357/833/2/145.

Radwan Tajeddine, Philip D. Nicholson, Pierre-Yves Longaretti, Maryame El Moutamid, and Joseph A. Burns. What Confines the Rings of Saturn? , 232(2):28, October 2017. doi: 10.3847/1538-4365/aa8c09.

P. C. Thomas. Radii, shapes, and topography of the satellites of Uranus from limb coordinates. , 73(3):427–441, March 1988. doi: 10.1016/0019-1035(88)90054-1.

P. C. Thomas, J. A. Burns, M. Hedman, P. Helfenstein, S. Morrison, M. S. Tiscareno, and J. Veverka. The inner small satellites of Saturn: A variety of worlds. , 226:999–1019, September 2013. doi: 10.1016/j.icarus.2013.07.022.

Matthew S. Tiscareno, Colin J. Mitchell, Carl D. Murray, Daiana Di Nino, Matthew M. Hedman, Jürgen Schmidt, Joseph A. Burns, Jeffrey N. Cuzzi, Carolyn C. Porco, Kevin Beurle, and Michael W. Evans. Observations of Ejecta Clouds Produced by Impacts onto Saturn's Rings. *Science*, 340(6131):460–464, April 2013. doi: 10.1126/science.1233524.

R. H. D. Townsend and S. A. Teitler. GYRE: an open-source stellar oscillation code based on a new Magnus Multiple Shooting scheme. *Monthly Notices of the Royal Astronomical Society*, 435(4):3406–3418, Nov 2013. doi: 10.1093/mnras/stt1533.

W. Unno, Y. Osaki, H. Ando, and H. Shibahashi. *Nonradial Oscillations of Stars.* Univ. of Tokyo Press, 1979.

Dimitri Veras, Thomas R. Marsh, and Boris T. Gänsicke. Dynamical mass and multiplicity constraints on co-orbital bodies around stars. , 461(2):1413–1420, September 2016. doi: 10.1093/mnras/stw1324.

P. E. Verrier and C. R. McInnes. Periodic orbits for three and four co-orbital bodies. , 442 (4):3179–3191, August 2014. doi: 10.1093/mnras/stu1056.

David Vokrouhlický and David Nesvorný. Transit Timing Variations for Planets Co-orbiting in the Horseshoe Regime. , 791(1):6, August 2014. doi: 10.1088/0004-637X/791/1/6.

S. V. Vorontsov and V. N. Zharkov. Natural Oscillations of the Giant Planets - Influence of Rotation and Ellipticity. , 25:627, October 1981.

James W. Warwick, David R. Evans, Joseph H. Romig, Constance B. Sawyer, Michael D. Desch, Michael L. Kaiser, Joseph K. Alexander, Thomas D. Carr, David H. Staelin, Samuel Gulkis, Robert L. Poynter, Monique Aubier, Andre Boischot, Yolande Leblanc, Alain Lecacheux, Bent M. Pedersen, and Philippe Zarka. Voyager 2 Radio Observations of Uranus. *Science*, 233(4759):102–106, July 1986. doi: 10.1126/science.233.4759.102.

James W. Warwick, David R. Evans, Gerard R. Peltzer, Robert G. Peltzer, Joseph H. Romig, Constance B. Sawyer, Anthony C. Riddle, Andrea E. Schweitzer, Michael D. Desch, Michael L. Kaiser, William M. Farrell, Thomas D. Carr, Imke de Pater, David H. Staelin, Samuel Gulkis, Robert L. Poynter, Andre Boischot, Francoise Genova, Yolande Leblanc, Alain Lecacheux, Bent M. Pedersen, and Philippe Zarka. Voyager Planetary Radio Astronomy at Neptune. *Science*, 246(4936):1498–1501, December 1989. doi: 10.1126/science.246.4936.1498.

Hugh F. Wilson, Michael L. Wong, and Burkhard Militzer. Superionic to Superionic Phase

Change in Water: Consequences for the Interiors of Uranus and Neptune. , 110(15):151102, April 2013. doi: 10.1103/PhysRevLett.110.151102.

J. Wisdom. The resonance overlap criterion and the onset of stochastic behavior in the restricted three-body problem. *AJ*, 85:1122–1133, August 1980. doi: 10.1086/112778.

Yanqin Wu and Yoram Lithwick. Memoirs of a Giant Planet. , 881(2):142, August 2019. doi: 10.3847/1538-4357/ab2892.

Ke Zhang and Douglas P. Hamilton. Orbital resonances in the inner neptunian system. I. The 2:1 Proteus Larissa mean-motion resonance. *Icarus*, 188(2):386–399, June 2007. doi: 10.1016/j.icarus.2006.12.002.

Ke Zhang and Douglas P. Hamilton. Orbital resonances in the inner neptunian system. II. Resonant history of Proteus, Larissa, Galatea, and Despina. *Icarus*, 193(1):267–282, January 2008. doi: 10.1016/j.icarus.2007.08.024.

Appendix A: Supplemental figures concerning the dynamics of multiple bodies in a corotation resonance

In this Appendix I present additional figures relating the the Aegaeon project (see Chapter 2).

Two characteristics of Aegaeon's corotation resonance distinguish it from those of Anthe and Methone. One is that Aegaeon is closer to exact resonance than Anthe and Methone are, as shown in Figure 5.14. The other is that the ratio of total mass in Aegaeon's ring arc apart from Aegaeon is comparable to Aegaeon's own mass, as shown in Figure 5.15. If these two phenomena were causally connected, as Hedman et al. (2010) suspected, then Aegaeon's orbital evolution would have been linked to interactions with other masses in its corotation resonance. As we showed, however, the simultaneous occurrence of these two phenomena is a coincidence (A'Hearn et al., 2019), which makes Aegaeon's presence so close to the deepest part of its corotation resonance site all the more surprising.

Figure 5.16 summarizes changes that occur to a body's orbit when it experiences forces in certain directions. Let us consider the time derivatives of eccentricity and longitude of

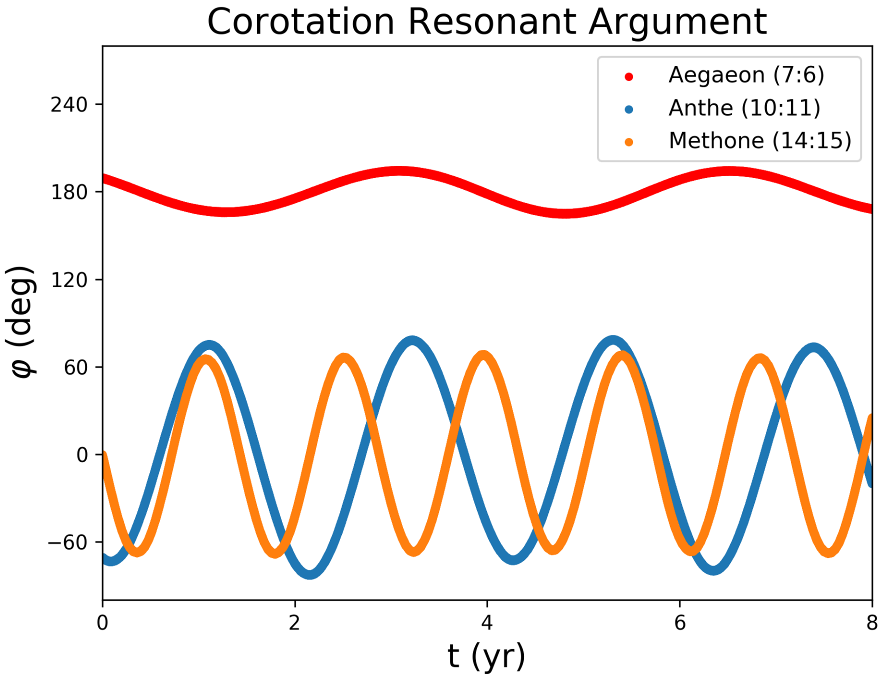

Figure 5.14: Resonant arguments for Aegaeon, Anthe, and Methone from an eight-year simulation, starting from their locations on April 10, 2010 according to the SPICE kernels. Aegaeon's resonant argument $\varphi = 7\lambda_{\text{Mimas}} - 6\lambda_{\text{Aegaeon}} - \varpi_{\text{Mimas}}$ oscillates around 180 degrees because it is interior to Mimas. Anthe's resonant argument $\varphi = 11\lambda_{\text{Anthe}} - 10\lambda_{\text{Mimas}} - \varpi_{\text{Mimas}}$ and Methone's resonant argument $\varphi = 15\lambda_{\text{Methone}} - 14\lambda_{\text{Mimas}} - \varpi_{\text{Mimas}}$ oscillate around zero because they are exterior to Mimas. Since the amplitude of oscillations is much smaller for Aegaeon, it is closer to exact resonance with Mimas than Anthe and Methone are.

pericenter (Hedman, 2018), approximated for low-eccentricity, low-inclination orbits:

$$\frac{de}{dt} = n\left(\frac{F_r}{F_G}\sin f + 2\frac{F_\lambda}{F_G}\cos f\right) \tag{5.5}$$

$$\frac{d\varpi}{dt} = \frac{n}{e}\left(-\frac{F_r}{F_G}\cos f + 2\frac{F_\lambda}{F_G}\sin f\right) \tag{5.6}$$

A close encounter with body 3 can alter body 4's eccentricity and longitude of pericenter at any location in its orbit, but is twice as effective when the tug is in a longitudinal direction.

The effect of a close encounter on eccentricity and longitude of pericenter depends on where in each body's orbit the closest approach occurs. If body 4 is at apocenter at closest approach, a prograde tug will decrease its eccentricity (and increase its semimajor axis), whereas a retrograde tug will increase its eccentricity (and decrease its semimajor axis). At pericenter, on the other hand, a prograde tug will increase its eccentricity, and a retrograde

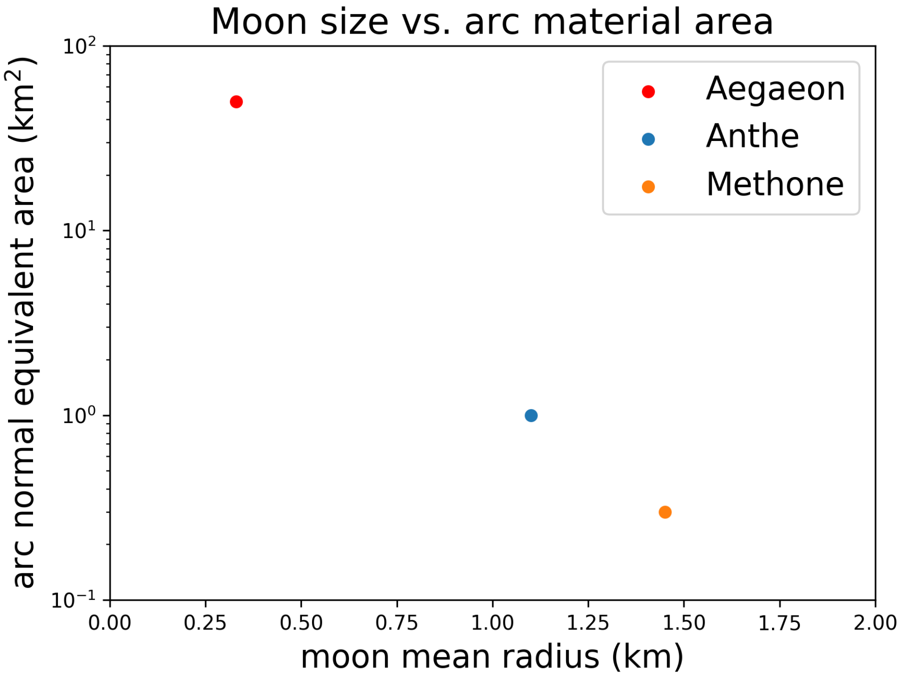

Figure 5.15: The size of both Anthe and Methone compared to the area that the material in their ring arcs take up. Aegaeon is the smallest of these three moons, and the material in its ring arc takes up more area compared to the ring arcs of Anthe and Methone.

tug will decrease its eccentricity.

If pericenter is on the left and apocenter is on the right, then to increase eccentricity, we require a downward force at any place in its orbit. An upward force at any place in its orbit would decrease eccentricity. Downward and upward forces are longitudinal (and thus can be twice as effective) at pericenter and at apocenter.

One example given in Hedman (2018) is that a radial force applied near apocenter will delay body 4's inward motion, and thus cause the pericenter to shift forward in longitude. Clocking the longitude of pericenter forward can be done at any point in the orbit as long as the force is to the right. In contrast, a force to the left shifts the longitude of pericenter backward. Since right and left are longitudinal halfway between pericenter and apocenter, we can expect the most significant alterations to the longitude of pericenter to occur during close encounters at these locations.

Figure 5.17 illustrates how far Aeageon is from completely dominating its own corotation resonance site, despite it being the largest mass in its ring arc.

Using the spice kernels from April 10, 2010 for Mimas and Aegaeon, we were able to

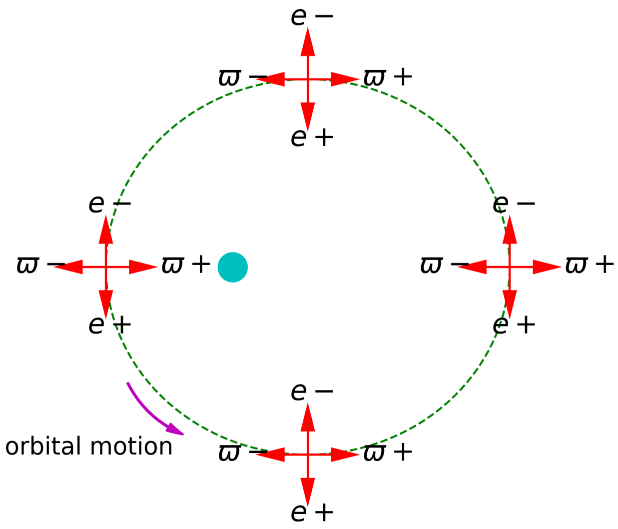

Figure 5.16: On an elliptical orbital trajectory (green dashed line) around a primary (cyan) body at one focus of the ellipse, a body that experiences an external force in the direction of the red arrow undergoes changes in its orbital elements: $e+$ indicates an increase in eccentricity, $e-$ a decrease in eccentricity, $\varpi+$ an increase in the longitude of pericenter, $\varpi-$ a decrease in the longitude of pericenter.

reproduce similar plots of Aegaeon's resonant arguments and their Fourier spectra to those found in (see Figures 5.18 and 5.19; Hedman et al. 2010). In our Fourier analyses, we used a brute force technique that allowed for custom determination of the sample period bounds and number of samples. To investigate the space of the corotation and Lindblad eccentricity resonances, we varied Aegaeon's initial semimajor axis and mean longitude with step-sizes of 0.5 km and 0.5 degrees over the range of the expected resonance space. Since `Mercury6` uses the osculating orbital elements, for each simulation, the initial geometric orbital elements were converted to state vectors using the equations found in Renner and Sicardy (2006). After each eight-year simulation, the resonant argument of the corotation eccentricity resonance was fit to a least squares sine wave with a linearly time-dependent amplitude. The mean amplitude of the fit sine wave was then mapped to a color in order to produce a map of the corotation eccentricity resonance, displayed in Figure 5.20. For 2.08% of the simulations, the sine fit produced by our algorithm did not match up with

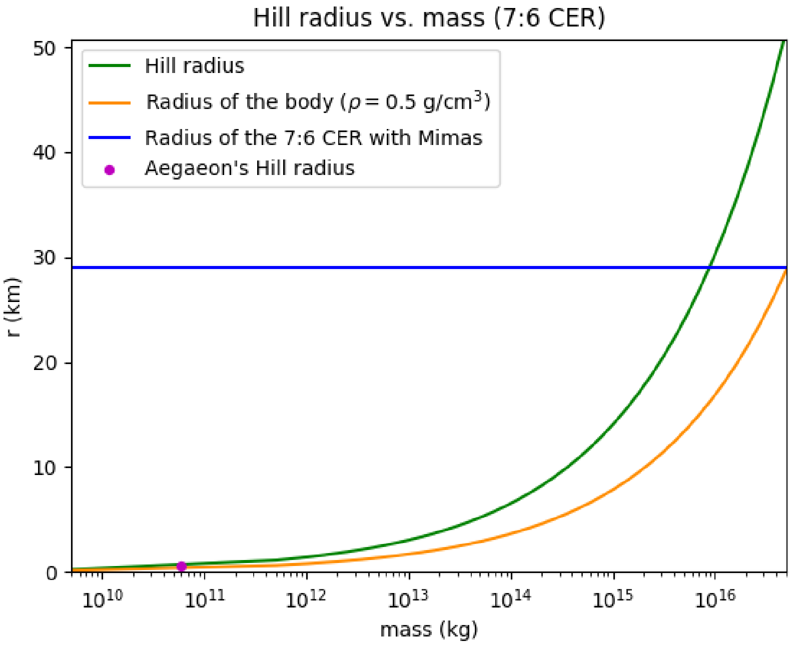

Figure 5.17: This plot shows the relationship between a body's mass, radius, and Hill radius, compared to the width of the 7:6 corotation resonance with Mimas.

the resonant argument. This happened mostly on the fringe of the resonance. For these cases, the amplitude value given by the sine fit was discarded, and an amplitude value was interpolated from surrounding mean longitude steps in the resonance map. The map of the corotation eccentricity resonance produced in Figure 5.20 is consistent with the expected shape for a CER that appears in El Moutamid et al. (2014). The width of the CER seen in the map is approximately 60 km, and the calculated value using the equation given in El Moutamid et al. (2016) is 58 km. Using colors to indicate the libration amplitude of the resonant argument, it becomes evident that proximity to the location of exact resonance is strongly correlated with the resonant argument's libration amplitude.

Two different criteria were employed to make Lindblad resonance maps. For the Lindblad resonance shown in Figure 5.22, the number of times the resonant argument crossed the ±180° limits was counted, and the standard deviation from zero was computed in order to produce maps of the Lindblad eccentricity resonance. An alternate way to map the Lindblad resonance is shown in Figure 5.21. The first map (see Figure 5.21) uses colors to indicate the resonant argument's deviation from zero. The next map (see Figure 5.22)

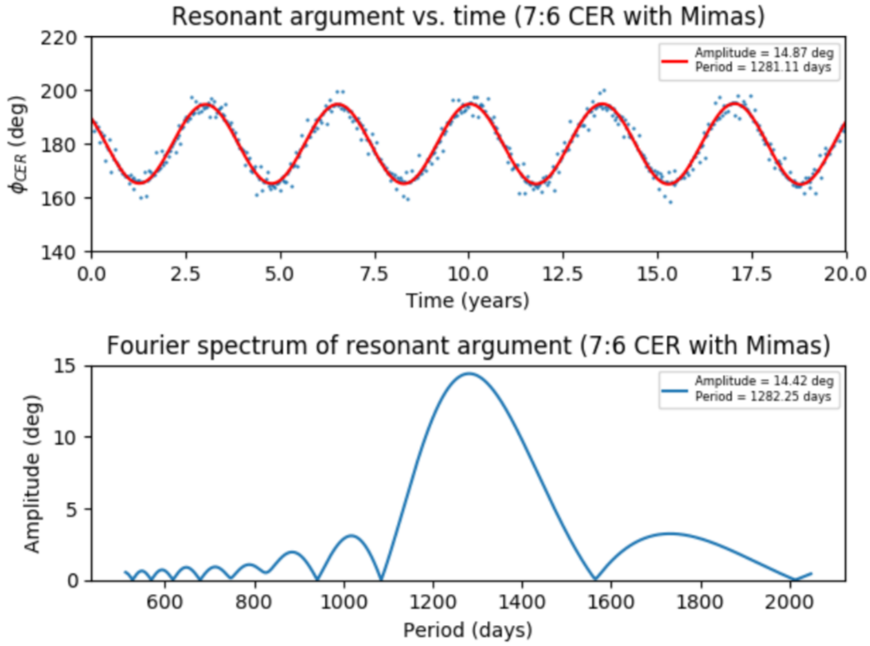

Figure 5.18: (Top) Corotation eccentricity resonant argument vs. time. Blue dots are data points from a 20-year simulation with the initial values equivalent to those given by the SPICE kernels for April 10, 2010. These data were fit to a sine function (red), which yields the best-fit amplitude and period, listed in the legend. (Bottom) Fourier spectrum of the data from the top panel, with an amplitude and period listed in the legend.

shows by colors how many times the resonant argument crossed over the ±180° limit. The Lindblad resonance maps also show that around a mean longitude 0° away from the location of exact resonance the resonant argument tends to oscillate around some value other than zero.

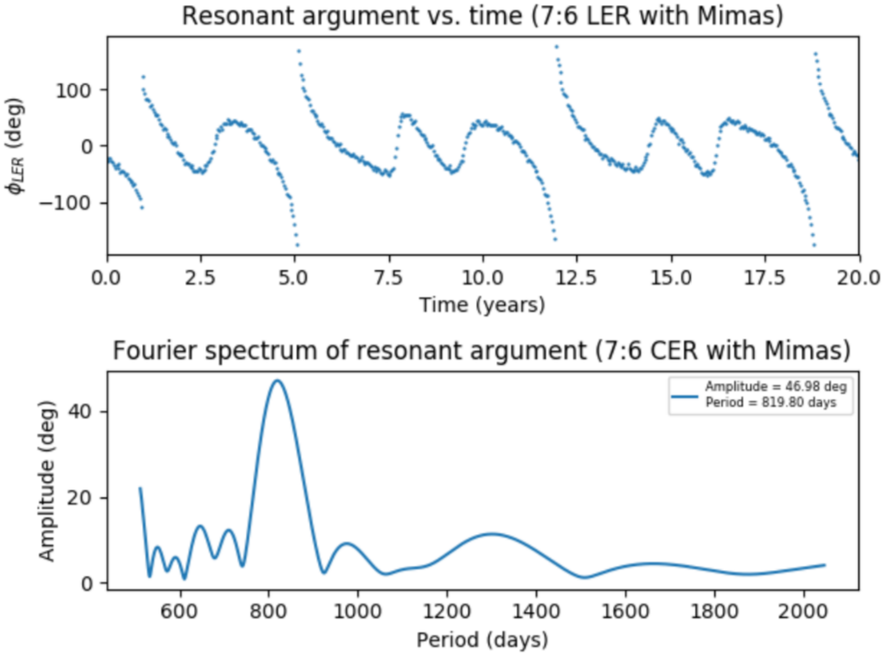

Figure 5.19: (Top) Lindblad eccentricity resonant argument vs. time. Blue dots are data points from a 20-year simulation with the initial values equivalent to those given by the SPICE kernels for April 10, 2010. (Bottom) Fourier spectrum of the data from the top panel, with an amplitude and period listed in the legend.

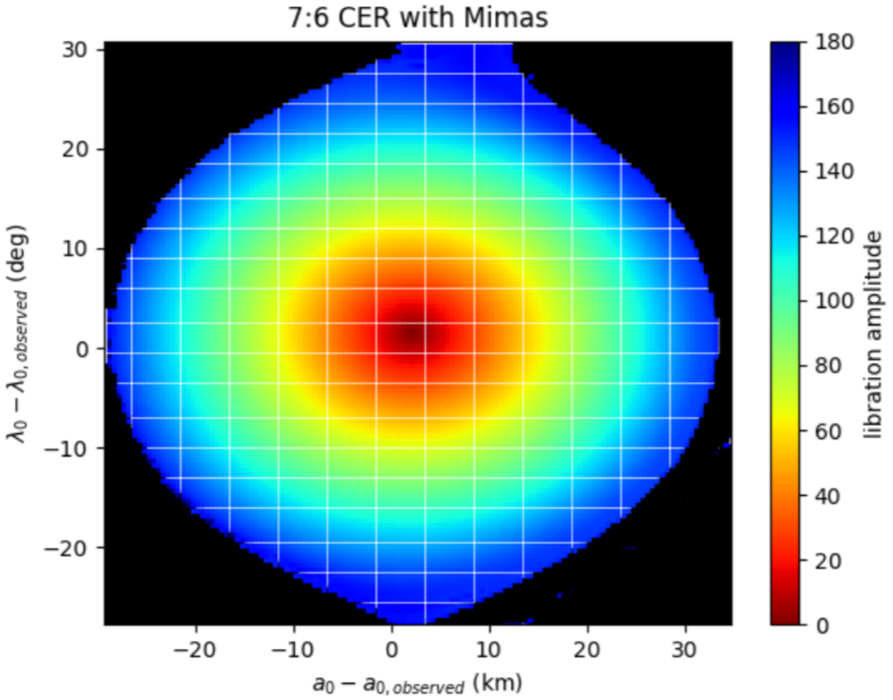

Figure 5.20: A map of one corotation eccentricity resonance site. The axes are zeroed at Aegaeon's initial location when the SPICE kernels of April 10, 2010 are used. The black regions are outside of the corotation resonance, which was determined to be the case if the maximum and minimum values of the resonant argument during the eight-year orbital simulation differed by more than 354°. This was taken as an indication that the resonant argument was likely not oscillating around 180°, but cycling through all 360°. The colors of the region inside the resonance correspond to the amplitude of the resonant argument's librations.

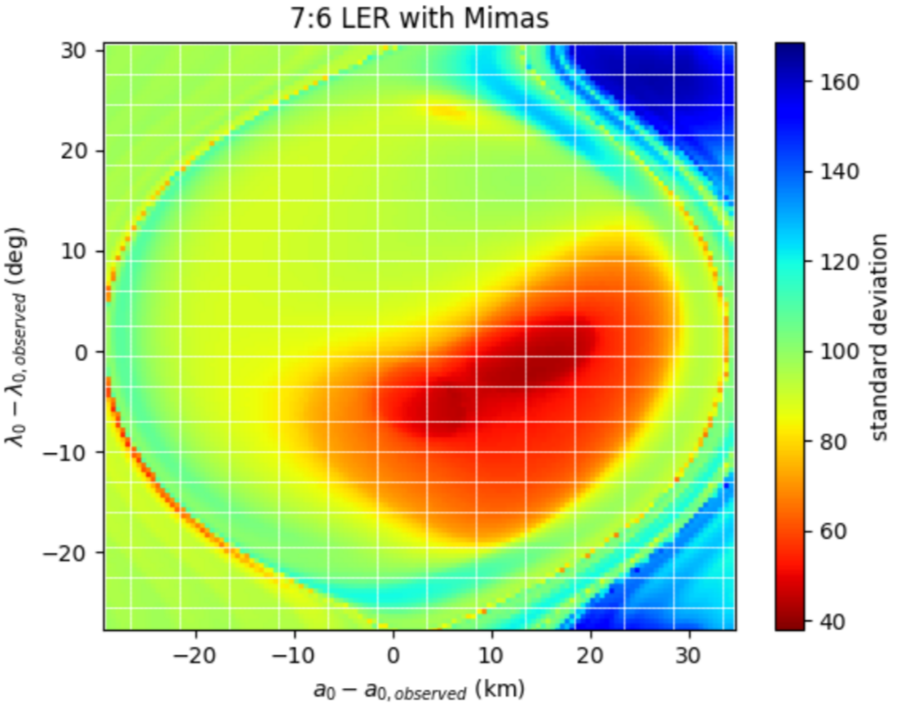

Figure 5.21: This map of the Lindblad eccentricity resonance uses colors to indicate the resonant argument's deviation from zero.

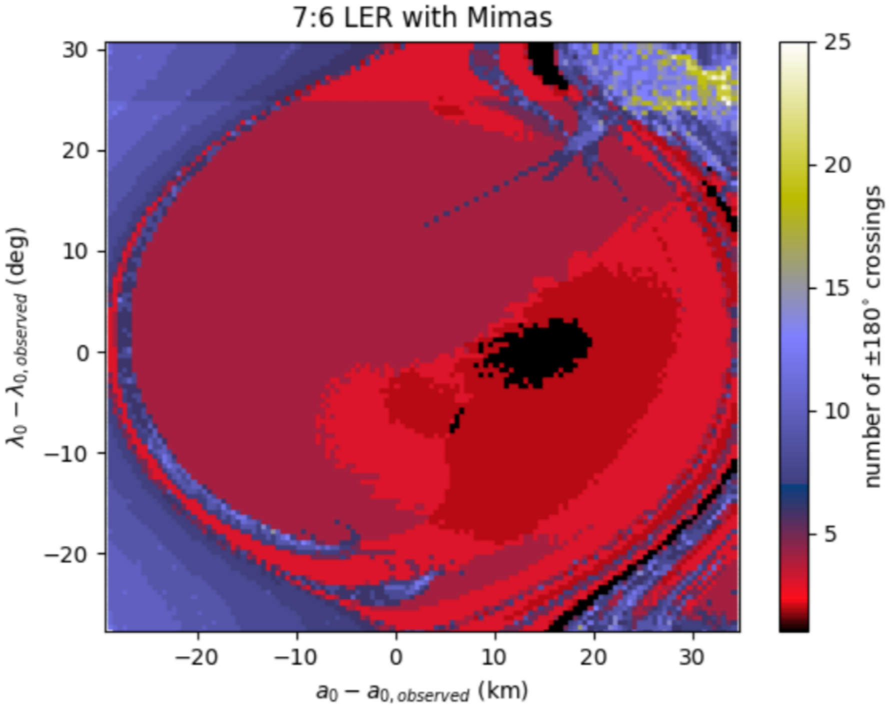

Figure 5.22: This map of the Lindblad eccentricity resonance uses colors to indicate the number of times the resonant argument crossed over one of the ±180° limits during the eight-year simulation.

Appendix B: Supplemental figures concerning the D68 clumps

In this Appendix I present additional figures relating the the D68 project (see Chapter 3).

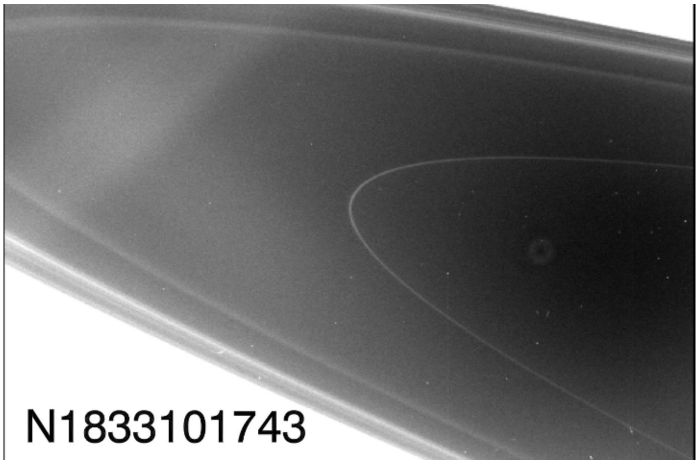

Figure 5.23: This image, taken on 2 February 2016, shows a region of the D68 ringlet without observable clumps, representative of the whole ringlet before 2014 (Hedman, 2019). D68 is the narrow ring near the center of the image.

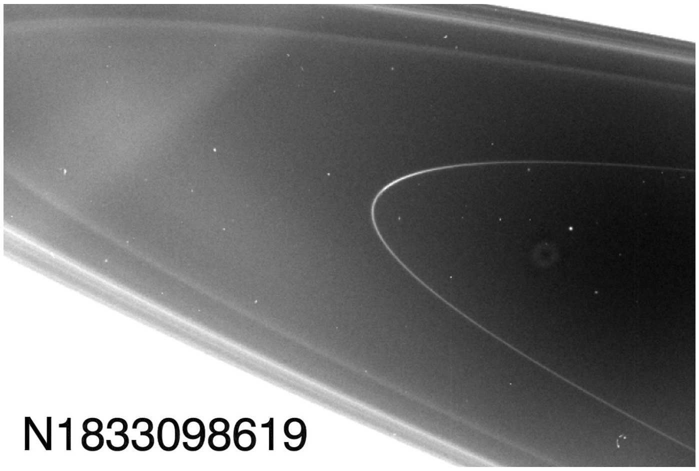

Figure 5.24: This image, also taken on 2 February 2016, shows one of the bright clumps in the D68 ringlet. D68 is the narrow ring near the center of the image. The bright feature is located near the ansa. (Hedman, 2019)

Appendix C: Supplemental figures concerning the Uranian and Neptunian rings

In this Appendix I present additional figures relating the the ice giant ring seismology project (see Chapter 4). Appendices C.1. and C.2. were submitted for publication along with the paper, though with slightly different formatting and labeling. Appendix C.3. contains Voyager images of the Uranian and Neptunian rings, but was included in the submission for publication.

Appendix C.1. Extended Tables of f-mode frequencies and resonance locations

In this appendix, we present all the calculated f-mode frequencies and resonance locations for all the models. Table 5.5 shows the initial estimates by Marley et al. (1988). Our Lindblad resonance calculations are provided in tables: the Uranus thick model in Table 5.6, the Uranus medium model in Table 5.7, the Uranus thin model in Table 5.8, the Uranus adiabatic model in Table 5.9, the Uranus shallow model in Table 5.10, and the Neptune model in Table 5.11. Similarly, our vertical resonance calculations are then provided in tables: the Uranus thick model in Table 5.12, the Uranus medium model in Table 5.13, the Uranus thin model in Table 5.14, the Uranus adiabatic model in Table 5.15, the Uranus shallow model in Table 5.16, and the Neptune model in Table 5.17. Error bars are one-sided because the frequencies and resonance locations are only calculated to first order. Second-order calculations would universally lower the frequencies, which would cause the resonance locations to be more distant from the planet.

ℓ	m	model	Ω_{pat} (deg/day)	r_{res} (km)
2	2	6	1683	48,300
		5	1718	47,700
		4	1767	46,800
3	3	6	2015	39,600
		5	2025	39,500
		4	2054	39,100
4	4	6	2005	38,100
		5	2010	38,000
		4	2030	37,800
5	5	6	1941	37,900
		5	1941	37,900
		4	1950	37,800

Table 5.5: Predicted Lindblad resonance locations among the inner rings of Uranus from Marley et al. (1988).

Table 5.6: Pattern frequencies and Lindblad resonance locations of the thick Uranus model

Uranus Thick model

ℓ	m	Ω_{pat} (deg/day)	r_{res} (km)
$\ell = m$			
2	2	2218.7 - 62.4	40196 + 772
3	3	2228.9 - 59.9	37054 + 678
4	4	2077.7 - 53.6	37198 + 653
5	5	1922.5 - 47.8	38123 + 644
6	6	1788.3 - 42.9	39263 + 641
7	7	1677.2 - 39.1	40418 + 639
8	8	1586.7 - 35.9	41503 + 638
9	9	1513.3 - 33.4	42481 + 636
10	10	1453.5 - 31.4	43345 + 634
11	11	1404.4 - 29.7	44106 + 632
12	12	1363.3 - 28.3	44780 + 629
13	13	1328.1 - 27.0	45386 + 626
14	14	1297.5 - 26.0	45939 + 623
15	15	1270.5 - 25.0	46451 + 620
16	16	1246.2 - 24.2	46928 + 617
17	17	1224.3 - 23.4	47377 + 614
18	18	1204.3 - 22.7	47802 + 611
19	19	1185.9 - 22.1	48205 + 608
20	20	1169.0 - 21.5	48589 + 605
21	21	1153.2 - 21.0	48955 + 602
22	22	1138.6 - 20.5	49305 + 600
23	23	1125.0 - 20.0	49640 + 597
24	24	1112.2 - 19.6	49962 + 594
25	25	1100.2 - 19.2	50271 + 592
$\ell - m = 2$			
4	2	3755.8 - 107.2	28306 + 551
5	3	2919.8 - 79.6	30955 + 575
6	4	2460.7 - 64.4	33234 + 592
7	5	2166.4 - 54.7	35208 + 604
8	6	1961.7 - 47.9	36916 + 613
9	7	1812.2 - 43.0	38388 + 618
10	8	1699.1 - 39.2	39654 + 621
11	9	1610.9 - 36.3	40749 + 623
12	10	1540.2 - 33.9	41705 + 623
13	11	1482.1 - 32.0	42553 + 622
14	12	1433.1 - 30.3	43314 + 621
15	13	1391.1 - 28.9	44007 + 619
16	14	1354.5 - 27.6	44644 + 617
17	15	1322.1 - 26.6	45234 + 615
18	16	1293.3 - 25.6	45784 + 613
19	17	1267.3 - 24.7	46299 + 611
20	18	1243.8 - 23.9	46784 + 609
21	19	1222.4 - 23.2	47242 + 606
22	20	1202.7 - 22.5	47675 + 604
23	21	1184.6 - 21.9	48087 + 602
24	22	1167.9 - 21.3	48478 + 599
25	23	1152.3 - 20.8	48852 + 597
$\ell - m = 4$			
7	3	3307.8 - 91.1	28487 + 535
8	4	2711.8 - 71.9	31153 + 562
9	5	2350.3 - 60.1	33349 + 581
10	6	2108.3 - 52.3	35187 + 593
11	7	1935.4 - 46.6	36743 + 602
12	8	1805.6 - 42.4	38080 + 607
13	9	1704.4 - 39.1	39246 + 610
14	10	1622.9 - 36.4	40278 + 612
15	11	1555.6 - 34.1	41203 + 613
16	12	1498.8 - 32.3	42041 + 614
17	13	1450.1 - 30.6	42807 + 613
18	14	1407.7 - 29.2	43512 + 612
19	15	1370.5 - 28.0	44165 + 611
20	16	1337.4 - 26.9	44772 + 610
21	17	1307.8 - 25.9	45340 + 608
22	18	1281.1 - 25.0	45873 + 607
23	19	1256.9 - 24.2	46375 + 605
24	20	1234.7 - 23.5	46849 + 603
25	21	1214.4 - 22.8	47298 + 601

Table 5.7: Pattern frequencies and Lindblad resonance locations of the medium Uranus model

Uranus Medium model			
ℓ	m	$\Omega_{\rm pat}$ (deg/day)	$r_{\rm res}$ (km)
$\ell = m$			
2	2	2207.8 - 62.1	40328 + 774
3	3	2234.6 - 60.1	36991 + 678
4	4	2096.0 - 54.2	36981 + 651
5	5	1949.2 - 48.6	37774 + 641
6	6	1819.6 - 43.9	38812 + 636
7	7	1710.1 - 40.0	39899 + 634
8	8	1618.6 - 36.8	40956 + 632
9	9	1542.1 - 34.2	41951 + 630
10	10	1477.8 - 32.0	42870 + 629
11	11	1423.3 - 30.1	43714 + 627
12	12	1377.0 - 28.6	44481 + 626
13	13	1337.5 - 27.3	45174 + 624
14	14	1303.6 - 26.1	45797 + 621
15	15	1274.3 - 25.1	46358 + 619
16	16	1248.7 - 24.3	46867 + 616
17	17	1226.0 - 23.5	47335 + 614
18	18	1205.5 - 22.8	47771 + 611
19	19	1186.8 - 22.1	48180 + 608
20	20	1169.7 - 21.5	48568 + 605
21	21	1153.9 - 21.0	48937 + 602
22	22	1139.2 - 20.5	49289 + 600
23	23	1125.4 - 20.0	49626 + 597
24	24	1112.6 - 19.6	49949 + 594
25	25	1100.5 - 19.2	50259 + 592
$\ell - m = 2$			
4	2	3792.6 - 108.4	28123 + 548
5	3	2963.8 - 81.0	30649 + 571
6	4	2506.6 - 65.8	32828 + 587
7	5	2210.9 - 56.0	34735 + 598
8	6	2002.6 - 49.1	36413 + 606
9	7	1847.7 - 43.9	37895 + 612
10	8	1728.0 - 40.0	39211 + 616
11	9	1633.0 - 36.8	40381 + 618
12	10	1556.0 - 34.3	41424 + 619
13	11	1492.6 - 32.2	42352 + 620
14	12	1439.9 - 30.5	43178 + 619
15	13	1395.4 - 29.0	43917 + 618
16	14	1357.2 - 27.7	44584 + 617
17	15	1324.0 - 26.6	45192 + 615
18	16	1294.6 - 25.6	45753 + 613
19	17	1268.4 - 24.7	46275 + 611
20	18	1244.6 - 23.9	46764 + 609
21	19	1223.1 - 23.2	47224 + 606
22	20	1203.3 - 22.5	47660 + 604
23	21	1185.1 - 21.9	48073 + 602
24	22	1168.3 - 21.4	48466 + 599
25	23	1152.7 - 20.8	48840 + 597
$\ell - m = 4$			
7	3	3379.5 - 93.3	28084 + 528
8	4	2770.6 - 73.6	30711 + 555
9	5	2397.7 - 61.5	32909 + 574
10	6	2145.0 - 53.3	34785 + 587
11	7	1962.4 - 47.3	36406 + 597
12	8	1824.4 - 42.9	37819 + 603
13	9	1716.8 - 39.4	39058 + 608
14	10	1630.7 - 36.6	40150 + 611
15	11	1560.4 - 34.3	41117 + 612
16	12	1501.9 - 32.3	41983 + 613
17	13	1452.2 - 30.7	42766 + 613
18	14	1409.2 - 29.3	43481 + 612
19	15	1371.6 - 28.0	44140 + 611
20	16	1338.3 - 26.9	44752 + 610
21	17	1308.6 - 25.9	45323 + 608
22	18	1281.8 - 25.0	45858 + 607
23	19	1257.4 - 24.2	46361 + 605
24	20	1235.2 - 23.5	46836 + 603
25	21	1214.9 - 22.8	47286 + 601

Table 5.8: Pattern frequencies and Lindblad resonance locations of the thin Uranus model

Uranus Thin model

ℓ	m	Ω_{pat} (deg/day)	r_{res} (km)
$\ell = m$			
2	2	2191.7 - 61.6	40525 + 777
3	3	2235.0 - 60.1	36986 + 678
4	4	2108.1 - 54.6	36840 + 650
5	5	1968.8 - 49.3	37524 + 639
6	6	1843.2 - 44.7	38481 + 634
7	7	1735.2 - 40.8	39514 + 631
8	8	1643.7 - 37.6	40538 + 629
9	9	1566.4 - 34.9	41517 + 627
10	10	1500.6 - 32.6	42435 + 626
11	11	1444.4 - 30.7	43288 + 624
12	12	1395.9 - 29.1	44080 + 622
13	13	1353.6 - 27.6	44814 + 620
14	14	1316.7 - 26.4	45494 + 618
15	15	1284.2 - 25.3	46121 + 616
16	16	1255.6 - 24.4	46695 + 615
17	17	1230.6 - 23.6	47216 + 612
18	18	1208.5 - 22.8	47691 + 610
19	19	1188.9 - 22.2	48125 + 608
20	20	1171.2 - 21.6	48528 + 605
21	21	1155.0 - 21.0	48906 + 602
22	22	1140.0 - 20.5	49264 + 600
23	23	1126.2 - 20.0	49605 + 597
24	24	1113.2 - 19.6	49931 + 594
25	25	1101.1 - 19.2	50243 + 592
$\ell - m = 2$			
4	2	3818.5 - 109.2	27996 + 547
5	3	2997.4 - 82.1	30419 + 568
6	4	2542.4 - 67.0	32520 + 583
7	5	2246.1 - 57.1	34371 + 594
8	6	2035.9 - 50.1	36015 + 602
9	7	1878.4 - 44.8	37482 + 608
10	8	1756.0 - 40.8	38794 + 612
11	9	1658.0 - 37.5	39974 + 614
12	10	1577.8 - 34.9	41040 + 615
13	11	1511.0 - 32.7	42008 + 616
14	12	1454.5 - 30.8	42888 + 616
15	13	1406.3 - 29.2	43690 + 616
16	14	1364.8 - 27.9	44418 + 615
17	15	1329.0 - 26.7	45077 + 614
18	16	1297.9 - 25.7	45675 + 613
19	17	1270.6 - 24.8	46220 + 611
20	18	1246.2 - 24.0	46724 + 609
21	19	1224.3 - 23.2	47194 + 606
22	20	1204.3 - 22.6	47635 + 604
23	21	1185.9 - 22.0	48052 + 602
24	22	1169.0 - 21.4	48447 + 599
25	23	1153.3 - 20.9	48824 + 597
$\ell - m = 4$			
7	3	3438.3 - 95.2	27763 + 524
8	4	2820.2 - 75.1	30350 + 551
9	5	2440.1 - 62.8	32527 + 569
10	6	2181.5 - 54.4	34396 + 583
11	7	1993.7 - 48.2	36024 + 592
12	8	1850.8 - 43.6	37459 + 599
13	9	1738.3 - 39.9	38734 + 604
14	10	1647.5 - 37.0	39876 + 607
15	11	1572.8 - 34.6	40902 + 610
16	12	1510.4 - 32.5	41825 + 611
17	13	1457.8 - 30.8	42656 + 612
18	14	1412.9 - 29.4	43405 + 612
19	15	1374.1 - 28.1	44087 + 611
20	16	1340.1 - 27.0	44713 + 610
21	17	1309.9 - 26.0	45292 + 608
22	18	1282.8 - 25.1	45833 + 607
23	19	1258.3 - 24.3	46340 + 605
24	20	1236.0 - 23.5	46818 + 603
25	21	1215.5 - 22.8	47270 + 601

Table 5.9: Pattern frequencies and Lindblad resonance locations of the adiabatic Uranus model

Uranus Adiabatic model

ℓ	m	$\Omega_{\rm pat}$ (deg/day)	$r_{\rm res}$ (km)
$\ell = m$			
2	2	2360.4 - 67.0	38571 + 747
3	3	2150.9 - 57.5	37943 + 692
4	4	1963.4 - 50.2	38627 + 672
5	5	1820.2 - 44.8	39537 + 662
6	6	1710.1 - 40.7	40451 + 655
7	7	1623.0 - 37.6	41314 + 649
8	8	1552.2 - 35.0	42115 + 645
9	9	1493.3 - 32.9	42858 + 640
10	10	1443.4 - 31.1	43547 + 637
11	11	1400.4 - 29.6	44189 + 633
12	12	1362.9 - 28.3	44787 + 630
13	13	1329.8 - 27.1	45349 + 626
14	14	1300.2 - 26.1	45876 + 623
15	15	1273.7 - 25.1	46373 + 620
16	16	1249.6 - 24.3	46843 + 617
17	17	1227.7 - 23.5	47289 + 614
18	18	1207.7 - 22.8	47712 + 611
19	19	1189.3 - 22.2	48115 + 608
20	20	1172.2 - 21.6	48499 + 605
21	21	1156.4 - 21.1	48866 + 602
22	22	1141.7 - 20.6	49217 + 600
23	23	1127.9 - 20.1	49553 + 597
24	24	1115.0 - 19.7	49876 + 594
25	25	1102.9 - 19.2	50187 + 592
$\ell - m = 2$			
4	2	3534.8 - 100.4	29473 + 571
5	3	2755.2 - 74.6	32175 + 594
6	4	2347.7 - 61.1	34291 + 607
7	5	2093.3 - 52.6	36022 + 615
8	6	1917.5 - 46.7	37481 + 620
9	7	1787.6 - 42.3	38739 + 623
10	8	1687.0 - 38.9	39843 + 624
11	9	1606.3 - 36.2	40826 + 624
12	10	1539.9 - 33.9	41711 + 623
13	11	1484.1 - 32.0	42515 + 622
14	12	1436.3 - 30.4	43251 + 621
15	13	1394.8 - 29.0	43930 + 619
16	14	1358.3 - 27.8	44559 + 617
17	15	1326.0 - 26.7	45145 + 615
18	16	1297.1 - 25.7	45694 + 613
19	17	1271.1 - 24.8	46209 + 611
20	18	1247.4 - 24.0	46694 + 609
21	19	1225.9 - 23.3	47153 + 606
22	20	1206.1 - 22.6	47587 + 604
23	21	1187.9 - 22.0	48000 + 602
24	22	1171.0 - 21.4	48392 + 599
25	23	1155.3 - 20.9	48767 + 597
$\ell - m = 4$			
6	2	4260.5 - 122.2	26026 + 509
7	3	3190.8 - 87.6	29179 + 546
8	4	2648.1 - 70.0	31649 + 570
9	5	2317.2 - 59.2	33665 + 585
10	6	2092.9 - 51.9	35359 + 596
11	7	1929.9 - 46.5	36813 + 603
12	8	1805.5 - 42.4	38083 + 607
13	9	1706.9 - 39.1	39208 + 610
14	10	1626.7 - 36.5	40215 + 612
15	11	1559.9 - 34.3	41126 + 613
16	12	1503.3 - 32.4	41957 + 613
17	13	1454.6 - 30.8	42719 + 613
18	14	1412.1 - 29.4	43422 + 612
19	15	1374.7 - 28.1	44074 + 611
20	16	1341.5 - 27.0	44682 + 610
21	17	1311.7 - 26.0	45251 + 608
22	18	1284.8 - 25.1	45785 + 607
23	19	1260.4 - 24.3	46288 + 605
24	20	1238.2 - 23.6	46763 + 603
25	21	1217.7 - 22.9	47212 + 601

Table 5.10: Pattern frequencies and Lindblad resonance locations of the shallow Uranus model

Uranus Shallow model

ℓ	m	$\Omega_{\rm pat}$ (deg/day)	$r_{\rm res}$ (km)
$\ell = m$			
2	2	2052.5 - 57.2	42337 + 805
3	3	2162.1 - 57.9	37812 + 690
4	4	2073.0 - 53.7	37254 + 657
5	5	1959.5 - 49.2	37642 + 643
6	6	1851.0 - 45.1	38373 + 636
7	7	1753.2 - 41.6	39244 + 633
8	8	1666.7 - 38.5	40166 + 631
9	9	1591.0 - 35.9	41088 + 629
10	10	1525.1 - 33.6	41981 + 628
11	11	1467.8 - 31.6	42827 + 626
12	12	1418.1 - 30.0	43618 + 625
13	13	1375.0 - 28.5	44350 + 623
14	14	1337.3 - 27.2	45024 + 621
15	15	1304.3 - 26.1	45644 + 618
16	16	1275.3 - 25.1	46214 + 616
17	17	1249.4 - 24.2	46741 + 613
18	18	1226.3 - 23.4	47229 + 611
19	19	1205.4 - 22.7	47685 + 608
20	20	1186.4 - 22.1	48112 + 605
21	21	1169.0 - 21.5	48514 + 603
22	22	1153.0 - 20.9	48895 + 600
23	23	1138.2 - 20.4	49256 + 598
24	24	1124.3 - 20.0	49601 + 595
25	25	1111.5 - 19.5	49930 + 593
$\ell - m = 2$			
4	2	3753.5 - 107.3	28318 + 553
5	3	2986.2 - 82.0	30495 + 570
6	4	2557.7 - 67.7	32390 + 584
7	5	2274.2 - 58.2	34088 + 594
8	6	2068.9 - 51.4	35631 + 602
9	7	1912.1 - 46.1	37041 + 607
10	8	1788.2 - 42.0	38327 + 612
11	9	1688.0 - 38.7	39500 + 614
12	10	1605.7 - 35.9	40565 + 616
13	11	1537.1 - 33.7	41532 + 617
14	12	1479.3 - 31.7	42409 + 617
15	13	1430.0 - 30.1	43206 + 616
16	14	1387.5 - 28.7	43933 + 615
17	15	1350.5 - 27.4	44598 + 614
18	16	1318.0 - 26.4	45211 + 612
19	17	1289.1 - 25.4	45778 + 611
20	18	1263.2 - 24.5	46306 + 609
21	19	1239.8 - 23.7	46799 + 606
22	20	1218.5 - 23.0	47263 + 604
23	21	1199.1 - 22.4	47701 + 602
24	22	1181.1 - 21.8	48115 + 600
25	23	1164.6 - 21.2	48508 + 598
$\ell - m = 4$			
7	3	3490.0 - 97.1	27489 + 521
8	4	2873.3 - 77.1	29975 + 547
9	5	2490.0 - 64.6	32091 + 566
10	6	2226.7 - 56.0	33930 + 580
11	7	2034.1 - 49.7	35547 + 591
12	8	1887.1 - 44.9	36978 + 598
13	9	1771.4 - 41.1	38252 + 603
14	10	1678.1 - 38.1	39391 + 607
15	11	1601.4 - 35.6	40414 + 609
16	12	1537.2 - 33.5	41338 + 610
17	13	1482.8 - 31.7	42176 + 611
18	14	1435.9 - 30.1	42942 + 611
19	15	1395.1 - 28.8	43645 + 610
20	16	1359.2 - 27.6	44294 + 609
21	17	1327.2 - 26.5	44897 + 608
22	18	1298.6 - 25.6	45460 + 606
23	19	1272.8 - 24.7	45988 + 605
24	20	1249.3 - 23.9	46484 + 603
25	21	1227.9 - 23.2	46953 + 601

Table 5.11: Pattern frequencies and Lindblad resonance locations of the Neptune model

Neptune model

ℓ	m	$\Omega_{\rm pat}$ (deg/day)	$r_{\rm res}$ (km)
$\ell = m$			
2	2	2292.5 - 45.4	41555 + 557
3	3	2251.9 - 42.6	38883 + 498
4	4	2088.3 - 38.1	39168 + 483
5	5	1940.9 - 34.3	40024 + 478
6	6	1821.9 - 31.3	40973 + 475
7	7	1726.4 - 28.9	41890 + 474
8	8	1648.6 - 27.0	42747 + 472
9	9	1583.8 - 25.4	43541 + 471
10	10	1529.0 - 24.1	44279 + 470
11	11	1481.7 - 22.9	44966 + 469
12	12	1440.4 - 21.9	45608 + 468
13	13	1404.0 - 21.0	46211 + 467
14	14	1371.5 - 20.2	46779 + 466
15	15	1342.2 - 19.5	47315 + 465
16	16	1315.7 - 18.9	47823 + 463
17	17	1291.5 - 18.3	48306 + 462
18	18	1269.4 - 17.8	48765 + 461
19	19	1249.0 - 17.3	49203 + 460
20	20	1230.1 - 16.9	49622 + 459
21	21	1212.6 - 16.5	50023 + 457
22	22	1196.3 - 16.1	50407 + 456
23	23	1181.0 - 15.7	50776 + 455
24	24	1166.7 - 15.4	51131 + 454
25	25	1153.3 - 15.1	51472 + 453
$\ell - m = 2$			
4	2	3803.1 - 76.1	29659 + 402
5	3	2969.9 - 57.1	32337 + 421
6	4	2526.1 - 46.9	34505 + 433
7	5	2247.0 - 40.5	36304 + 442
8	6	2053.6 - 36.0	37832 + 448
9	7	1910.6 - 32.6	39154 + 452
10	8	1799.8 - 30.1	40319 + 455
11	9	1711.0 - 28.0	41358 + 457
12	10	1637.8 - 26.3	42297 + 458
13	11	1576.2 - 24.8	43152 + 459
14	12	1523.4 - 23.6	43938 + 460
15	13	1477.6 - 22.5	44664 + 460
16	14	1437.4 - 21.6	45338 + 460
17	15	1401.6 - 20.8	45969 + 460
18	16	1369.6 - 20.0	46560 + 459
19	17	1340.8 - 19.4	47116 + 459
20	18	1314.6 - 18.7	47642 + 458
21	19	1290.6 - 18.2	48140 + 457
22	20	1268.7 - 17.7	48612 + 457
23	21	1248.4 - 17.2	49062 + 456
24	22	1229.7 - 16.8	49491 + 455
25	23	1212.2 - 16.4	49901 + 454
$\ell - m = 4$			
6	2	4638.9 - 93.8	25983 + 356
7	3	3461.9 - 67.4	29198 + 385
8	4	2863.8 - 54.0	31739 + 405
9	5	2498.8 - 45.7	33825 + 418
10	6	2251.3 - 40.1	35586 + 428
11	7	2071.3 - 36.0	37104 + 436
12	8	1933.8 - 32.9	38436 + 441
13	9	1824.9 - 30.4	39620 + 445
14	10	1736.2 - 28.3	40684 + 448
15	11	1662.3 - 26.6	41650 + 451
16	12	1599.6 - 25.2	42533 + 452
17	13	1545.6 - 24.0	43345 + 454
18	14	1498.5 - 22.9	44097 + 454
19	15	1457.0 - 21.9	44797 + 455
20	16	1420.1 - 21.1	45451 + 455
21	17	1387.0 - 20.3	46064 + 455
22	18	1357.2 - 19.6	46641 + 455
23	19	1330.0 - 19.0	47186 + 455
24	20	1305.2 - 18.4	47702 + 454
25	21	1282.4 - 17.9	48191 + 454

Table 5.12: Pattern frequencies and vertical resonance locations of the thick Uranus model

Uranus Thick model			
ℓ	m	Ω_{pat} (deg/day)	r_{res} (km)
$\ell - m = 1$			
3	2	3166.5 - 89.8	31763 + 613
4	3	2637.1 - 71.5	33162 + 611
5	4	2296.5 - 59.7	34825 + 615
6	5	2057.3 - 51.5	36463 + 621
7	6	1881.0 - 45.6	37981 + 625
8	7	1747.4 - 41.1	39344 + 628
9	8	1644.1 - 37.6	40545 + 629
10	9	1562.7 - 34.8	41593 + 629
11	10	1497.3 - 32.6	42507 + 628
12	11	1443.7 - 30.8	43311 + 627
13	12	1398.7 - 29.3	44029 + 625
14	13	1360.1 - 28.0	44680 + 623
15	14	1326.5 - 26.8	45276 + 620
16	15	1296.7 - 25.8	45828 + 618
17	16	1270.2 - 24.9	46344 + 615
18	17	1246.2 - 24.1	46827 + 612
19	18	1224.4 - 23.3	47284 + 610
20	19	1204.4 - 22.7	47715 + 607
21	20	1186.1 - 22.0	48125 + 605
22	21	1169.2 - 21.5	48514 + 602
23	22	1153.4 - 20.9	48886 + 599
24	23	1138.8 - 20.4	49241 + 597
25	24	1125.2 - 20.0	49581 + 594
$\ell - m = 3$			
5	2	4166.5 - 119.4	26475 + 515
6	3	3133.2 - 85.9	29574 + 551
7	4	2594.4 - 68.3	32113 + 575
8	5	2261.8 - 57.5	34235 + 591
9	6	2036.4 - 50.1	36027 + 602
10	7	1874.5 - 44.8	37549 + 609
11	8	1752.9 - 40.8	38853 + 614
12	9	1658.2 - 37.7	39983 + 616
13	10	1582.1 - 35.1	40977 + 617
14	11	1519.4 - 33.1	41863 + 618
15	12	1466.5 - 31.3	42664 + 617
16	13	1421.1 - 29.8	43394 + 616
17	14	1381.5 - 28.5	44067 + 615
18	15	1346.7 - 27.3	44689 + 613
19	16	1315.7 - 26.2	45269 + 612
20	17	1287.9 - 25.3	45812 + 610
21	18	1262.7 - 24.5	46322 + 608
22	19	1239.9 - 23.7	46803 + 606
23	20	1218.9 - 23.0	47257 + 603
24	21	1199.7 - 22.4	47688 + 601
25	22	1182.0 - 21.8	48097 + 599
$\ell - m = 5$			
8	3	3461.8 - 95.8	27679 + 520
9	4	2821.1 - 75.2	30374 + 550
10	5	2435.7 - 62.7	32590 + 570
11	6	2178.8 - 54.4	34444 + 584
12	7	1995.2 - 48.4	36022 + 594
13	8	1857.3 - 43.9	37386 + 600
14	9	1749.4 - 40.4	38583 + 605
15	10	1662.5 - 37.6	39648 + 608
16	11	1590.6 - 35.2	40606 + 609
17	12	1530.0 - 33.2	41476 + 610
18	13	1478.1 - 31.5	42271 + 610
19	14	1433.1 - 30.0	43004 + 610
20	15	1393.6 - 28.7	43683 + 609
21	16	1358.5 - 27.5	44314 + 608
22	17	1327.2 - 26.5	44904 + 607
23	18	1299.0 - 25.6	45457 + 606
24	19	1273.4 - 24.7	45977 + 604
25	20	1250.1 - 23.9	46469 + 602

Table 5.13: Pattern frequencies and vertical resonance locations of the medium Uranus model

Uranus Medium model

ℓ	m	$\Omega_{\rm pat}$ (deg/day)	$r_{\rm res}$ (km)
$\ell - m = 1$			
3	2	3175.4 - 90.1	31704 + 612
4	3	2661.6 - 72.2	32959 + 608
5	4	2329.7 - 60.7	34494 + 611
6	5	2094.4 - 52.7	36031 + 615
7	6	1918.8 - 46.6	37482 + 619
8	7	1783.2 - 42.0	38818 + 621
9	8	1675.8 - 38.4	40033 + 623
10	9	1589.0 - 35.5	41133 + 624
11	10	1517.7 - 33.1	42127 + 624
12	11	1458.4 - 31.2	43021 + 623
13	12	1408.6 - 29.5	43823 + 622
14	13	1366.5 - 28.1	44541 + 621
15	14	1330.5 - 26.9	45184 + 619
16	15	1299.3 - 25.9	45767 + 617
17	16	1271.9 - 24.9	46301 + 615
18	17	1247.4 - 24.1	46796 + 612
19	18	1225.3 - 23.4	47259 + 610
20	19	1205.2 - 22.7	47695 + 607
21	20	1186.7 - 22.0	48107 + 605
22	21	1169.7 - 21.5	48499 + 602
23	22	1153.9 - 20.9	48872 + 599
24	23	1139.3 - 20.4	49228 + 597
25	24	1125.6 - 20.0	49569 + 594
$\ell - m = 3$			
5	2	4231.9 - 121.5	26202 + 511
6	3	3193.5 - 87.8	29202 + 545
7	4	2649.1 - 70.0	31670 + 568
8	5	2309.8 - 58.9	33760 + 584
9	6	2076.8 - 51.2	35559 + 596
10	7	1906.7 - 45.7	37125 + 604
11	8	1777.1 - 41.4	38500 + 609
12	9	1675.3 - 38.1	39711 + 613
13	10	1593.5 - 35.4	40782 + 615
14	11	1526.6 - 33.2	41731 + 616
15	12	1471.0 - 31.4	42576 + 616
16	13	1424.0 - 29.9	43335 + 616
17	14	1383.5 - 28.5	44025 + 615
18	15	1348.1 - 27.3	44658 + 613
19	16	1316.8 - 26.3	45245 + 611
20	17	1288.7 - 25.3	45792 + 610
21	18	1263.4 - 24.5	46305 + 608
22	19	1240.5 - 23.7	46787 + 606
23	20	1219.5 - 23.0	47243 + 603
24	21	1200.2 - 22.4	47675 + 601
25	22	1182.4 - 21.8	48085 + 599
$\ell - m = 5$			
8	3	3538.6 - 98.1	27279 + 514
9	4	2879.0 - 76.8	29967 + 543
10	5	2478.6 - 63.9	32214 + 564
11	6	2209.5 - 55.2	34125 + 579
12	7	2016.1 - 49.0	35773 + 590
13	8	1870.8 - 44.3	37205 + 598
14	9	1757.9 - 40.6	38459 + 603
15	10	1667.7 - 37.7	39564 + 607
16	11	1594.0 - 35.3	40549 + 609
17	12	1532.3 - 33.3	41435 + 610
18	13	1479.7 - 31.5	42241 + 610
19	14	1434.3 - 30.0	42980 + 610
20	15	1394.5 - 28.7	43663 + 609
21	16	1359.3 - 27.6	44297 + 608
22	17	1327.9 - 26.5	44888 + 607
23	18	1299.6 - 25.6	45443 + 606
24	19	1274.0 - 24.7	45965 + 604
25	20	1250.6 - 24.0	46457 + 602

Table 5.14: Pattern frequencies and vertical resonance locations of the thin Uranus model

Uranus Thin model			
ℓ	m	$\Omega_{\rm pat}$ (deg/day)	$r_{\rm res}$ (km)
$\ell - m = 1$			
3	2	3176.8 - 90.2	31695 + 612
4	3	2678.2 - 72.8	32823 + 607
5	4	2354.5 - 61.6	34252 + 609
6	5	2122.9 - 53.6	35709 + 612
7	6	1948.1 - 47.6	37106 + 616
8	7	1811.8 - 42.9	38409 + 618
9	8	1702.9 - 39.2	39608 + 619
10	9	1614.1 - 36.2	40706 + 620
11	10	1540.5 - 33.8	41710 + 620
12	11	1478.6 - 31.7	42628 + 619
13	12	1425.8 - 29.9	43470 + 619
14	13	1380.3 - 28.4	44244 + 618
15	14	1340.8 - 27.2	44952 + 617
16	15	1306.6 - 26.0	45598 + 615
17	16	1276.7 - 25.1	46185 + 614
18	17	1250.6 - 24.2	46717 + 612
19	18	1227.5 - 23.4	47204 + 609
20	19	1206.7 - 22.7	47655 + 607
21	20	1187.9 - 22.1	48076 + 605
22	21	1170.6 - 21.5	48474 + 602
23	22	1154.7 - 21.0	48851 + 599
24	23	1139.9 - 20.5	49210 + 597
25	24	1126.1 - 20.0	49553 + 594
$\ell - m = 3$			
5	2	4283.1 - 123.2	25994 + 508
6	3	3241.6 - 89.3	28914 + 541
7	4	2693.2 - 71.4	31325 + 564
8	5	2349.6 - 60.1	33379 + 580
9	6	2112.4 - 52.3	35160 + 591
10	7	1938.3 - 46.6	36722 + 599
11	8	1804.9 - 42.2	38105 + 605
12	9	1699.2 - 38.7	39339 + 608
13	10	1613.3 - 35.9	40448 + 611
14	11	1542.3 - 33.6	41449 + 613
15	12	1482.6 - 31.7	42355 + 613
16	13	1432.0 - 30.0	43173 + 614
17	14	1388.8 - 28.6	43913 + 613
18	15	1351.6 - 27.4	44581 + 612
19	16	1319.1 - 26.3	45191 + 611
20	17	1290.4 - 25.4	45752 + 609
21	18	1264.7 - 24.5	46274 + 608
22	19	1241.5 - 23.8	46762 + 606
23	20	1220.3 - 23.0	47222 + 603
24	21	1200.9 - 22.4	47656 + 601
25	22	1183.0 - 21.8	48069 + 599
$\ell - m = 5$			
8	3	3604.4 - 100.2	26948 + 509
9	4	2931.5 - 78.5	29609 + 538
10	5	2521.9 - 65.2	31845 + 560
11	6	2245.4 - 56.3	33761 + 575
12	7	2045.8 - 49.8	35427 + 586
13	8	1894.6 - 44.9	36894 + 594
14	9	1776.2 - 41.1	38195 + 600
15	10	1681.0 - 38.0	39356 + 604
16	11	1603.0 - 35.5	40396 + 607
17	12	1538.3 - 33.4	41328 + 608
18	13	1483.7 - 31.6	42167 + 609
19	14	1437.0 - 30.1	42927 + 609
20	15	1396.4 - 28.8	43623 + 609
21	16	1360.7 - 27.6	44266 + 608
22	17	1329.0 - 26.6	44863 + 607
23	18	1300.5 - 25.6	45422 + 606
24	19	1274.7 - 24.8	45946 + 604
25	20	1251.3 - 24.0	46440 + 602

Table 5.15: Pattern frequencies and vertical resonance locations of the adiabatic Uranus model

Uranus Adiabatic model

ℓ	m	Ω_{pat} (deg/day)	r_{res} (km)
$\ell - m = 1$			
3	2	3051.9 - 86.3	32550 + 626
4	3	2487.2 - 66.9	34478 + 631
5	4	2170.8 - 56.0	36153 + 634
6	5	1965.1 - 48.9	37591 + 635
7	6	1818.9 - 43.8	38839 + 635
8	7	1708.7 - 40.0	39935 + 634
9	8	1622.1 - 37.0	40911 + 633
10	9	1551.7 - 34.6	41789 + 631
11	10	1493.1 - 32.5	42587 + 629
12	11	1443.4 - 30.8	43318 + 627
13	12	1400.5 - 29.4	43992 + 625
14	13	1363.0 - 28.1	44616 + 622
15	14	1329.9 - 26.9	45199 + 620
16	15	1300.4 - 25.9	45743 + 617
17	16	1273.8 - 25.0	46255 + 615
18	17	1249.8 - 24.2	46737 + 612
19	18	1227.9 - 23.4	47193 + 610
20	19	1207.8 - 22.8	47625 + 607
21	20	1189.4 - 22.1	48035 + 605
22	21	1172.3 - 21.6	48426 + 602
23	22	1156.5 - 21.0	48799 + 600
24	23	1141.8 - 20.5	49155 + 597
25	24	1128.0 - 20.0	49496 + 595
$\ell - m = 3$			
5	2	3924.0 - 112.0	27549 + 534
6	3	2985.3 - 81.4	30539 + 566
7	4	2504.9 - 65.7	32871 + 586
8	5	2209.7 - 56.0	34769 + 599
9	6	2008.3 - 49.3	36362 + 607
10	7	1861.0 - 44.4	37730 + 612
11	8	1747.9 - 40.7	38926 + 615
12	9	1657.9 - 37.7	39987 + 617
13	10	1584.4 - 35.2	40938 + 617
14	11	1522.8 - 33.2	41800 + 617
15	12	1470.5 - 31.4	42587 + 617
16	13	1425.2 - 29.9	43310 + 616
17	14	1385.7 - 28.6	43978 + 615
18	15	1350.8 - 27.4	44599 + 613
19	16	1319.7 - 26.4	45179 + 611
20	17	1291.7 - 25.4	45722 + 610
21	18	1266.4 - 24.6	46232 + 608
22	19	1243.4 - 23.8	46714 + 606
23	20	1222.3 - 23.1	47170 + 604
24	21	1203.0 - 22.5	47601 + 601
25	22	1185.1 - 21.9	48012 + 599
$\ell - m = 5$			
8	3	3378.7 - 93.3	28129 + 528
9	4	2780.7 - 74.0	30667 + 555
10	5	2417.7 - 62.2	32751 + 573
11	6	2172.6 - 54.2	34509 + 585
12	7	1995.1 - 48.5	36023 + 594
13	8	1860.2 - 44.0	37347 + 600
14	9	1753.7 - 40.5	38521 + 604
15	10	1667.3 - 37.7	39572 + 607
16	11	1595.5 - 35.3	40522 + 609
17	12	1534.9 - 33.4	41388 + 610
18	13	1482.9 - 31.6	42182 + 610
19	14	1437.6 - 30.1	42914 + 610
20	15	1397.9 - 28.8	43592 + 609
21	16	1362.7 - 27.7	44224 + 608
22	17	1331.1 - 26.6	44815 + 607
23	18	1302.8 - 25.7	45369 + 606
24	19	1277.0 - 24.8	45891 + 604
25	20	1253.6 - 24.1	46383 + 602

Table 5.16: Pattern frequencies and vertical resonance locations of the shallow Uranus model

Uranus Shallow model

ℓ	m	$\Omega_{\rm pat}$ (deg/day)	$r_{\rm res}$ (km)
$\ell - m = 1$			
3	2	3069.0 - 86.9	32429 + 625
4	3	2633.1 - 71.6	33195 + 613
5	4	2344.5 - 61.5	34349 + 612
6	5	2133.7 - 54.2	35589 + 614
7	6	1970.3 - 48.5	36828 + 616
8	7	1839.1 - 44.0	38029 + 618
9	8	1731.5 - 40.4	39172 + 620
10	9	1642.0 - 37.3	40245 + 621
11	10	1566.9 - 34.8	41241 + 621
12	11	1503.4 - 32.7	42159 + 621
13	12	1449.3 - 30.9	43000 + 620
14	13	1402.9 - 29.3	43769 + 619
15	14	1362.7 - 27.9	44471 + 618
16	15	1327.7 - 26.8	45115 + 616
17	16	1296.8 - 25.7	45707 + 614
18	17	1269.4 - 24.8	46254 + 612
19	18	1244.9 - 24.0	46762 + 610
20	19	1222.8 - 23.2	47237 + 607
21	20	1202.6 - 22.5	47683 + 605
22	21	1184.2 - 21.9	48103 + 602
23	22	1167.2 - 21.4	48501 + 600
24	23	1151.5 - 20.8	48879 + 598
25	24	1136.9 - 20.3	49239 + 595
$\ell - m = 3$			
5	2	4269.7 - 123.0	26049 + 510
6	3	3264.4 - 90.3	28780 + 541
7	4	2730.1 - 72.8	31043 + 563
8	5	2390.7 - 61.7	32997 + 578
9	6	2152.9 - 53.8	34719 + 590
10	7	1976.1 - 48.0	36253 + 598
11	8	1839.4 - 43.5	37627 + 604
12	9	1730.8 - 39.9	38859 + 608
13	10	1642.5 - 37.0	39967 + 611
14	11	1569.6 - 34.6	40966 + 613
15	12	1508.5 - 32.6	41868 + 613
16	13	1456.6 - 30.9	42686 + 613
17	14	1411.9 - 29.4	43433 + 613
18	15	1373.0 - 28.1	44117 + 612
19	16	1338.8 - 27.0	44748 + 611
20	17	1308.4 - 26.0	45333 + 609
21	18	1281.1 - 25.1	45879 + 607
22	19	1256.5 - 24.2	46390 + 606
23	20	1234.1 - 23.5	46870 + 604
24	21	1213.6 - 22.8	47323 + 602
25	22	1194.8 - 22.2	47753 + 600
$\ell - m = 5$			
8	3	3677.8 - 102.8	26590 + 505
9	4	2995.8 - 80.7	29186 + 535
10	5	2577.5 - 67.2	31387 + 556
11	6	2293.6 - 58.0	33288 + 572
12	7	2088.0 - 51.3	34949 + 584
13	8	1932.4 - 46.3	36412 + 592
14	9	1810.6 - 42.3	37711 + 598
15	10	1712.7 - 39.1	38869 + 602
16	11	1632.5 - 36.5	39910 + 605
17	12	1565.4 - 34.3	40850 + 607
18	13	1508.5 - 32.4	41704 + 608
19	14	1459.4 - 30.8	42486 + 608
20	15	1416.8 - 29.4	43206 + 608
21	16	1379.2 - 28.2	43871 + 607
22	17	1345.7 - 27.1	44491 + 606
23	18	1315.8 - 26.1	45069 + 605
24	19	1288.8 - 25.2	45612 + 604
25	20	1264.2 - 24.4	46123 + 602

Table 5.17: Pattern frequencies and vertical resonance locations of the Neptune model

Neptune model			
ℓ	m	$\Omega_{\rm pat}$ (deg/day)	$r_{\rm res}$ (km)
$\ell - m = 1$			
3	2	3211.4 - 63.9	33238 + 447
4	3	2659.9 - 50.8	34830 + 449
5	4	2326.8 - 42.8	36470 + 454
6	5	2103.6 - 37.5	37953 + 457
7	6	1943.3 - 33.7	39264 + 460
8	7	1822.2 - 30.8	40423 + 462
9	8	1726.8 - 28.6	41458 + 463
10	9	1649.4 - 26.7	42391 + 464
11	10	1584.9 - 25.2	43241 + 464
12	11	1530.1 - 23.9	44021 + 464
13	12	1482.9 - 22.8	44741 + 464
14	13	1441.6 - 21.8	45411 + 463
15	14	1405.1 - 20.9	46036 + 463
16	15	1372.5 - 20.2	46623 + 462
17	16	1343.1 - 19.5	47175 + 461
18	17	1316.6 - 18.9	47697 + 460
19	18	1292.3 - 18.3	48191 + 459
20	19	1270.1 - 17.8	48660 + 459
21	20	1249.7 - 17.3	49107 + 458
22	21	1230.8 - 16.8	49534 + 457
23	22	1213.2 - 16.4	49941 + 455
24	23	1196.8 - 16.0	50332 + 454
25	24	1181.5 - 15.7	50706 + 453
$\ell - m = 3$			
5	2	4256.1 - 85.7	27568 + 374
6	3	3230.4 - 62.5	30610 + 400
7	4	2702.6 - 50.6	33013 + 417
8	5	2377.7 - 43.2	34983 + 429
9	6	2155.7 - 38.1	36645 + 437
10	7	1993.3 - 34.4	38079 + 443
11	8	1868.6 - 31.5	39336 + 448
12	9	1769.4 - 29.2	40455 + 451
13	10	1688.1 - 27.3	41462 + 453
14	11	1620.2 - 25.8	42377 + 455
15	12	1562.3 - 24.4	43215 + 456
16	13	1512.2 - 23.3	43987 + 457
17	14	1468.5 - 22.3	44703 + 457
18	15	1429.8 - 21.4	45370 + 457
19	16	1395.3 - 20.6	45994 + 457
20	17	1364.2 - 19.8	46580 + 457
21	18	1336.2 - 19.2	47132 + 457
22	19	1310.6 - 18.6	47655 + 456
23	20	1287.2 - 18.1	48150 + 455
24	21	1265.6 - 17.6	48620 + 455
25	22	1245.7 - 17.1	49068 + 454
$\ell - m = 5$			
7	2	4980.5 - 101.1	24839 + 340
8	3	3673.9 - 71.9	28103 + 371
9	4	3013.5 - 57.1	30708 + 393
10	5	2612.4 - 48.1	32860 + 409
11	6	2341.5 - 42.0	34684 + 420
12	7	2145.3 - 37.6	36262 + 429
13	8	1995.9 - 34.2	37648 + 435
14	9	1878.1 - 31.5	38881 + 440
15	10	1782.3 - 29.3	39990 + 444
16	11	1702.8 - 27.5	40996 + 447
17	12	1635.6 - 26.0	41915 + 449
18	13	1577.8 - 24.7	42760 + 451
19	14	1527.6 - 23.5	43543 + 452
20	15	1483.5 - 22.5	44270 + 453
21	16	1444.3 - 21.6	44949 + 453
22	17	1409.2 - 20.8	45585 + 454
23	18	1377.6 - 20.1	46183 + 454
24	19	1348.9 - 19.4	46748 + 454
25	20	1322.8 - 18.8	47282 + 453

Appendix C.2. Extended tables of g-mode frequencies and resonance locations

In this appendix, we present all the calculated g-mode frequencies and resonance locations for all the models. Table 5.19 displays the $\ell = m$, $n = 1$ Lindblad resonance locations for Uranus. Table 5.18 shows the $\ell = m$, $n = 1$ Lindblad resonance locations and the corotation resonance locations associated with them for Neptune.

Table 5.18: $\ell = m$, $n = 1$, g-mode pattern frequencies and Lindblad resonance locations of the Neptune model

ℓ,m	Ω_{pat} (deg/day)	r_{res} (km)	r_{cor} (km)
1	1808.1 - 34.7	58959 + 766	37170 + 481
2	1683.1 - 28.2	51058 + 578	38986 + 441
3	1566.6 - 24.6	49518 + 526	40893 + 433
4	1462.1 - 21.9	49668 + 502	42815 + 432
5	1369.0 - 19.7	50502 + 489	44732 + 432
6	1287.1 - 17.7	51646 + 480	46611 + 432
7	1215.6 - 16.1	52917 + 472	48417 + 431
8	1153.8 - 14.7	54217 + 465	50129 + 429
9	1100.5 - 13.5	55495 + 458	51736 + 426
10	1054.3 - 12.5	56722 + 451	53235 + 423
11	1014.1 - 11.6	57888 + 444	54630 + 418
12	979.0 - 10.8	58988 + 437	55927 + 414
13	948.2 - 10.1	60022 + 429	57132 + 408
14	920.9 - 9.5	60992 + 422	58253 + 402
15	896.7 - 8.9	61902 + 415	59299 + 396
16	875.0 - 8.5	62757 + 407	60274 + 390
17	855.5 - 8.0	63560 + 400	61186 + 385
18	837.9 - 7.6	64315 + 393	62041 + 379
19	821.9 - 7.3	65027 + 386	62843 + 373
20	807.3 - 6.9	65698 + 379	63597 + 367
21	793.9 - 6.6	66331 + 373	64308 + 361
22	781.7 - 6.4	66931 + 366	64978 + 355
23	770.4 - 6.1	67498 + 360	65612 + 349
24	759.9 - 5.9	68036 + 354	66211 + 344
25	750.2 - 5.7	68547 + 348	66779 + 339

Table 5.19: $\ell = m$, $n = 1$, g-mode pattern frequencies and Lindblad resonance locations of non-adiabatic Uranus models

	Thick		**Medium**		**Thin**		**Shallow**	
ℓ,m	$\Omega_{\rm pat}$ (deg/day)	$r_{\rm res}$ (km)	$\Omega_{\rm pat}$ (deg/day)	$r_{\rm res}$ (km)	$\Omega_{\rm pat}$ (deg/day)	$r_{\rm res}$ (km)	$\Omega_{\rm pat}$ (deg/day)	$r_{\rm res}$ (km)
1	1785.9 - 49.8	56259 +1070	1807.0 - 50.7	55820 +1069	1769.6 - 49.4	56605 +1079	1418.5 - 37.2	65597 +1172
2	1723.2 - 42.2	47569 + 793	1745.5 - 43.2	47163 + 794	1717.1 - 42.2	47682 + 798	1426.3 - 31.9	53959 + 819
3	1659.1 - 38.7	45108 + 715	1684.8 - 39.8	44647 + 716	1662.1 - 39.0	45053 + 719	1400.9 - 29.7	50490 + 726
4	1602.1 - 36.2	44230 + 679	1632.0 - 37.5	43688 + 681	1614.4 - 36.9	44005 + 683	1375.4 - 28.3	48962 + 684
5	1550.0 - 34.2	44004 + 659	1584.4 - 35.6	43365 + 662	1571.3 - 35.2	43605 + 663	1351.5 - 27.3	48211 + 659
6	1501.1 - 32.4	44118 + 646	1540.3 - 34.0	43367 + 649	1531.2 - 33.7	43539 + 651	1328.6 - 26.4	47857 + 644
7	1454.7 - 30.7	44438 + 636	1499.1 - 32.5	43556 + 640	1493.5 - 32.4	43665 + 642	1306.3 - 25.5	47740 + 632
8	1410.1 - 29.1	44897 + 628	1460.5 - 31.1	43859 + 634	1457.8 - 31.1	43912 + 635	1284.3 - 24.8	47780 + 624
9	1367.0 - 27.6	45457 + 622	1424.2 - 29.8	44233 + 628	1424.2 - 29.9	44234 + 630	1262.4 - 24.0	47932 + 617
10	1325.5 - 26.2	46091 + 616	1390.1 - 28.6	44653 + 623	1392.4 - 28.8	44604 + 626	1240.6 - 23.3	48168 + 611
11	1285.9 - 24.8	46774 + 611	1358.0 - 27.5	45103 + 618	1362.5 - 27.8	45004 + 622	1218.9 - 22.5	48469 + 606
12	1248.5 - 23.6	47482 + 606	1327.7 - 26.4	45576 + 614	1334.4 - 26.8	45422 + 618	1197.3 - 21.8	48823 + 601
13	1213.7 - 22.4	48194 + 602	1298.7 - 25.4	46068 + 610	1308.1 - 25.9	45848 + 614	1176.0 - 21.1	49218 + 597
14	1181.5 - 21.4	48898 + 598	1271.0 - 24.4	46577 + 606	1283.3 - 25.0	46278 + 610	1154.9 - 20.4	49644 + 592
15	1151.9 - 20.4	49585 + 593	1244.4 - 23.5	47096 + 602	1259.8 - 24.2	46712 + 606	1134.4 - 19.7	50093 + 588
16	1124.6 - 19.5	50250 + 589	1219.2 - 22.7	47619 + 599	1237.4 - 23.4	47152 + 603	1114.4 - 19.1	50557 + 584
17	1099.6 - 18.7	50891 + 584	1195.4 - 21.9	48138 + 596	1215.7 - 22.6	47601 + 599	1095.1 - 18.4	51030 + 580
18	1076.6 - 17.9	51508 + 579	1173.0 - 21.1	48646 + 593	1194.7 - 21.9	48057 + 596	1076.6 - 17.8	51506 + 576
19	1055.3 - 17.2	52102 + 574	1152.1 - 20.4	49142 + 590	1174.6 - 21.2	48515 + 593	1059.0 - 17.3	51980 + 572
20	1035.6 - 16.6	52672 + 570	1132.6 - 19.8	49622 + 587	1155.4 - 20.6	48968 + 590	1042.2 - 16.7	52449 + 568
21	1017.3 - 16.0	53220 + 565	1114.3 - 19.2	50088 + 583	1137.2 - 20.0	49413 + 587	1026.2 - 16.2	52911 + 564
22	1000.3 - 15.4	53748 + 560	1097.2 - 18.6	50538 + 580	1120.0 - 19.4	49848 + 584	1011.1 - 15.7	53363 + 560
23	984.4 - 14.9	54255 + 555	1081.1 - 18.1	50973 + 577	1103.9 - 18.9	50270 + 581	996.8 - 15.3	53805 + 556
24	969.6 - 14.4	54744 + 550	1065.9 - 17.6	51395 + 574	1088.6 - 18.4	50680 + 578	983.2 - 14.8	54236 + 552
25	955.7 - 14.0	55214 + 545	1051.7 - 17.2	51803 + 571	1074.2 - 17.9	51078 + 575	970.4 - 14.4	54654 + 548

Appendix C.3. Voyager images of the Uranian and Neptunian rings

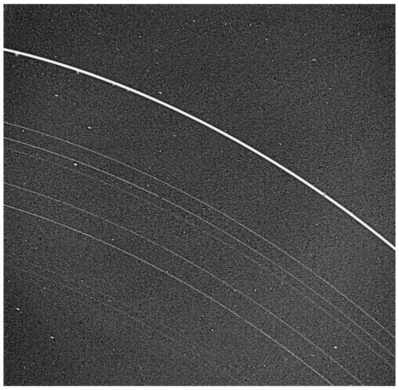

Figure 5.25: Voyager image of the Uranian rings.

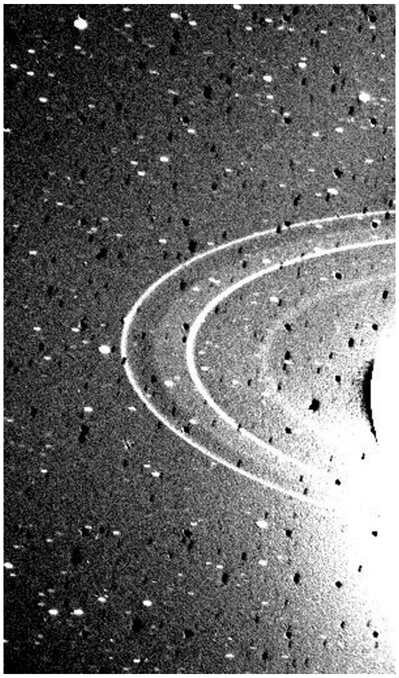

Figure 5.26: Voyager image of the Neptunian rings.

Appendix D: Copyright for published articles

Appendix D.1. Copyright for IOP Publishing

Quoted from IOP publishing permissions FAQs:

Question: "May I include the Final Published Version of the article in my research thesis or dissertation?"

Answer: "Upon transfer of copyright, IOP and/or the copyright owner grants back to authors a number of rights. These include the right to include the Final Published Version of the article in your research thesis or dissertation. Please include citation details and, for online use, a link to the Version of Record. IOP's permission will be required for commercial use of an article published as part of your thesis. IOP does not allow ProQuest to publish or sell the article as part of your dissertation."

Credit for Chapter 2: A'Hearn, J.A., Hedman, M.M., El Moutamid, M. 2019 "Dynamics of multiple bodies in a corotation resonance: Conserved quantities and relevance to ring arcs" The Astrophysical Journal, 882, 66, reproduced by permission of the AAS.

Credit for Chapter 3: A'Hearn, J.A., Hedman, M.M., Hamilton, D.P. 2021 "Modeling Saturn's D68 Clumps as a Co-orbital Satellite System" The Planetary Science Journal 2, 74, reproduced by permission of the AAS.

Credit for Chapter 4: But it will have been only submitted, not published yet

Links to publications:

Chapter 2: https://doi.org/10.3847/1538-4357/ab31af
Chapter 3: https://doi.org/10.3847/PSJ/abed57

Appendix D.2. Copyright for arXiv

Although the paper published by MNRAS is not open access, a preliminary version of it can be found on arXiv with a copyright CC BY.

Credit for part of Chapter 5: Muñoz-Gutiérrez, M.A., Granados Contreras, A.P., Madeira, G., A'Hearn, J.A., Giuliatti Winter, S. 2021 "Long-term Dynamical Evolution of Pallene

(Saturn XXXIII) and Its Diffuse, Dusty Ring" Monthly Notices of the Royal Astronomical Society, stab3627

Links to publications:

Chapter 5, Section 2.2: https://doi.org/10.1093/mnras/stab3627; https://arxiv.org/abs/2112.05903